Direct Imaging of Intermediate Mass Giants with RV Trends

笠　嗣瑠

博士（理学）

総合研究大学院大学
物理科学研究科
天文科学専攻

平成３０（２０１８）年度

Direct Imaging of Intermediate Mass Giants with RV Trends

Dissertation for Doctor of Philosophy

Tsuguru Ryu
Department of Astronomical Science SOKENDAI
(The Graduate University for Advanced Studies)
20130955

June 26 2018

Abstract

Radial velocity (RV) technique is one of the most useful methods to detect exoplanets and has been used to discover over 700 planets in more than 500 systems in the last 20 years. This method has an advantage in detecting planets orbiting short distance from the host stars. However, it is less sensitive for wide-orbit planets with a semi-major axis a larger than 10 AU because it takes a long time to cover a full orbit of a such planet. The number of distant planets ($a > 10$ AU) is still small and more discovery of distant planets is required to understand the formation of distant planets. We developed a method to tackle such an observational challenge.

The long-term RV trend of a host star is a clue to discover planetary companions in wide-orbits. A linear RV trend shown in 10 years of observations can be generated by an object at 10 AU. It could also be generated by a distant stellar companion or a brown dwarf companion in an even wide-orbit (> 100 AU). Therefore, with the RV method alone we cannot distinguish between a planet and a stellar companion as a generator of the RV trend.

We chose direct-imaging technique which is to directly detect a companion, to uncover the nature of the RV trend generator (RVTG) through directly detecting a companion. Even with non-detection of any planetary/brown dwarf/stellar companions, the direct imaging data can constrain the range of the mass and the semi-major axis of the object that generates the RV trend. At Okayama Astrophysical Observatory (OAO), an RV survey targeting intermediate mass giants has been conducted for over a decade. Identifying the companions that generate the RV trends in this OAO survey can improve our knowledge of exoplanet populations for intermediate mass stars, which is not well understood compared with that of the solar type stars.

There are two formation theories of the giant gas planets. One is a core accretion model that can explain solar system formation, and the other is a gravitational instability in the protostellar disk. Which planetary formation theory matches the observational results of the exoplanets? Determining the occurrence rate of planets can be an important clue to understand the exoplanetary formation theory.

In this thesis, we aim to detect or put constraints on the objects responsible for the observed RV trends that indicate the presence of distant companions. We attempt to estimate the occurrence rate of distant planets around intermediate mass giants and compare it with that of a Sun-like star to put some constraints on planetary formation theory around intermediate mass stars.

With the above goal in mind, we conducted direct-imaging observations for thirty two intermediate mass giants with RV trends using the HiCIAO high-contrast camera on the 8.2m Subaru Telescope and the NESSI imager on the WIYN 3.5m telescope. We detected and confirmed three companions (γ Hya B, HD 5608 B, and HD 109272 B) and twelve targets with companion candidates. In contrast, we were not able to detect any companion candidates towards seven targets observed with HiCIAO and ten targets observed with NESSI.

By combining direct-imaging observation results with RV trend data, we clarify and constrain the RVTGs. We conclude that our confirmed three companions are responsible for the observed RV trend in each star. In addition, we conclude that the companion candidates around eight stars are likely to be the RVTGs for the observed RV trends even if considering the possibility of a contamination of background stars. For other stars, we constrain the nature of the RVTGs and find that thirteen targets have possibilities of

planetary ($< 13\ M_{\rm Jup}$) RVTGs at a = 9-26 AU, and/or sub-stellar ($< 75 M_{\rm Jup}$) RVTGs at a = 9-62 AU.

Considering limitations caused by the RV trend detection efficiency, white dwarf contamination, and missing stellar companions, we made a rough estimate of an upper limit of occurrence rates of wide-orbit planets around intermediate mass giants and suggested that it is less than 20%. This is a first clue to understand distant planet formation around intermediate mass giants. When we consider that NESSI observations could overlook companions, an upper limit of distant planet occurrence rates around intermediate mass giants can be 10 %. Our result could not distinguish between the core accretion and gravitational instability models for distant planet formation.

Based on our RVTG discussion of the eccentric systems, we suggest that Kozai mechanism is one of the likely origins of three eccentric planet systems in our sample, ι Dra b, HD 5608 b, and HD 14067 b.

Acknowledgements

First of all, I would like to be truly thankful to my supervisor, Professor Motohide Tamura. He gave me a chance to study extrasolar planets and observational astronomy. Without his generous support to conduct my studies, I could not have been completed this thesis.

I am also deeply thankful to Dr. Norio Narita for supervising and advising me. He has always discussed me to improve my studies.

I would like to show my appreciation Associate Professor Saeko S. Hayashi. She was always concerned about me and gave sincere advice.

I would like to acknowledge Professor Tomonori Usuda and Dr. Satoshi Mayama. They have also supervised me. I am grateful for their helpful advices for making my presentation better.

I also express my gratitude to my collaborators. Eespecially, I deeply acknowledge Dr. Masayuki Kuzuhara, Dr. Yasuhiro Takahashi and Dr. Akihiko Fukui, who supported my studies.

I thank my colleagues of NAOJ/Sokendai and my friends. They had encouraging talks to me to do my studies.

Finally, I express special appreciate to my mother, Yuko Ryu. My mother have encouraged me and supported me throughout my life.

Contents

1 Introduction **4**
- 1.1 Detection methods of exoplanets . . . 5
  - 1.1.1 Radial velocity method . . . 5
  - 1.1.2 Transit method . . . 6
  - 1.1.3 Micro-lensing method . . . 7
  - 1.1.4 Direct imaging method . . . 7
- 1.2 Discovery results and occurrence rate of exoplanets . . . 9
  - 1.2.1 Summary of discovery results and occurrence rate . . . 9
  - 1.2.2 RV survey for intermediate mass giants . . . 10
- 1.3 Formation and migration theory . . . 10
- 1.4 RV trend . . . 12
- 1.5 Purpose of the study . . . 14

2 Method **16**
- 2.1 Angular Differential Imaging (ADI) . . . 17
  - 2.1.1 Locally Optimized Combination of Imaging (LOCI) . . . 17
- 2.2 Bad pixels . . . 19
- 2.3 Analysis procedure for HiCIAO data . . . 21
- 2.4 Common proper motion test . . . 22
- 2.5 Estimation of mass and calculation of detection limit . . . 23

3 Observations **25**
- 3.1 HiCIAO and AO188 . . . 26
  - 3.1.1 AO188 . . . 26
  - 3.1.2 Atmospheric Dispersion Corrector (ADC) . . . 26
  - 3.1.3 HiCIAO . . . 26
- 3.2 WIYN telescope and NESSI instrument . . . 27
- 3.3 Okayama Astrophysical Observatory 188cm Telescope and HIDES instrument . . . 27
- 3.4 Observation targets . . . 28
  - 3.4.1 Age estimation of some of the systems . . . 38
  - 3.4.2 RV trends . . . 40
- 3.5 Direct Imaging Observations . . . 50

4 Results **53**
- 4.1 Confirmed Stellar Companions . . . 54
  - 4.1.1 γ Hya . . . 54
  - 4.1.2 HD 109272 . . . 54

4.1.3 HD 5608 . . . 54
4.2 Confirmed Background Star . . . 57
4.2.1 18 Del . . . 57
4.3 Case of the non-detection of the companion candidates from HiCIAO observations . . . 57
4.3.1 ι Dra . . . 57
4.3.2 HD 14067 . . . 59
4.3.3 HD 360 . . . 60
4.3.4 HD 4188 . . . 60
4.3.5 HD 15920 . . . 60
4.3.6 HD 120420 . . . 60
4.4 Case of the non-detection of the companion candidates from NESSI observations . . . 61
4.4.1 HD 11949 . . . 61
4.4.2 HD 45415 . . . 61
4.4.3 HD 54810 . . . 61
4.4.4 HD 65228 . . . 61
4.4.5 HD 95808 . . . 62
4.4.6 HD 106714 . . . 62
4.4.7 HD 157527 . . . 62
4.4.8 HD 159353 . . . 63
4.4.9 HD 162076 . . . 63
4.4.10 HD 167042 . . . 63
4.5 Stars with Companion Candidates . . . 65
4.5.1 HD 9408 . . . 65
4.5.2 HD 18970 . . . 65
4.5.3 HD 27971 . . . 66
4.5.4 HD 39007 . . . 66
4.5.5 HD 55730 . . . 67
4.5.6 HD 64152 . . . 67
4.5.7 ι Cnc A (HD 74739) . . . 68
4.5.8 ζ Crt (HD 102070) . . . 68
4.5.9 HD 111028 . . . 69
4.5.10 β Boo (HD 133208) . . . 69
4.5.11 HD 10348 . . . 70
4.5.12 HD 74395 . . . 70

5 Discussion **72**
5.1 RV Trend Generators . . . 73
5.1.1 Confirmed companion cases . . . 74
5.1.2 No companions cases . . . 74
5.1.3 Companion candidate cases . . . 80
5.1.4 Summary of RVTG . . . 82
5.2 Distant planet rate and implication for its formation model . . . 84
5.2.1 Planet occurrence rate . . . 84
5.3 Mechanism Influencing the Orbit of Inner Eccentric Planets . . . 88

6 Summary **89**

Chapter 1

Introduction

As an introduction to this thesis, in this chapter, we first introduce the detection methods of exoplanets and the progress of discovery of exoplanets. Second, we introduce the importance of wide-orbit planets supported by the planetary formation theory.

1.1 Detection methods of exoplanets

Since the majority of the discoveries were made through indirect method, I am going to summarize important ones to set foundation for my research.

1.1.1 Radial velocity method

The radial velocity (RV) method is one of the significant techniques to discover exoplanets and has been used in the discovery of more than 500 planets in the last 20 years. Using RV method, the first exoplanets orbiting around a sun-like star, 51 Peg b, was discovered (Mayor & Queloz, 1995).

The RV method uses variations of RV of a star (Figure 1.1). If a planet with M_p mass orbits around a star with M_* mass, the star with the semi-major axis a_* orbits around the common center of mass,

$$a_* = \frac{M_p}{M_*} a \tag{1.1.1}$$

where a is the semi-major axis of the planets. Along with this orbital motion, variation of the RV of the star can be written as,

$$\mathrm{RV} = \frac{2\pi a_*}{P\sqrt{1-e^2}}\, m_p \sin i\, (\cos(\omega + f) + e\cos\omega) \tag{1.1.2}$$

where G, e, i, ω, and f is the gravitational constant, the eccentricity of the orbit, the inclination of the orbit, the true anomaly, and the longitude of periastron, respectively. The RV amplitude K is defined as

$$K = \frac{M_p}{M_* + M_p} \frac{2\pi}{P} \frac{a \sin i}{\sqrt{1-e}}. \tag{1.1.3}$$

By measuring the RV of the star and deriving the period and eccentricity from the shape of the RV, we can obtain the planet mass as $M_p \sin i$, not M_p, with the assumption of the mass of the primary star M_*. The sensitivity of the RV method depends on mass and the period of the planet.

A radial velocity is measured using the Doppler effect of the spectrum obtained by the spectroscopy. Since an amplitude of an RV generated by a planet is typically from several tens m s^{-1} to several m s^{-1}, a high precision radial velocity measurement is required to detect a planet. The accuracy of the RV measurement, σ_{RV}, is written as

$$\sigma_{\mathrm{RV}} = \mathrm{c} \left(\sum_i \frac{\lambda_i^2 \cdot |dA_i/d\lambda|^2}{A_i + \sigma_D^2} \right)^{-1/2}, \tag{1.1.4}$$

where c is the speed of light, i is pixel of a detector, A is the flux, and σ_D is a read-out-noise of a detector (Bouchy et al., 2001). σ_{RV} is also estimated as

$$\sigma_{\mathrm{RV}} \approx 1.45 \times 10^9 \cdot (S/N)^{-1} \cdot R^{-1} \cdot B^{-1} (\mathrm{m\,s^{-1}}) \tag{1.1.5}$$

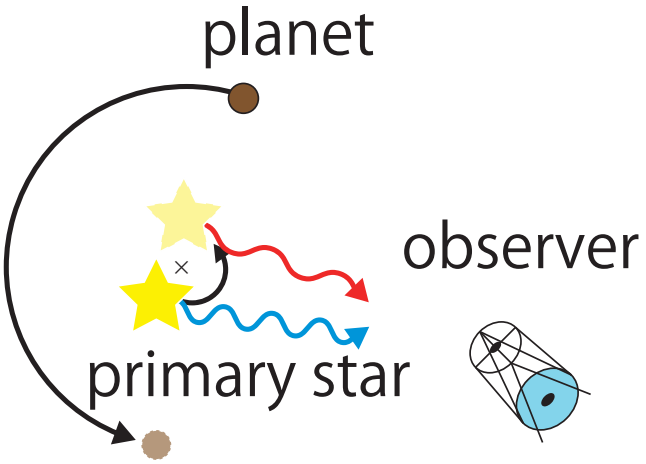

Figure 1.1: An illustration of the RV method.

where S/N is signal-to-noise, R is resolving power of a spectrometer, and B is wavelength coverage (Å) of a detector (Hatzes & Cochran, 1992). To achieve the high precision RV measurement to detect a planet, sharper spectrum is required. This is the reason why metal-rich, slowly rotating sun-like stars have been preferred as the targets in an early phase of the RV survey (e.g. Mayor & Queloz, 1995; Marcy & Butler, 1996).

An RV measurement with precision of 1m s^{-1} corresponds to a few 10^{-5} Å shifts in wavelengths, which is $\sim 1/1000$ of a detector pixels for a R=100,000 instrument. To measure this extreme small shift of spectrum, there are two methods, the iodine cell technique and the simultaneous reference technique.

The iodine cell technique uses a glass cell containing iodine that has many molecular absorption lines in optical regions (Marcy & Butler, 1992). The iodine cell is mounted in front of a spectrograph slit to superimpose iodine lines on a stellar spectrum. By analyzing the superimposed iodine lines on the stellar spectrum, a high precision RV is obtained. The iodine cell technique is widely used at telescopes such as Lick Observatory, Keck/HIRES, and Okayama Astrophysical Observatory/HIDES (Izumiura, 1999) because it is easy to install at spectrograph.

The simultaneous reference technique simultaneously acquires the stellar spectrum calibration lamp (e.g. Th-Ar lamp) fed by the optical fiber. Using this method, 51 Peg b was discovered with ELODIE spectrograph (Mayor & Queloz, 1995).

In this thesis, we employ the RV method to detect planetary companions.

1.1.2 Transit method

Transit method is to detect a flux dimming when a planet crosses in front of its primary star, like a solar eclipse. The first transiting exoplanet is discovered in HD 209458 (Charbonneau et al., 2000). Assuming the radius of the primary star,R_*, we can obtain the radius of the transiting planet, R_p because the transit depth δ is

$$\delta \approx (R_p/R_*)^2 \tag{1.1.6}$$

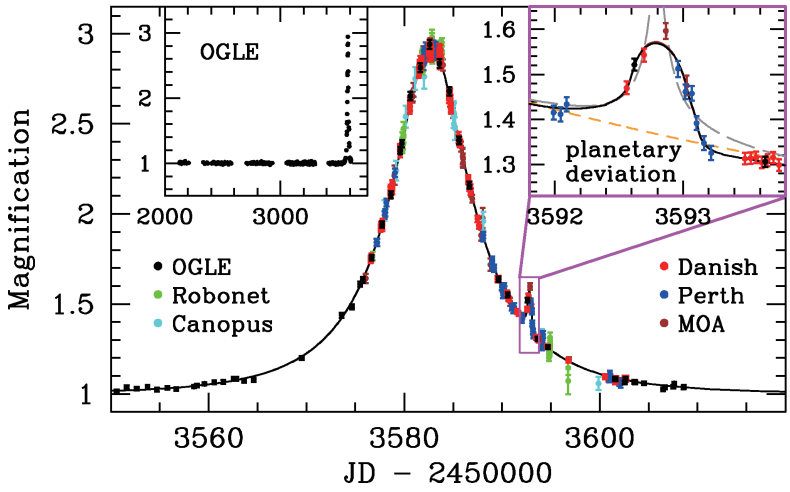

Figure 1.2: Light curve magnified by a micro-lensing event (Beaulieu et al., 2006). Second peak of light curve is caused by the detected planet.

The probability of transit, $p_{\rm tra}$, is

$$p_{\rm tra} = \frac{R_*}{a} \tag{1.1.7}$$

for the limiting case $R_p \ll R_*$ and e=0. This shows that the transit method is sensitive to an inner planet.

The transit method generally cannot estimate mass of the detected planet. With the mass estimated from the RV method,$M_p \sin i$, we can obtain the true mass of the planet because a transit observation measures the inclination of the planet. Moreover, the transit method enables us to probe atmosphere of the planet. Since the grazing starlight gets through the planetary atmosphere, starlight during the transit has wavelength dependency that caused by a planetary atmosphere and cloud.

1.1.3 Micro-lensing method

The micro-lensing method utilizes the general relativistic effect. When a foreground star and a distant background star are almost aligned in line of sight, the gravitational field of the foreground star bends the light from the background star like a "lens". This magnifies the light of the background star. If the foreground star hosts a planet, magnified light curve shows a spike features that is caused by the gravitational field of the planet (Figure 1.2). The micro-lensing method has an advantage to detect the planet whose projected separation is 1-10 astronomical units. However, it is difficult to do follow-up observations to grasp the properties of the planet.

1.1.4 Direct imaging method

The direct imaging is a method of directly detecting a light of a planet as its name implies. The most famous discoveries of planets using direct imaging method are HR 8799 b, c, d (Marois et al., 2008). Since a planet has a very small separation and brightness, a high-contrast imaging technique that suppresses the primary star's light is required. Also, an adaptive optics is employed to improve the seeing to resolve the planet in images.

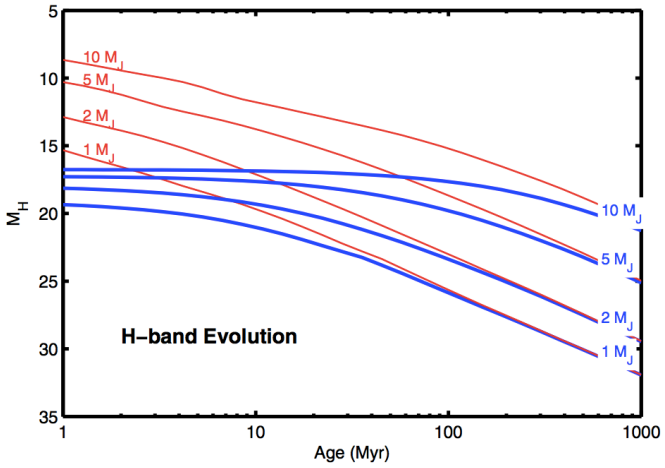

Figure 1.3: Luminosity evolutionary model of a gas giant in H-band (Spiegel & Burrows, 2012). Horizontal axis is the age of the planet (million year), and vertical axis its absolute magnitude in H-band. Red solid line represents hot-start model and blue solid line represents cold-start model.

The direct imaging method detects the thermal emission or reflection light of the planet. Note that reflection light of the planet is not directly detected so far due to the limited contrast of the current instruments. While the peak of the thermal emission of the planet is located from NIR to thermal infrared, the peak of the starlight is in the optical region. To minimize the contrast, the direct imaging observation is performed for the self-luminous companions in the near infrared region.

Since a direct-imaging observation enables us only to measure magnitude and separation of the planet, the mass of the planet detected by the direct imaging method is estimated by converting the magnitude of the planet using stellar evolutionary models of the low-mass object. Mass, magnitude, and age are closely related with each other, and its relation is summarized as a stellar evolutionary model or a stellar isochrone. Therefore age estimation of the system is important in this procedure where it is assumed that the ages of the companion and the primary are the same. In general, a younger object is much luminous than older one. The direct-imaging method is more sensitive to young objects. However, a young planetary mass object has a large mass uncertainties due to difference in models. Mainly two models that differ initial entropy conditions, hot-start or cold-start, are proposed for a planetary formation. Figure 1.3 shows that the difference of the hot-start and cold-start model for luminosity evolution of a planetary mass object. In this thesis, we do not consider the difference of two models because our samples are old enough (> 0.3Gyr) and there is no difference between two models.

Recently, a long-term (>5yr) observation reveals that the orbital motion of the planet detected by direct-imaging (e.g. Wertz et al., 2017). The measurement of the orbital motion offers us not only the measurement of Keplerian elements, but also estimation of dynamical mass. In this thesis, our observations for a target are at most three times in two years and this is not enough to fit the orbit. So we do not attempt the orbital fitting from the image.

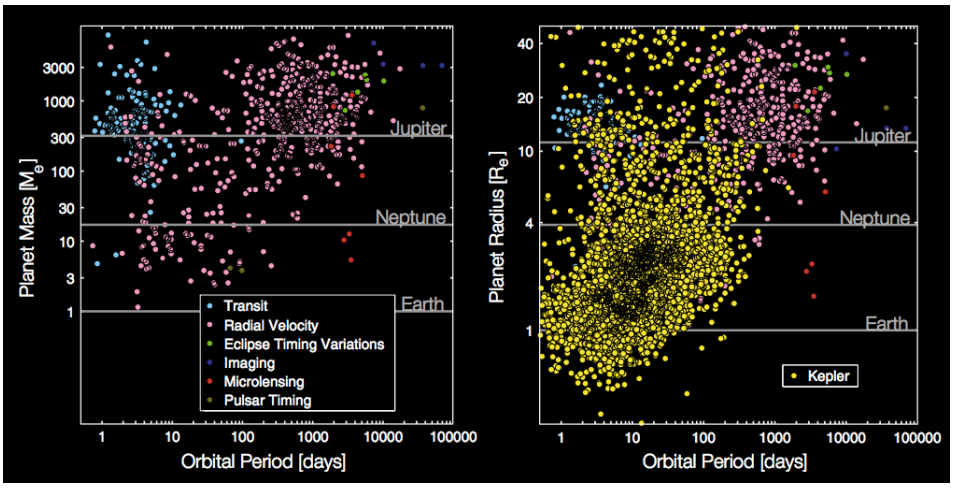

Figure 1.4: Comparison between non-Kepler exoplanet discoveries and Kepler exoplanets (Fig.1 of Batalha, 2014).

1.2 Discovery results and occurrence rate of exoplanets

The content of this section is more like "Recollection of the discoveries made by the indirect method".

1.2.1 Summary of discovery results and occurrence rate

Since the discovery of 51 Peg b in 1995, over 3500 exoplanets have been discovered by the RV method, transit method, direct-imaging method,micro-lensing method, and other methods (e.g. pulsar timing method). In an early stage of discovery of exoplanets, the RV method revealed that the existence of short-period gas giants, called hot Jupiters. The discovery of these hot Jupiters revealed the frequency of short period giant gas planets around the FGK type star, which is the main target of the RV method. For example, Cumming et al. (2008) estimated that frequencies of planets with $0.3 > M_{\rm J}$ and P$<$ 2000 days are 10.5%, using Keck/HIRES targeting for 585 stars. The frequency of the giant gas planet ($a < 2.5$ au) is estimated to be 3 % around the M type star, 8.5 % around the FGK type star, and 20 % around the A type star (Johnson et al., 2010) . It is suggested that the frequency of the giant gas planet increases in proportion to the mass of the main star.

The Kepler telescope launched in 2009 observed a field of 10 $\times$ 10 square-degrees for four and a half years with the transit method. The Kepler telescope discovered more than 2000 planets with precise transit photometry over four years and found 4000 more planet candidates. Kepler further discovered the earth - sized habitable planet like Kepler 186 f (Quintana et al., 2014), and discovered many close-in Earth size planets (Figure 1.4). As a result, the frequency of the Earth-like planet of 1 $R_\oplus$ and the frequency of super-earth of 1.5-2 $R_\oplus$ was obtained. Dressing & Charbonneau (2015), using Kepler's all data, suggested the frequency of Earth-like planets with a period of 50 days or less around the M-type star are found to be 0.56, and those in the habitable zone are 0.16.

While the RV method and the transit method revealed the presence and nature of

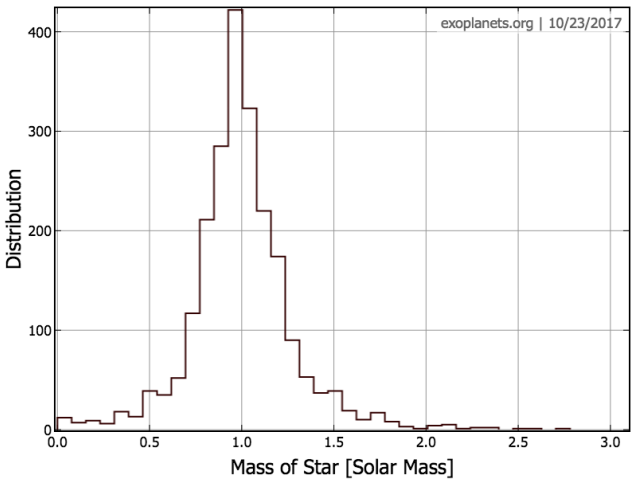

Figure 1.5: Histogram of discovered planets classified by host star mass.

a close-in planet, lensing those of distant planets is becoming apparent with the direct imaging method and micro-lens method. Direct imaging can detect substellar companion far from 20-300 AU. As a result of more than 10 years observations it has become clear that the frequency of giant gas planets in the distance is less than 5% (Galicher et al., 2016; Vigan et al., 2017). By micro-lensing method, the giant gas planet in the range of 0.5 - 10 AU, is estimated to be 17%, furthermore the ice giant like Neptune is 52% and the super - Earth is 62% (Cassan et al., 2012).

1.2.2 RV survey for intermediate mass giants

Most of the researches we have introduced so far is the survey targeting the sun type stars and its result, and the nature of the planet around the intermediate mass star is not well understood yet (Figure 1.5). At Okayama Astrophysical Observatory, a team led by Dr. Bun'ei Sato (Tokyo Institute of Technology) has been conducting an RV survey targeting intermediate mass giants (1.5-5 $M_{\odot}$) with HIDES instrument from 2001 . Since the survey period has exceeded 10 years, more than 30 planets/brown dwarfs have been discovered so far. It is suggested that the discovery of these planets suggests that the planetary distribution around intermediate mass giants is different from those around the sun type stars. Sato et al. (2008) pointed out that a close-in planet does not exist around an intermediate mass giant, and planets around intermediate mass ($> 1.5\ M_{\odot}$) that are less than 1AU are rarely present constraint (Figure 1.6).

A survey around a medium mass star gives a limit to the planetary formation because the mass of the disk on which the planet is formed is proportional to that of the central star. As the mass of the central star increases ($0.1 M_{\odot}$ <M<$1.3\ M_{\odot}$), the frequency of the giant gas planet within 2.5 AU is increasing (Johnson et al., 2007), also in Bowler et al. (2010), the frequency of the giant gas planet (a< 3AU) around the mass giant ($1.5 \leq M/M_{\odot} \leq 2.0$) is greater (26%) than the solar star (5-10%).

1.3 Formation and migration theory

In this section, I summarize the theoretical work on the formation process of the planets.

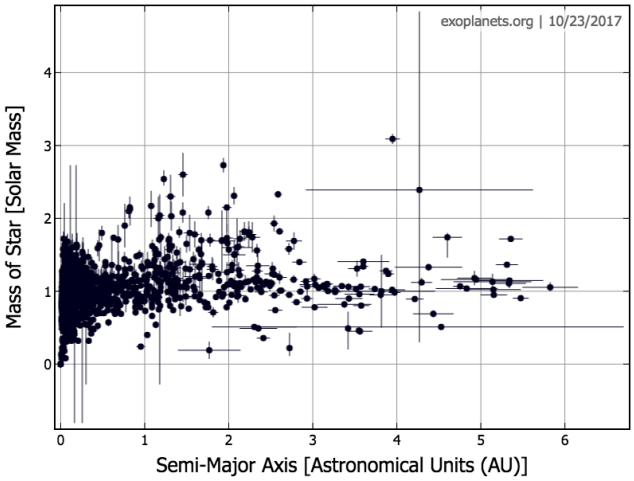

Figure 1.6: Discovered planet distribution of host star mass vs semi-major axis.

In the solar system Mercury exists at 0.4 AU. Venus (0.7 AU), Earth (1AU), Mars (1.5 AU) and these rocky planes are revolving inner side of the solar system. Jupiter is at 5 AU, and Saturn (10 AU) and the gas giant planets are located outside on the solar system. Furthermore, Uranus (19 AU) and Neptune (30 AU), i.e., the ice giants, are surrounding the outside. These eight planets have almost circular orbits with e <0.01 except Mercury (e = 0.2). A core-accretion model (e.g. Hayashi et al., 1985) was proposed as a model to explain the formation of the solar system. In this model, the planet is formed within a light disk whose protoplanetary disk mass is $\approx 0.01\ M_{\odot}$. Gas giant planets are formed via growing of planetesimals. When a protoplanet grows up to critical mass ($\sim 10\ M_{\rm Earth}$), it starts to accrete a gas envelope (Mizuno, 1980). Gas giants are formed beyond the snow line ($\sim$ 3-5 AU) where ices condense in the disk because disk surface density increases. Planet population synthesis based on the core accretion model can explain the observed mass-orbit, and mass distribution for planets up to several AU around solar type stars (Mordasini et al., 2009). With increasing the distance from the star, gas densities decrease, and it slows growth of a protoplanet. Therefore the core accretion theory has difficulties to explain formation of gas giants located beyond $\sim$ 20 AU (Kennedy & Kenyon, 2008) due to longer formation timescale than gas dissipation timescale ($\leq$ 10 Myr, e.g. Haisch et al., 2001).

On the other hand, the heavy ($\approx 0.1 M_{\odot}$) disk splits by self gravity to form a planet. This is called the gravitational instability model (e.g. Boss, 1997). The gravitational instability model can easily explain the distant gas giant planet formation. The instability condition is given by the Toomre Q value (Toomre, 1964),

$$Q = \frac{c_s \kappa}{\pi G \Sigma} \tag{1.3.1}$$

where c_s is the locas sound speed of the gas, κ is epicyclic frequency (equal to angular velocity in Kepler motion), Σ is the surface density of the disk, and $Q \leq 1$ indicates an instability of the disk. Thus the massive disks which have bigger surface density Σ can be gravitationally unstable at cool regions where the sound speed c_s is small. Recent gravitational instability model including migration process predicts that planets via gravitational instability emerge in 10 to several tens AU (e.g. Forgan et al., 2015;

Müller et al., 2018). The gravitational instability model is complementary to the core accretion model.

Many exoplanet systems that are different from the solar system are found. The biggest difference is that Jovian mass object is at less than 0.1 AU, this is called Hot Jupiter. Also there are planets with high eccentricity, called eccentric planet. Since the core-accretion model explains that a gas giant is formed outside the snow line in a circular orbit , it can not make hot Jupiter planet or eccentric planet.

Planetary migration theories can solve this problem. The theories of migration of a gas giant are type II migration, planet scattering, and Kozai mechanism. Type II migraion is a theory in which a protoplanet is trapped in a gap created in a disk and falls inside with the gap (e.g. Lin et al., 1997). If the disk has viscosity, the disk loses its angular momentum with torque. The disk whose momentum has been lost moves inward. If there are gaps and there are protoplanets there, they will move inward with that gap. The planet made by this type II migration is a gas giant with a circular orbit that orbits around 0.05 AU. Type II migration explains the formation of hot Jupiter.

Planet scattering model predicts that if there are multiple gas giants, the orbit intersects by mutual gravitational interaction; one planet is repelled outside the system, and the remaining planets have large orbital eccentricity. This is called a jumping Jupiter model (e.g. Marzari & Weidenschilling, 2002). In the case of two planets, the condition under which the orbit crossing occurs can be understood analytically. In the case of three or more, planets scattering occurs suddenly in a finite time. This planetary scattering model explains the formation of eccentric planets which are currently observed.

When an outer inclined object exists, the orbital inclination and eccentricity of an inner object fluctuates due to the gravity perturbation from the outer object (Kozai, 1962). This is called the Kozai mechanism, or oscillation. The Kozai oscillation is occurred if the semi-major axis of an inner object $a_{\rm in}$ is too smaller than those of an outer object $a_{\rm out}$, and the orbital plane of the inner object is tilted more than 39.2 degrees to those of the outer object. Time scale of the Kozai oscillation, $P_{\rm Kozai}$ is calculated,

$$P_{\rm Kozai} \sim \frac{P_{\rm out}^2}{P_{\rm in}} \frac{M}{m_{\rm out}} \left(1 - e_{\rm out}^2\right) \tag{1.3.2}$$

where $P_{\rm out}, P_{\rm in}$ are orbital period of outer and inner object, respectively, M is the primary star mass, $m_{\rm out}$ is the mass of outer object, and $e_{\rm out}$ is the eccentricity of outer object. If the time scale of Kozai oscillation is shorter than the age of the system, there is a possibility that the orbit of the planet was perturbed by the outer object. The Kozai oscillation also explains the formation of eccentric planets.

1.4 RV trend

As a result of the previous RV surveys, a long-term RV accelerations, called RV trends, are seen in some targets (Figure 1.7). The long-term RV acceleration (RV trends) of a host star is useful information for uncovering possible planetary companions in wide orbits. If a companion exists beyond ∼10 AU from the host star, the companion generates an almost linear trend in the RV of the host star within a relatively short period. The slope of the trend depends on the mass and the semimajor axis of the RV trend generator (RVTG), and we can estimate its minimum mass based on the following relation:

$$M_p \sin i = \frac{\dot{v} a^2}{\rm G} \tag{1.4.1}$$

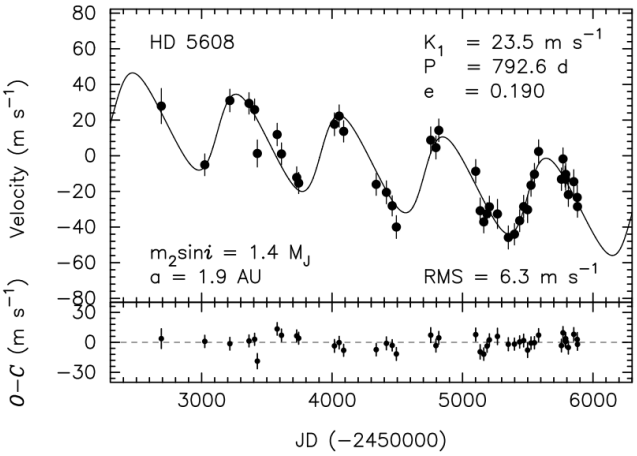

Figure 1.7: RV measurement result of HD 5608 (Sato et al., 2012)。A long-term decreasing RV trend is seen in addition to RV oscillation from planet (P=792 days).

where M_p is the RVTG mass, i is the orbital inclination, G is the gravitational constant, a is the semimajor axis of the RVTG, and $\dot{v}$ is the RV trend. For example, an RV trend of 10 m s^{-1} yr^{-1} corresponds to 5 $M_{\rm Jup}$, the minimum mass of the RVTG at a semimajor axis of 10 au. However, such an RV trend could just as easily be generated by a face-on or distant stellar companion or a brown-dwarf companion as a planetary one. A companion with M_p sin $i \sim 0.5$ $M_\odot$ located at 100 AU also yields an RV trend of 10 m s^{-1} yr^{-1} for the host star. Accordingly, the detection of the RV trend alone is not sufficient to identify the RVTG. Furthermore, the multiple rate of a solar type star is 46% (Raghavan et al., 2010), and those of A type main sequence star is 50% (Duchéne & Kraus, 2013). The false positive probability that an RV trend is generated by a stellar companion is not so low.

Direct imaging observations can solve this problem through confirming whether a stellar mass object exists in the distance. Even non-detection of any companions is useful for constraining the range of the mass and semimajor axis of an RVTG by a simultaneous analysis of the direct-imaging and RV-trend data (Figure 1.8).

One of the programs employing this idea, namely, combination of the direct imaging and the RV-trend observations, is TaRgetting bENchmark objects with Doppler Spectroscopy(TRENDS; e.g. Crepp et al. 2012) , which attempts to detect companions around FGKM-type stars showing RV trends. They discovered three low-mass stellar companions (Crepp et al., 2012), a tertiary stellar companion (Crepp et al., 2013a), a white dwarf companion (Crepp et al., 2013b), and a T dwarf (Crepp et al., 2014) using NIRC2/Keck telescope. Another similar program is MagAO Imaging of Long-period Objects (MILO) using MagAO/Magellan Telescope (Rodigas et al., 2016). The targets of TRENDS and MILO are mainly FGKM main sequence stars with RV trends. These projects are still on-going and the planet occurrence rate is not reported except for one sub-project called TRENDS IV by Montet et al. (2014). Montet et al. (2014) report a result of analysis of Doppler measurements of a sample of 111 M-dwarf stars and direct-imaging result of 4 targets with RV trends. Montet et al. (2014) determined that the distant ($0 < a < 20$ AU) gas giant ($1 < M_p < 13 M_{\rm Jup}$) occurrence rate around M dwarfs is 6.5 $\pm$ 3.0 %.

TRENDS project uses a relation between an RV trend slope and a separation of

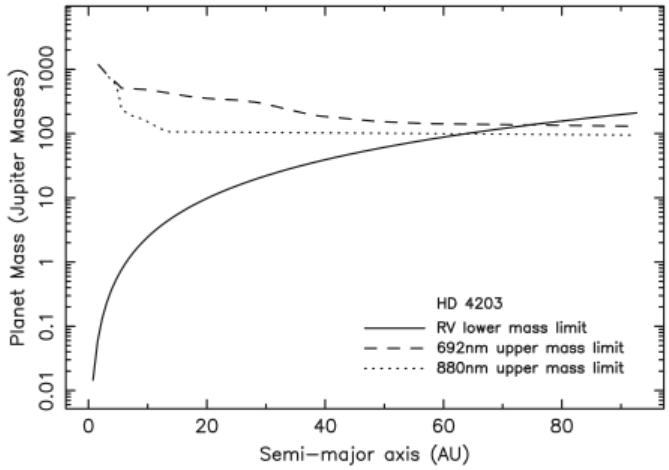

Figure 1.8: RVTG limitation by combining analysis of RV trends and speckle observation (Kane et al., 2014). Solid line represents the minimum mass derived from the observed RV trend. dashed line is the detectable mass limit. RVTG exists in the area surrounded by the solid line and the dotted line.

the companion derived by Torres (1999) to determine the lower mass from the RV trend. Rodigas et al. (2016) developed a new method that exploits some curvature and conducted a Markov chain Monte Carlo procedure to constrain orbital period, semi-major axis, and orbital inclination of the imaged companion. A similar approach, which uses RV data and direct imaging astrometric result is a software ExoSOFT developed by Mede & Brandt (2017). However, to combine RV data and direct imaging astrometric results, multi-epoch direct-imaging observations are required so that the companion movement is large enough compared with astrometric errors. Furthermore, this direct imaging technique also revealed that stars hosting a hot-Jupiter tend to be accompanied by a stellar companion (Knutson et al., 2014). These results clearly show that direct imaging observations can help us to explore and identify distant companions that generate RV trends of the host stars.

1.5 Purpose of the study

As a result of the 10 year RV survey targeting on GK type giants at the Okayama Astrophysical Observatory, several targets are already known that they have RV trends. Identifying the companions that generate the RV trend can improve our knowledge of exoplanet populations for intermediate-mass stars, which are poorly well understood compared to solar-type stars.

The planet distribution around intermediate mass stars is suggested to be different from that around solar type stars (Sato et al., 2008). Revealing the nature of distant planets around intermediate mass giants offers us a clue to test planetary formation theory. Especially, distant planets that can be the cause of RV trends give us information to distinguish which planetary formation theory is dominant for distant planets.

To clarify the sources of RVTGs around intermediate-mass stars observed in the OAO RV survey, we have performed direct-imaging observations as part of the Strategic Explo-

ration of Exoplanets and Disks with Subaru (SEEDS; Tamura 2009) project. The SEEDS project has discovered stellar companions around transiting planet systems (Narita et al., 2010, 2012; Takahashi et al., 2013), as well as planetary companions(e.g. Kuzuhara et al., 2013). While the TRENDS has targeted FGKM-type stars, our campaign focuses on intermediate-mass stars with RV trends and is therefore complementary to TRENDS.

In this study, we aim to identify the responsible objects causing the observed RV trends toward intermediate mass stars. The direct imaging technique is employed to search for the distant objects (both stellar companion and the planets). For the cases that the stellar companions are not detected, they are strong candidates of having planets to create the observed RV trends. In this way, we aim to discuss the occurrence rate of distant planets around intermediate mass giant stars and compare with that of the solar type stars. We also aim to discuss the formation scenario of distant planets around the intermediate stars.

Chapter 2

Method

In order to have a high angular resolution with a high dynamic range, we employed an ADI (Angular Differential Imaging) technique (Marois et al., 2006), and a LOCI (Locally Optimized Combination of Imaging) technique (Lafrenière et al., 2007).

After data reduction, we conducted a common proper motion test for several targets if a companion candidate existed. If the candidate had a common proper motion to the primary star, we estimated the companion mass derived from atmospheric model. Furthermore, we estimated a minimum mass that can make an RV trend. By combining it with the result of direct imaging, we restricted the existence range and mass of RVTG, or examined whether the detected companion star can cause the RV trend.

2.1 Angular Differential Imaging (ADI)

Since the stars rotate together with the diurnal movement, the star appears to rotate on the detector in the case of observation with am altitude-azimuth telescope. For normal observation, this rotation is offset by using Instrumental rotator or Imaging rotator. ADI observation is done without offsetting this rotation. While a object attached to a target star rotates on the detector together with the diurnal movement, speckle noise etc. that are derived from the telescope and optical system do not rotate. By synthesizing observation data with a median value, it is possible to create a reference image in which only noise that does not rotate remains. By subtracting the reference image of noise from data, the object attached to the target star remains, and the rotation of the diurnal motion is restored and synthesized, whereby a high contrast image can be obtained (Figure 2.1).

2.1.1 Locally Optimized Combination of Imaging (LOCI)

ADI offers us to easily obtain high contrast image, but since it makes a reference image from all data, it cannot cope with the temporal change of the center star and the time change of the speckle noise. To cope with these noises and to make the contrast higher, an analysis algorithm called Locally Optimized Combination of Imaging was proposed by Lafrenière et al. (2007) (Figure 2.2).

In LOCI algorithm, images are divided into small areas, linearly combined so as to minimize noise in each area, and a reference image is obtained. Each region is divided

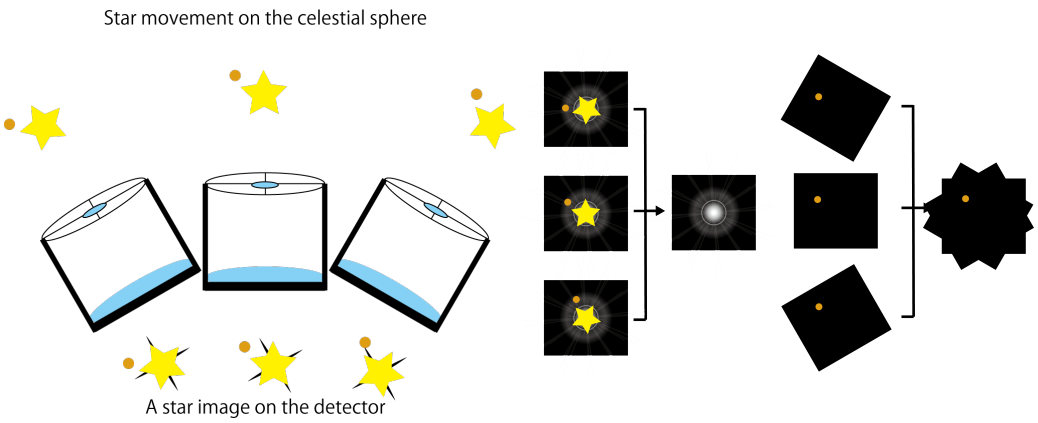

Figure 2.1: The conceptual image of the ADI method.

Table 2.1: Used LOCI parameters in this thesis

N_δ	0.75
N_A	300
g	1.0
dr	1.5-15 (1.5 ($< 60\lambda$/D, beyond that 15)

into a subtraction region S^T and an optimization region O^T so as to surround it. In order to minimize speckle noise in the optimization region O^T, O^T in all other frames are linearly combined with the least squares method to obtain a reference image. The reference image obtained in this way is subtracted only by S^T which is a part of O^T, and noise is removed. If O^T is smaller than the PSF of the companion star, it is regarded as noise and deducted. Therefore, the size of O^T depends on the size of PSF and how much the point source occupies O^T. The size of the optimized region, A is determined by

$$A = N_A \pi \left(\frac{W}{2}\right)^2 \tag{2.1.1}$$

where N_A is a LOCI parameter indicating how many times the optimized area is to be multiplied by the PSF, and W is the full width at half maximum of the PSF.

When dividing an image into a circle, since the noise level is different between the inside and the outside, the subtraction area S^T is set inside. At this time, the subtraction area S^T has an inner radius of r, an angle of ϕ, a radius width of dr and an angle width of $\Delta\phi$. The inner radius of the optimized region O^T is also r, the radius width is Δr, and the azimuth width is $(r + \Delta r/2)\Delta\phi$. A is also written as

$$A = \Delta r \, (r + \Delta r/2) \, \Delta\phi \tag{2.1.2}$$

Here the ratio of the radial width to the angular width of the optimized region g is determined by

$$g = \frac{\Delta r}{(r + \Delta r/2) \, \Delta\phi} = \frac{\Delta r^2}{A} \tag{2.1.3}$$

From this, Δr and $\Delta\phi$ can be determined by g and N_A and the full width at half maximum W of PSF,

$$\Delta r = \sqrt{\frac{\pi g N_A W^2}{4}} \tag{2.1.4}$$

$$\Delta\phi = \left(\frac{g}{2} + \frac{2r}{W}\sqrt{\frac{g}{\pi N_A}}\right)^{-1} \tag{2.1.5}$$

Therefore the parameters N_A, g, W are determined, the division parameter is also determined.

Note that we should be careful for self-subtraction due to insufficient rotation in ADI observation. When the rotation is insufficient, signals of objects are recorded in plural files in one optimized area (Figure 2.3). In such a case, the signal of the object is regarded as noise and it is deducted, becoming darker than the original brightness. Therefore, the minimum moving amount, $\delta_{\min}$, is

$$\delta_{\min} = N_\delta W + r\delta\theta_n \tag{2.1.6}$$

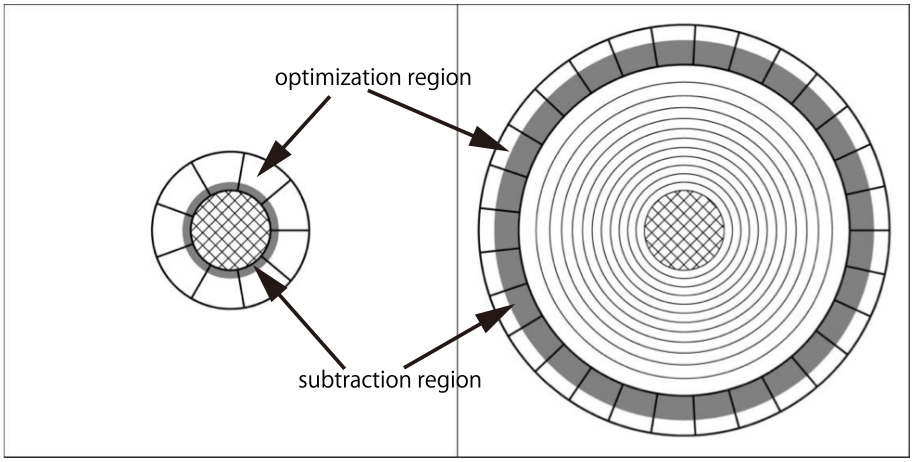

Figure 2.2: The conceptual image of subtraction area (gray) and optimization are (inside solid lines) of LOCI algorithm. The original image in Lafrenière et al. (2007) and revised by the author.

where N_δ is LOCI parameter, and $\delta\theta_n$ is rotation angle in exposure time n. To evaluate the effect of this self-subtraction in this analysis, the artificial star was embedded in the image after LOCI process was completed, and the effect of self-subtraction was estimated (Figure 2.4).

The LOCI parameters used in the analysis are shown in the table 2.1. These values were same as Lafrenière et al. (2007) except for N_δ.

2.2 Bad pixels

There are pixels whose count number is abnormally large on HiCIAO detector even the shutter does not open as a dark frame (Figure 2.5). This is called badpixel. Before analyzing, it is necessary to mask the bad pixel part with a mask. In the bad pixel of HiCIAO detector, as shown in the figure 2.5, pixels with a large number of counts cause leakage of electrons to the surroundings, which are cross shaped or rectangular. This cross-shaped part has a lower count number than the center part of the cross. However, since the number of counts in the center part is very high, the standard deviation is in this state is large, and in this state, if the pixel count exceeding 5 σ is marked as bad pixel, a bad pixel with a slightly larger count is not recognized as a bad pixel. Therefore, firstly, very high bad pixels were detected, a bad pixel mask was made, masked, and standard deviation was measured again to detect bad pixels.

The procedure for creating a bad pixel mask is as follows. The HiCIAO raw data has striped patterns as shown in the figure 2.6. First, average and standard deviation are calculated for each stripe. Look for points exceeding 5 *sigma* for each stripe and mask each. Using ACORNS module (Brandt et al., 2013), we create a provisional flat using this bad pixel mask. Flat correction is performed using this flat, bad pixel mask is applied, average value and standard deviation are calculated, and the position of the bad pixel is determined. Then, a final bad pixel mask is obtained. I made this bad pixel mask with Dr. Masayuki Kuzuhara (Astrobiology Center).

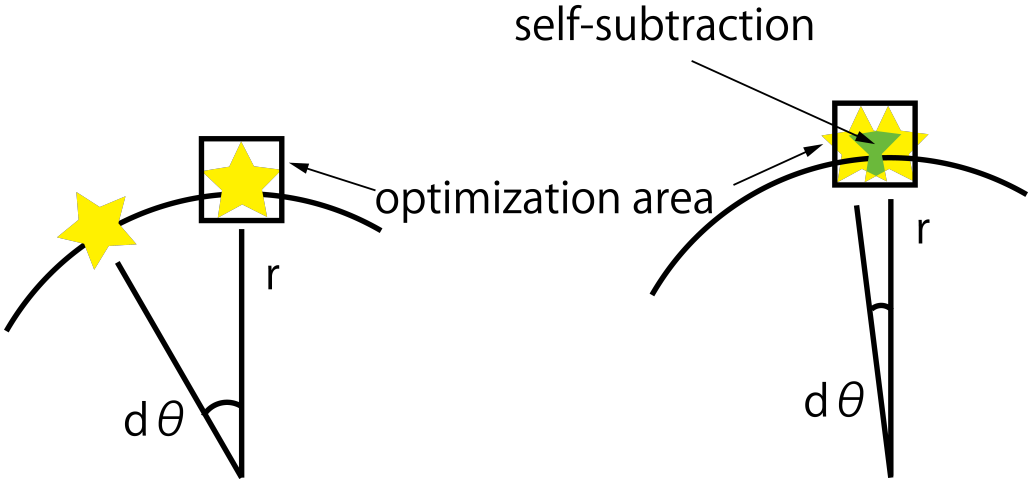

Figure 2.3: The conceptual image of self-subraction.

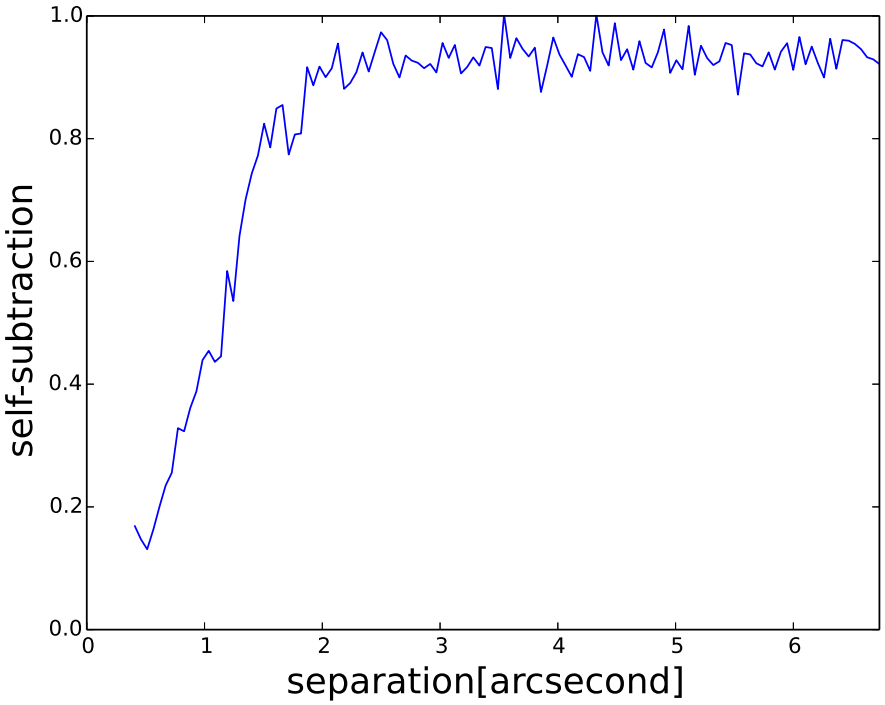

Figure 2.4: The effect of self-subraction. The original brightness is normalized. The self-subtraction is effective for inner region.

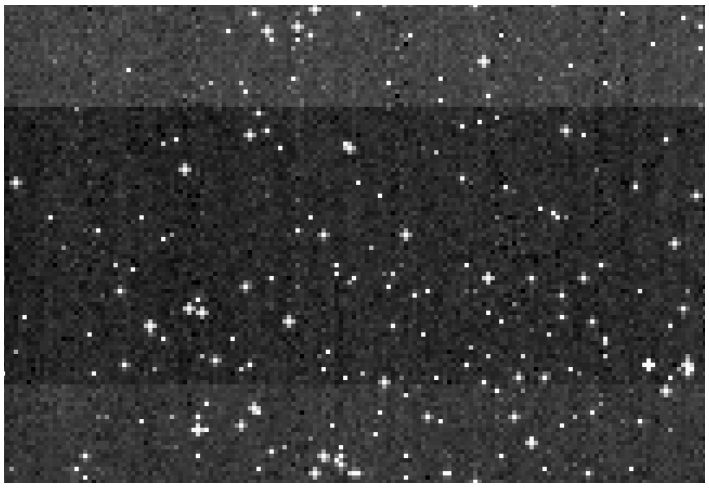

Figure 2.5: Bad pixels on HiCIAO detector in a dark frame.

2.3 Analysis procedure for HiCIAO data

In this analysis, we used modified ADI and LOCI analysis pipeline made by Dr. Masayuki Kuzuhara and Dr. Yasuhiro Takahashi for HiCIAO data distributed in SEEDS.

In the raw data obtained by HiCIAO, there is a striped pattern like the figure 2.6. First of all, stripe subtraction was done for both the science images and the reference images. Next, flat correction and distortion correction were performed for the reference image without moving the position. The position of the central star and the full width at half maximum were measured with respect to the reference image subjected to this correction. The difference between the position of this central star and the center coordinate (1024, 1024) on the HiCIAO detector is obtained (if the position is measured by IRAF, the difference from 1025). Science frame was shifted by the difference, and flat correction and distortion correction were performed at the same time. Enter the full width at half maximum used for the LOCI parameter, calculate the radial profile of each image, and subtract halo. The processed image was processed with LOCI to obtain the final image. After this, the artificial star was embedded in the final image, and the influence of self-subtraction was estimated. We also calculated the S / N map for the final image.

Further, the contrast obtained by LOCI analysis is calculated from the obtained final image. we checked the achieved 5σ contrast ratio $C(r)$ by calculating the standard deviation within 2 pixel wide rings, from the center to the outer region every 4.5 pixels. $C(r)$ is calculated by

$$C(r) = \frac{5\sigma}{S(r) \int_{\mathrm{FWHM}} F_* dS} \tag{2.3.1}$$

where $S(r)$ is percentage dimmed by self-subtraction in r, F_* is stellar flux. In this thesis, the flux of the star was measured in aperture photometry with FWHM of the star using the unsaturate image with neutral density (ND) filter for position reference. Transmittances of the ND filter was measured precisely by observation of SEEDS in the past, and its value was used (Table 2.2). In the unsaturate frame, the position was also measured, and the standard deviation of the position of the central star was assumed to be an error in position measurement of the companion star candidate.

Table 2.2: Transmittances of ND filters installed at HiCIAO in H-band

ND10	9.740% ± 0.022%
ND1	0.854% ± 0.002%
ND0.1	0.063% ± 0.020%
ND0.01	0.016% ± 0.001%

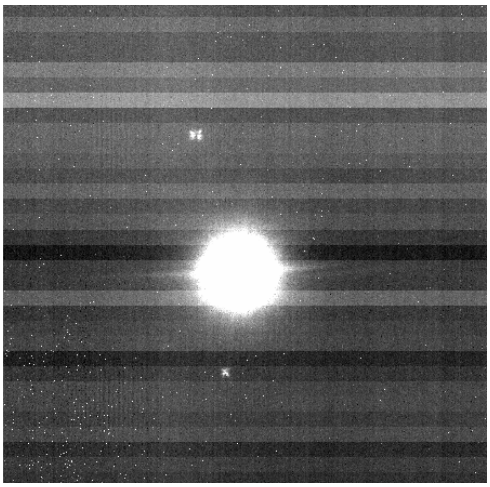

Figure 2.6: Stripe patters on HiCIAO raw data frame.

2.4 Common proper motion test

The detected companion star candidate has a possibility not to be a gravitatively constrained companion star, but be a background star. For this reason, we made follow-up observations to confirm whether the companions have common proper motion to the primary stars. In the case of the background star, since the proper motion of the background star can be regarded to be negligibly small, the relative position between the main star and the companion candidate star changes. On the other hand, in the case of a companion star which is gravitationaly bound to the primary star, the relative position between the main star and the companion candidate star hardly changed because the orbital motion of the companion at tens au can be ignored during the observation period of several years (Figure 2.7). In order to detect the background star's motion significantly, considering the pixel scale of the telescope, we should observe for follow-up observation Δt later from the first observation,

$$\Delta t \geq \frac{\text{pixel scale}}{\sqrt{\mu_\alpha^2 + \mu_\delta^2}} \tag{2.4.1}$$

where μ_α is proper motion of right ascension, and μ_δ is proper motion of declination. It is possible that the companion candidate is foreground star, however, the probability is considered extremely low because target in this thesis is almost located within 100 pc.

Stellar motion of right ascension,$\Delta\alpha$, and declination $\Delta\delta$ considering parallax ($\Delta\alpha_{\text{parallax}}$, and $\Delta\delta_{\text{parallax}}$) on the image is represented as sum of μ_α,μ_δ, $\Delta\alpha_{\text{parallax}}$, and $\Delta\delta_{\text{parallax}}$

$$\Delta\alpha = \mu_\alpha + \Delta\alpha_{\text{parallax}} \tag{2.4.2}$$

$$\Delta\delta = \mu_\delta + \Delta\delta_{\text{parallax}} \tag{2.4.3}$$

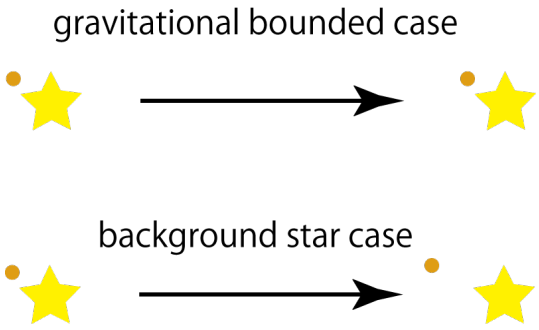

Figure 2.7: Conceptual image of common proper motion test.

Parallax is calculated as

$$\Delta\alpha_{\mathrm{parallax}} = \frac{1}{\cos\delta}\varpi\left(-\sin\alpha\cos L_{\odot} + \cos\alpha\sin L_{\odot}\cos\varepsilon\right) \tag{2.4.4}$$

$$\Delta\delta_{\mathrm{parallax}} = \varpi\left(-\cos\alpha\sin\delta\cos L_{\odot} - \sin\alpha\sin\delta\sin L_{\odot}\cos\varepsilon + \cos\delta\sin L_{\odot}\sin\varepsilon\right) \tag{2.4.5}$$

where α, δ is the coordinate of right ascension, and declination, $L_{\odot}$ is ecliptic longitude at observed time, ε is obliquity of the ecliptic, and ϖ is amplitude of annual parallax that is calculated as

$$\varpi = \frac{a}{d} \tag{2.4.6}$$

where a is the distance between Sun and Earth, and d is the distance to the star.

2.5 Estimation of mass and calculation of detection limit

Generally, in the direct imaging method, since the distance between the primary star and the companion is large, the mass of the companion star cannot be obtained from the orbital motion in few years observations. In that case, we estimate the mass from the flux of the object using the atmospheric model.

In a low mass star that a hydrogen nuclear fusion reaction cannot occur, light is emitted by deuterium combustion or Kelvin / Helmholtz contraction. After the deuterium burning, the luminosity decreases gradually as the temperature decreases. That is, age and luminosity are required for estimating the mass of low mass objects. Assumed the age of the companion star is considered to be the same as the age of the main star, we can estimate mass of a low mass object if luminosity information is obtained. It is the atmospheric model that studied about the luminosity evolution of a low mass object.

In this thesis, we adopted COND model (Baraffe et al., 2003) and NextGen model (Hauschildt et al., 1999a). The COND model is a model that takes into consideration that metal components are removed from the gas by condensation, which is well explain T type brown dwarf. The NexTGen model is an atmospheric model without dust.

Detection limit is estimated as below. We converted the obtained contrast ratio $C(r)$ to the absolute magnitude of M, using absolute magnitude M_H in the H-band of the primary star.

$$M = -2.5\log_{10}\left(C(r)\right) + M_H \tag{2.5.1}$$

Then, we converted the absolute magnitude of the object to mass using COND model, and regarded it as detection limit. We also used PARSEC isochrones (Bressan et al., 2012) for NESSI/WIYN data because these detection limits is on evolved stars mass. For the case of a detected companion, we adopted NextGen model to derive companion's mass.

Chapter 3

Observations

For this thesis, I used the data which is a part of the SEEDS survey from 2011-2014 (Tamura, 2009) using the High Contrast Instrument for the Subaru Next Generation Adaptive Optics (HiCIAO; Suzuki et al. 2010) on the 8.2 m Subaru Telescope. In addition, I obtained WIYN data obtained in 2017. RV observations at OAO identified thirty two intermediate-mass giants with RV trends. In order to clarify the objects that cause the RV trends, we observed the thirty two giants via direct imaging.

3.1 HiCIAO and AO188

In this section, I summarize three important components for the observations, AO188, ADC, and HiCIAO. HiCIAO and AO 188 are installed in the infrared Nasmyth focus of the Subaru telescope with an effective aperture of 8.2 m located at the summit of Mauna Kea (altitude 4,200 m) in Hawaii, USA.

3.1.1 AO188

In the case of ground telescopes, light from the star is distorted by atmospheric fluctuations and become larger. It is adaptive optics (AO) that suppresses deterioration of the star image caused by this atmospheric fluctuation. In AO 188, the distortion of the star image is detected by the wavefront sensor, and the deformable mirror cancels the distortion by the wavefront correction mirror, thereby the star image deteriorated by atmospheric fluctuation is restored (Hayano et al., 2008). The seeing size at the summit of Mauna Kea is about $0.4''$ at the best time, but as a result of adaptive optics performed by AO 188, the seeing size is improved to 0.06 $''$ (2 μ m).

Schematic view of AO188 is shown in Figure 3.1. The reference star to measure the wavefront is observed in the R band in AO188. The reference star is required brighter than R$\leq$15. For an object magnitude of R $>$ 15, adaptive optics is performed by the artificial star created by laser.

3.1.2 Atmospheric Dispersion Corrector (ADC)

Due to the atmosphere, the short wavelength side is refracted more than the longer wavelength side (Figure 3.2). The star image becomes large like the ellipse with the horizon direction on the red side and the zenith direction on the blue side. As the observation elapses, the altitude changes and the magnitude of the refraction changes so that the position of the star image moves. Therefore, the star image deteriorates more than the diffraction limit and the positional shift occurs. In the case of observations with AO to achieve the diffraction limit, this effect, atmospheric dispersion, should be corrected. Atmospheric Dispersion Corrector (ADC) is to correct this atmospheric difference.There is ADC in AO 188, and we correct the atmospheric difference using a prism (Egner et al., 2010).

3.1.3 HiCIAO

The High Contrast Instrument for the Subaru Next Generation Adaptive Optics (HiCIAO) is direct imaging method instrument installed at Subaru telescope infrared Nasmyth focus (Tamura et al., 2006; Suzuki et al., 2010). HiCIAO observations are carried out with AO 188 because bad seeing condition prevent to detect a faint object.

HiCIAO's design concept is shown in Figure 3.3. First, light from the telescope is passed through AO 188 to improve the seeing. Next, the light passes through the

Table 3.1: The properties of HiCIAO detector (Suzuki et al., 2010).

Gain	1.60 e^-/ADU
Readout noise	15 e^-
Wavelenth coverage	z, J, H, Ks
detector	HAWAII-2RG
number of pixels	2048×2048
pixel scale	9.5 milli-arcsec/pixel
detection limit (1 hour exposure)	24.05 (J), 23.69 (H), 22.17 (K) mag

coronagraph part, and in the case of observation using the coronagraph, the central star is blocked by the coronagraph here. After that, light reaches the detector via a collimating lens and a Wollaston prism that splits the light. HiCIAO detector uses 2048×2048 HgCdTe HAWAII-2RG, and Table 3.1 shows the detector characteristic. HiCIAO is designed to achieve contrast of 10^{-4} at 0.1arcsec, and $10^{-5.5}$ at 1 arcsec.

In addition to the normal direct imaging mode (DI), HiCIAO has three different imaging modes to achieve high contrast, Polarimetric Differential Imaging (PDI), Spectral Differential Imaging (SDI), and Angular Differential Imaging (ADI). The PDI mode is an observation mode using polarized light. Since the speckle noise from the primary star is unpolarized light, information of polarized light due to scattering of dust in the protoplanetary disk can be extracted by subtracting the two linear polarized components. The SDI mode is an observation that subtracts characteristic spectrum of brown dwarfs or gas giants, for example, a narrow band filter that transmits only methane, to detect brown dwarfs and gas giants. A object with a characteristic spectrum becomes brighter with a narrow band filter, and the primary star which does not have a characteristic spectrum and the noise are the same brightness as in other filters. By taking the difference, brown dwarfs and gas giants can be detected. The ADI mode is an observation method using rotation on the detector due to the diurnal motion of the star. Details was described in the analysis. The ADI mode can be combined with other observation modes like PDI + ADI, SDI + ADI. In each observation mode, the size of the field of view is different as shown in the figure 3.4. The field of view in ADI and DI mode is $20'' \times 20''$, in PDI mode is $20'' \times 10''$, and in SDI mode is $5'' \times 5''$.

3.2 WIYN telescope and NESSI instrument

WIYN telescope is 3.5m diameter telescope located at Kitt Peak National Observatory in Arizona, USA. NESSI is acronym of the NASA Exoplanet Star (and) Speckle Imager installed at WIYN telescope (Howell et al., 2011; Scott et al., 2017). In speckle image mode, NESSI has a Andor iXon Ultra 888 electron multiplying CCDs (EMCCDs) 256 × 256 pixels and 4.6 × 4.6 arcsecond field of view. Speckle observations also enable us to improve seeing to detect close in stellar companions.

3.3 Okayama Astrophysical Observatory 188cm Telescope and HIDES instrument

We obtained RV data for the targets, except for ι Dra, with the 1.88m telescope and the High Dispersion Echelle Spectrograph (HIDES; Izumiura, 1999) at OAO between 2001

and 2016. We used an iodine absorption cell (I_2 cell; Kambe et al., 2002) for precise RV measurements, which provides a fiducial wavelength reference in a wavelength range of 5000–5800 Å. We used the HIDES-slit mode setting with a slit width of the spectrograph of 200 μm (0.76″), which corresponds to a spectral resolution ($R = \lambda/\Delta\lambda$) of 67000 with $\sim$ 3.3-pixel sampling. Reduction of the echelle data (i.e., bias subtraction, flat-fielding, scattered-light subtraction, and spectrum extraction) was performed using the IRAF software package.

For precise RV analysis, we modeled I_2-superposed stellar spectra (star+I_2) by the method detailed in Sato et al. (2002, 2012), which is based on the method by Butler et al. (1996) and Valenti et al. (1995). In the method, a star+I_2 spectrum is modeled as a product of a high resolution I_2 and a stellar template spectrum convolved with a modeled instrumental profile (IP) of the spectrograph. The stellar template spectrum is obtained by deconvolving a pure stellar spectrum with an IP estimated from a B-star or flat spectrum taken through an I_2 cell. We achieved a long-term RV precision of about 4 m s^{-1} over the entire span of the observations. The measurement error was derived from an ensemble of the velocities from each of the $\sim$300 spectral segments (each $\sim$3Å long) in every exposure. The RVs for 18 Del were updated and extended from those presented in Sato et al. (2008). The RVs for HD 5608 and HD 14067 presented in Sato et al. (2012) and Wang et al. (2014), respectively, were used for the analysis in this thesis.

3.4 Observation targets

We have selected thirty one targets with RV trends from the OAO survey 322 samples, and one target with an RV trend reported by Zechmeister et al. (2008) and Kane et al. (2010). **For the thirty one targets from the Okayama RV survey, we selected our RV trend samples as $>$ 10 m s^{-1} shifts in observation periods (^{s}im 10 years). Approximately 1 m s^{-1} yr^{-1} corresponds to a 1.5 $M_{\rm Jup}$ planet located at 10 AU where orbital period is more than 20 years. Also, we excluded the stars that showed 500 m s^{-1} shifts in observation periods because the trend generator's mass of 50 m s^{-1} yr^{-1} is more than 72 $M_{\rm Jup}$ (brown dwarf boundary mass). Some dozens stars in fact show a significant RV shift ($>$ 500 m s^{-1}), which indicates that stellar companions exist.** Note that the OAO survey has discovered over 30 planets/brown dwarfs and the widest orbit of them is 5 au (or a period of 2732 days 7.5 year) (Sato et al., 2013a). The rms of RVs of remaining targets is typically $\sim$ 10 m s^{-1} and $<$ 50 m s^{-1} . Therefore we could miss 5 m s^{-1} yr^{-1} trend that corresponds to a $\sim$ 7 $M_{\rm Jup}$ planet located at 10 AU.

Tables 3.2 - 3.8 show the stellar properties of our thirty two targets. Note that five of the targets have already-known RV planets (Table 3.9).

Table 3.2: Stellar properties of targets observed by HiCIAO in SEEDS project

Property	γ Hya	ι Dra	18 Del	HD 5608	HD 14067	HD 109272
Other name	HD 115659	HD 137759	HD 199665	HR 275	HR 665	HR 4779
R.A. (J2000) [a]	13:18:55.297	15:24:55.775	20:58:25.934	00:58:14.219	02:17:10.440	12:33:34.258
Dec. (J2000) [a]	-23:10:17.45	+58:57:57.83	+10:50:21.43	+33:57:03.18	+23:46:04.18	-12:49:48.73
J (mag) [b]	1.519 ± 0.278	1.293 ± 0.220			4.718 ± 0.037	4.151 ± 0.280
H (mag) [b]	1.065 ± 0.266	0.724 ± 0.146	3.44 ± 0.08	3.89 ± 0.05	4.448 ± 0.220	3.616 ± 0.226
K (mag) [b]	1.024 ± 0.300	0.671 ± 0.200			4.097 ± 0.036	3.600 ± 0.250
Distance (pc) [c]	41.0 ± 0.2	31.0 ± 0.1	75 ± 1	56 ± 1	163 ± 13	49.3 ± 0.8
μ_α (mas/yr) [a]	68.99 ± 0.17	-8.36 ± 0.08	-48.75 ± 0.33	34.98 ± 0.40	-32.57 ± 0.48	-17.64 ± 0.28
μ_δ (mas/yr) [a]	-41.85 ± 0.09	17.08 ± 0.10	-34.43 ± 0.17	-71.87 ± 0.20	-42.21 ± 0.44	52.09 ± 0.19
Mass ($M_\odot$)	$2.94\ ^{+0.03}_{-0.06}$ [d]	1.82 ± 0.23 [e]	$2.25\ ^{+0.05}_{-0.06}$ [d]	1.55 ± 0.11 [d]	2.4 ±0.2 [f]	1.79 ± 0.11 [d]
Sp. type	G8III	K2III	G6III	K0IV	G9III	G8III/IV
[Fe/H]	-0.04 ± 0.04 [d]	0.07 ± 0.08 [g]	-0.05 ± 0.04 [d]	0.06 ± 0.05 [d]	-0.10 ± 0.08 [f]	-0.26 ± 0.02 [d]
$T_{\rm eff}$ (K)	5019 ± 20 [d]	4545 ± 110 [e]	4985 ± 18 [d]	4854 ± 25 [d]	4815 ± 100 [f]	5104 ± 10 [d]
Age (Gyr)	$0.37\ ^{+0.03}_{-0.01}$ [d]		0.79 ± 0.05 [d]	$2.5\ ^{+1.4}_{-1.0}$ [d]	0.69 ± 0.20 [f]	$1.4\ ^{+0.3}_{-0.1}$ [d]

a Refined data reduction of *Hipparcos* (van Leeuwen , 2007)
b 2MASS catalogue (Cutri et al., 2003)
c The parallax-based distance from *Hipparcos* uses van Leeuwen (2007)
d Takeda et al. (2008)
e Baines et al. (2011)
f Wang et al. (2014)
g da Silva et al. (2011)

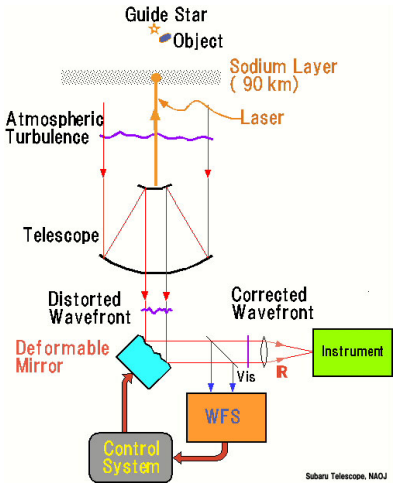

Figure 3.1: The conceptional image of adaptive optics. https://www.subarutelescope.org/Pressrelease/2006/11/20/index.html

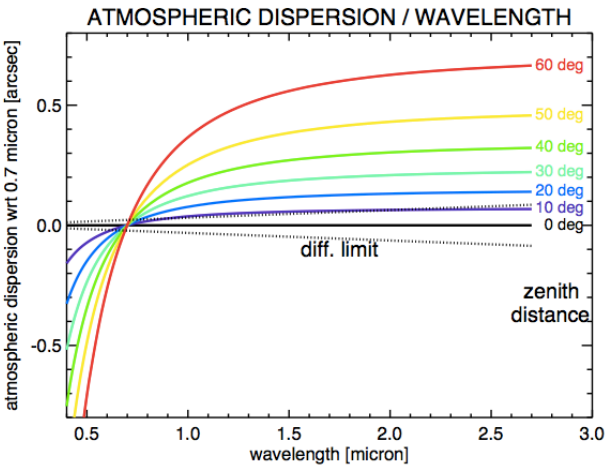

Figure 3.2: The magnitude of atmospheric dispersion in 0.7μm(Egner et al., 2010). Each line represents the zenith angle.

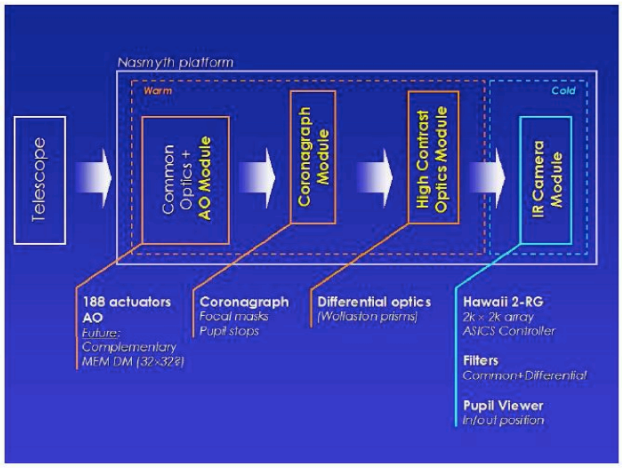

Figure 3.3: Conceptual image of HiCIAO(Tamura et al., 2006)

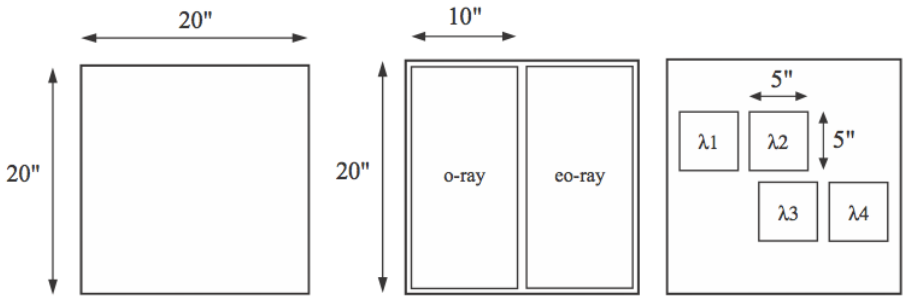

Figure 3.4: Field of view of HiCIAO in each mode(Suzuki et al., 2010). (Left) ADI and DI mode, (middle) PDI mode, (right) SDI mode.

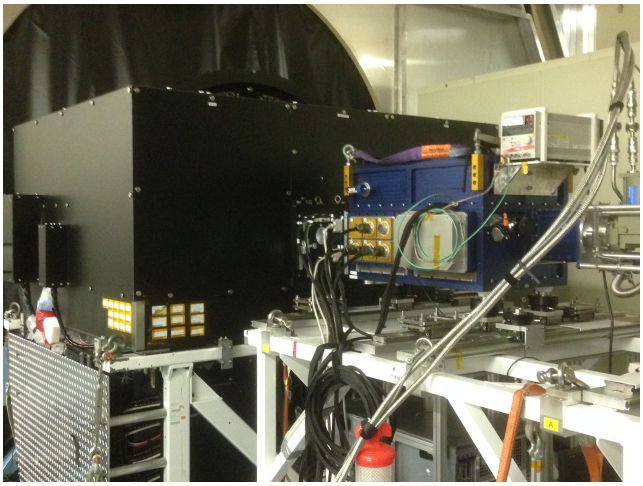

Figure 3.5: HiCIAO (blue box) and AO188 (black box) at the Nasmyth focus of the Subaru Telescope

S

Table 3.3: Stellar property of targets observed in Dec. 2015

Property	χ Cas	HD 27971	HD 39007	HD55730	ι Cnc A
other name	HD 9408				HD74739
R.A. (J2000)[a]	01 33 55.877	04 26 06.310	05 50 02.686	07 14 32.621	08 46 41.820
Dec. (J2000) [a]	+59 13 55.35	+31 26 20.08	+09 52 16.37	+12 06 56.98	+28 45 35.62
J (mag) [b]	3.019±0.200	3.790±0.294	4.284±0.01	4.204±0.302	2.368±0.244
H (mag)[b]	2.481±0.164	3.370±0.250	3.862±0.01	3.553±0.262	1.941±0.192
K (mag) [b]	2.311±0.218	3.199±0.362	3.749±0.01	3.470±0.244	1.831±0.236
distance (pc) [c]	63.8±1.5	77.6±1.9	109.8±8.0	90.2±2.3	101.5±6.2
μ_α (mas/yr) [a]	-43.03±0.34	76.79±0.37	15.59±0.68	-49.78±0.32	-21.58±0.75
μ_δ (mas/yr) [a]	-22.31±0.32	-121.57±0.28	-2.99±0.48	-16.07±0.23	-45.69±0.56
Mass ($M_\odot$) [d]	2.04±0.15	$2.56^{+0.11}_{-0.20}$	2.55±0.10	$2.33^{+0.13}_{-0.43}$	$3.43^{+0.30}_{-0.19}$
Sp. Type	K0 III	K1 III	G8 III	G6 III	G8 Iab
[Fe/H]	-0.34	+0.05	+0.08	-0.17	-0.06
Age (Gyr)	1.00±0.10	$0.58^{0.07}_{0.04}$	0.54±0.02	$0.72^{0.20}_{0.04}$	$0.26^{+0.02}_{-0.03}$

a The refined data reduction of *Hipparcos* (van Leeuwen , 2007)
b 2MASS Catalog(Cutri et al., 2003)
c The parallax-based distance from *Hipparcos* uses van Leeuwen (2007)
d Takeda et al. (2008)

Table 3.4: Stellar property of targets observed in Dec. 2015 II

Property	ζ Crt	HD 111028	β Boo	HD 360	HD 15920
other name	HD102070		HD133208		
R.A. (J2000)[a]	11 44 45.776	12 46 22.545	15 01 56.762	00 08 17.532	02 38 02.032
Dec. (J2000) [a]	-18 21 02.43	+09 32 22.87	+40 23 26.04	-08 49 26.80	+72 49 05.71
J (mag) [b]	3.170±0.302	4.174±0.282	1.90	4.28 ± 0.01 [e]	3.929 ± 0.262
H (mag) [b]	2.658±0.214	3.537±0.230	1.43	3.75 ± 0.01 [e]	3.476 ± 0.208
K (mag) [b]	2.558±0.266	3.442±0.260	1.34	3.65 ± 0.01 [e]	3.296 ± 0.306
distance (pc) [c]	108.2±6.9	45.14±0.71	69.06±0.66	98.4 ± 4.0	78.4 ± 1.4
μ_α (mas/yr) [a]	27.79±0.41	279.34±0.32	-40.15±0.12	-34.199 ± 0.028 [f]	-28.51 ± 0.20
μ_δ (mas/yr) [a]	-24.86±0.33	-453.41±0.25	-28.86±0.16	-35.106 ± 0.019 [f]	16.08 ± 0.22
Mass ($M_\odot$) [d]	$3.42^{+0.19}_{-0.18}$	$1.41^{+0.19}_{-0.23}$	$3.42^{+0.08}_{-0.11}$	$2.34^{+0.10}_{-0.27}$	$2.63^{+0.04}_{-0.03}$
Sp. Type	G8 III	K1III-IV	G8III	G8 III	G8III
[Fe/H]	+0.03	-0.05	-0.07	-0.08	-0.06
Age (Gyr)	0.25±0.01	$3.3^{+1.0}_{-0.6}$	0.25±0.01	$0.72^{+0.10}_{-0.04}$	0.51 ± 0.01

a The refined data reduction of *Hipparcos* (van Leeuwen , 2007)
b 2MASS Catalog(Cutri et al., 2003)
c The parallax-based distance from *Hipparcos* uses van Leeuwen (2007)
d Takeda et al. (2008)
e Laney et al. (2012)
f Gaia Collaboration et al. (2016)

Table 3.5: Stellar property of targets observed in Dec. 2015 III

Property	HD 4188	HD 64152	HD 18970	HD 120420
other name				
R.A. (J2000)[a]	00 44 11.400	07 51 43.025	03 05 32.412	13 48 38.735
Dec. (J2000) [a]	-10 36 34.38	-21 10 25.18	+56 42 20.59	+31 11 24.74
J (mag) [b]	3.07 ± 0.01 [e]	4.01 ± 0.01 [e]	3.014 ± 0.254	3.847 ± 0.282
H (mag) [b]	2.58 ± 0.01 [e]	3.58 ± 0.01 [e]	2.564 ± 0.194	3.291 ± 0.222
K (mag) [b]	2.46 ± 0.01 [e]	3.46 ± 0.01 [e]	2.398 ± 0.230	3.122 ± 0.348
distance (pc) [c]	71.6 ± 1.2	93.7 ± 2.8	64.7 ± 1.1	87.1 ± 2.1
μ_α (mas/yr) [a]	-8.96 ± 0.24	-45.59 ± 0.25	-12.72 ± 0.25	-5.628 ± 0.024 [f]
μ_δ (mas/yr) [a]	-113.82 ± 0.15	32.86 ± 0.19	70.04 ± 0.22	37.888 ± 0.017 [f]
Mass ($M_\odot$) [d]	$2.54^{+0.02}_{-0.57}$	$2.41^{+0.06}_{-0.07}$	$2.44^{+0.09}_{-0.45}$	$2.25^{+0.14}_{-0.28}$
Sp. type	K0IIIvar	K0III	K0II-III	K0III
[Fe/H]	-0.01	+0.07	-0.07	-0.20
Age (Gyr)	$0.56^{+0.22}_{-0.01}$	0.64 ± 0.02	$0.64^{+0.20}_{-0.03}$	$0.79^{+0.15}_{-0.05}$

a The refined data reduction of *Hipparcos* (van Leeuwen , 2007)
b 2MASS Catalog(Cutri et al., 2003)
c The parallax-based distance from *Hipparcos* uses van Leeuwen (2007)
d Takeda et al. (2008)
e Laney et al. (2012)
f Gaia Collaboration et al. (2016)

Table 3.6: Stellar property of targets observed in WIYN/NESSI

Property	HD 10348	HD 11949	HD 45415	HD 54810	HD 65228
R.A. (J2000)[a]	01 41 39.23	01 58 33.50	06 27 20.45	07 10 13.68	07 56 51.53
Dec. (J2000) [a]	+30 02 49.62	+49 12 15.67	+02 54 29.83	-04 14 13.58	-22 52 48.43
J (mag) [b]	4.198 ± 0.278	3.711 ± 0.204	3.815 ± 0.01 [e]	3.05 ± 0.23	2.963 ± 0.264
H (mag) [b]	3.829 ± 0.208	3.234 ± 0.212	3.306 ± 0.01 [e]	2.52 ± 0.19	2.633 ± 0.236
K (mag) [b]	3.757 ± 0.298	3.030 ± 0.296	3.188 ± 0.01 [e]	2.44 ± 0.21	2.556 ± 0.230
distance (pc) [c]	157.7 ± 9.2	75.0 ± 1.6	94.4 ± 2.9	62.1 ± 0.8	160 ± 5
μ_α (mas/yr) [a]	-8.39 ± 0.42	6.67 ± 0.27	-43.36 ± 0.29	-0.47 ± 0.23	-30.42 ± 0.17
μ_δ (mas/yr) [a]	-6.63 ± 0.20	41.74 ± 0.19	12.82 ± 0.25	217.36 ± 0.18	11.49 ± 0.16
Mass ($M_\odot$) [d]	$3.04^{+0.30}_{-0.15}$	$2.17^{+0.07}_{-0.19}$	$1.96^{+0.41}_{-0.06}$	$2.09^{+0.08}_{-0.57}$	$4.18^{+0.26}_{-0.22}$
Sp. type	K0 III	K0 IV	G9 III	K0 III	F7/F8II
[Fe/H]	+0.01	-0.10	-0.12	-0.32	+0.01
Age (Gyr)	$0.34^{+0.02}_{-0.03}$	$0.87^{+0.13}_{-0.03}$	$1.31^{+0.02}_{-0.35}$	$0.91^{+0.38}_{-0.04}$	0.14 ± 0.01

aThe refined data reduction of *Hipparcos* (van Leeuwen , 2007)
b2MASS Catalog(Cutri et al., 2003)
cThe parallax-based distance from *Hipparcos* uses van Leeuwen (2007)
dTakeda et al. (2008)
e Laney et al. (2012)

Table 3.7: Stellar property of targets observed in WIYN/NESSI II

Property	HD 74395	HD 95808	HD 106714	HD 157527	HD 159353
R.A. (J2000)[a]	08 43 40.37	11 03 14.87	12 16 20.53	17 24 42.02	17 33 39.38
Dec. (J2000) [a]	-07 14 01.43	-11 18 12.49	+23 56 43.47	-21 26 29.31	+16 19 03.18
J (mag) [b]	3.194 ± 0.278	4.091 ± 0.334	3.380 ± 0.246	4.349 ± 0.324	4.127 ± 0.274
H (mag) [b]	2.786 ± 0.262	3.526 ± 0.252	2.911 ± 0.186	3.798 ± 0.246	3.648 ± 0.244
K (mag) [b]	2.71 ± 0.3	3.431 ± 0.296	2.697 ± 0.276	3.810 ± 0.288	3.373 ± 0.314
distance (pc) [c]	235 ± 15	103.8 ± 7.4	76.4 ± 0.3	92.5 ± 4.0	92.9 ± 3.6
μ_α (mas/yr) [a]	-11.62 ± 0.21	-81.61 ± 0.67	-26.55 ± 0.29	-16.77 ± 0.64	-5.40 ± 0.32
μ_δ (mas/yr) [a]	-1.36 ± 0.13	-108.01 ± 0.59	-6.22 ± 0.17	-26.24 ± 0.35	-63.92 ± 0.37
Mass ($M_\odot$) [d]	$4.44^{+0.36}_{-0.34}$	$2.58^{+0.12}_{-0.20}$	$2.50^{+0.10}_{-0.24}$	2.49 ± 0.09	$2.69^{+0.09}_{-0.15}$
Sp. type	G2Ib	G7III	K0III	K0 III	K0III
[Fe/H]	-0.07	-0.09	-0.18	+0.07	+0.00
Age (Gyr)	0.12 ± 0.01	$0.54^{+0.07}_{-0.03}$	$0.61^{+0.09}_{-0.04}$	0.58 ± 0.02	$0.48^{+0.03}_{-0.01}$

aThe refined data reduction of *Hipparcos* (van Leeuwen , 2007)
b2MASS Catalog(Cutri et al., 2003)
cThe parallax-based distance from *Hipparcos* uses van Leeuwen (2007)
dTakeda et al. (2008)

Table 3.8: Stellar property of targets observed in WIYN/NESSI III

Property	HD 162076	HD 167042
other name		
R.A. (J2000)[a]	17 48 24.76	18 10 31.64
Dec. (J2000) [a]	+20 33 55.57	+54 17 11.59
J (mag) [b]	4.148 ± 0.236	3.933 ± 0.230
H (mag) [b]	3.717 ± 0.224	3.557 ± 0.198
K (mag) [b]	3.544 ± 0.332	3.550 ± 0.238
distance (pc) [c]	79.4 ± 2.6	50.22 ± 0.65
μ_α (mas/yr) [a]	24.28 ± 0.40	107.94 ± 0.29
μ_δ (mas/yr) [a]	4.72 ± 0.30	247.35 ± 0.27
Mass ($M_\odot$) [d]	$2.27^{+0.06}_{-0.05}$	1.50 ± 0.18
Sp. type	G5 IV	K1 III
[Fe/H]	+0.04	+0.00
Age (Gyr)	0.77 ± 0.02	$2.81^{+0.56}_{-0.45}$

aThe refined data reduction of *Hipparcos* (van Leeuwen , 2007)
b2MASS Catalog(Cutri et al., 2003)
cThe parallax-based distance from *Hipparcos* uses van Leeuwen (2007)
dTakeda et al. (2008)

Table 3.9: Summary of known planets

Name	Minimum planetary mass ($M_{\rm Jup}$)	Period (days)	Semi-major axis (AU)	Eccentricity	Periastron separation (AU)	Stellar companion
ι Dra b	12 ± 1.1 [a]	510.72 ± 0.07 [b]	1.27 [b]	0.713 ± 0.008 [b]	0.36	No [c,d]
18 Del b	10.3 [e]	993.3 ± 3.2 [e]	2.6 [e]	0.08 ± 0.01 [e]	2.4	Yes [f]
HD 5608 b	1.4 [g]	792.6 ± 7.7 [g]	1.9 [g]	0.190 ± 0.061 [g]	1.5	Yes [d]
HD 14067 b	7.8 ± 0.7 [h]	$1455\ ^{+13}_{-12}$ [h]	3.4 ± 0.1 [h]	$0.533\ ^{+0.043}_{-0.047}$ [h]	1.6	No [d]
HD 167042	1.7	412.6	1.3	0.027		No [i]

a Baines et al. (2011)
b Kane et al. (2010)
c Kane et al. (2014)
d This work
e Sato et al. (2008)
f Mugrauer et al. (2014)
g Sato et al. (2012)
h Wang et al. (2014)
i Johnson et al. (2008)

3.4.1 Age estimation of some of the systems

There is no information about age estimation of ι Dra so far. Age of the system is crucial information to estimate companion's mass and detection limit via atmosphere model for a low mass object, as we wrote it. Here we determined which age model is appropriate for ι Dra. We plots the PARSEC isochrone model (Bressan et al., 2012) within the range of the uncertainty of ι Dra ' s mass derived by Baines et al. (2011). The position of ι Dra in the figure 3.6 agrees with an age of 2 Gyr. Hence we use the 2 Gyr model to evaluate the detectable mass limits.

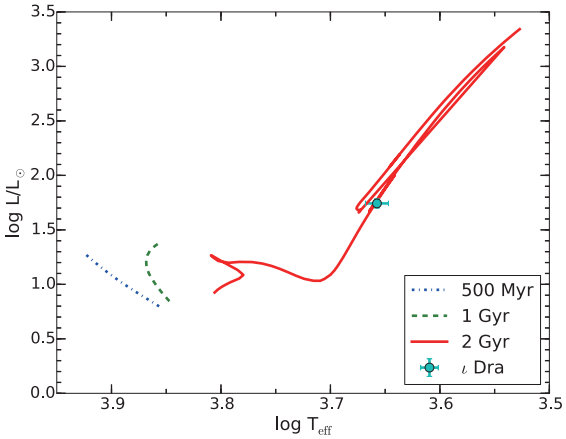

Figure 3.6: PARSEC (Bressan et al., 2012) isochrone plot, effective temperature Teff vs. luminosity. The green dot with error bars is the measured value for ι Dra, which clearly agrees with the 2 Gyr PARSEC isochrone model.

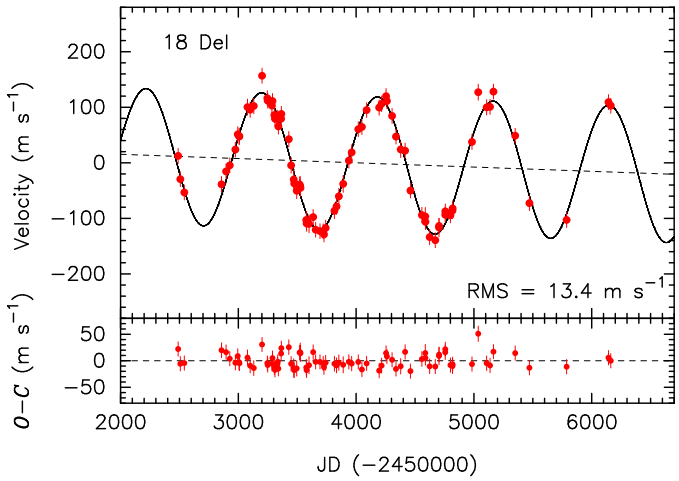

Figure 3.7: RVs of 18 Del observed at OAO. The nearly circular Keplerian orbit with a linear velocity trend ($\dot{v} = -2.8$m s^{-1} yr^{-1}) is shown by the solid line.

3.4.2 RV trends

We selected RV trend samples as > 10 m s^{-1} yr^{-1} shifts in observation periods (~ 10 years). For the case of planet host systems (HD 167042), we fit the RV data and detect RV trends. We fitted RVs to measure linear RV trends except objects whose RV trends have been reported, using the method of least squares; fitting function is $f(x) = ax + b$ and to minimize χ^2,

$$\chi^2 = \sum (\mathrm{RVdata} - f(x)/\mathrm{RVerror})^2 \tag{3.4.1}$$

and RVs are shown in figure 3.7 - 3.22.

RVs of HD 9408, HD 11949, HD64152, HD120420, and HD159353 have curvature feature. We also tried to fit linear RVs in the shape of RVs. For 18 Del, and HD 167042, we fitted with the orbital parameters of already discovered planets with RV trends. For ι Dra, HD 5608, HD 14067, RV trends are derived from Zechmeister et al. (2008), Sato et al. (2012), and Wang et al. (2014).

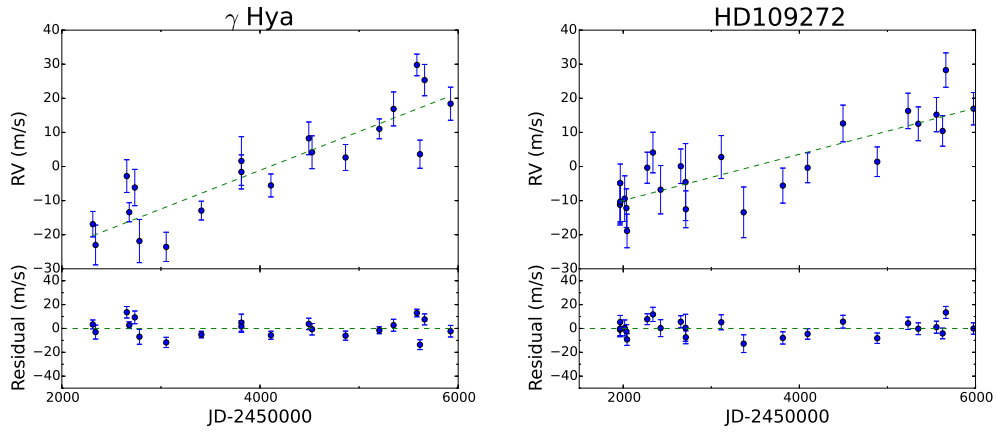

Figure 3.8: Measured RV data of the two systems γ Hya (left) and HD 109272 (right). The dashed lines show the best-fit linear trends.

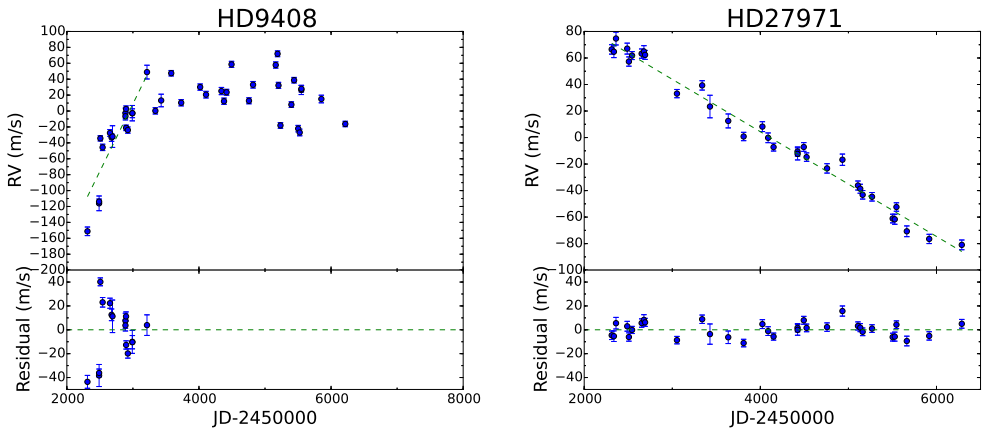

Figure 3.9: Measured RV data of the two systems HD9408 (left) and HD 27971 (right). The dashed lines show the best-fit linear trends.

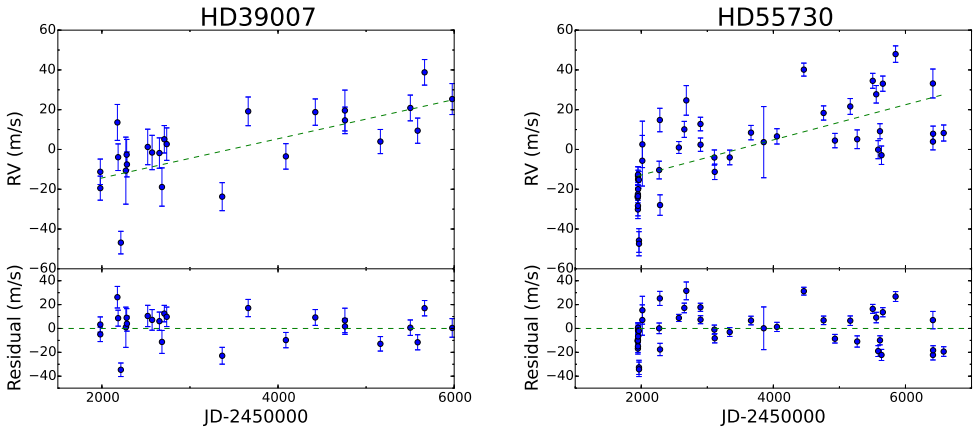

Figure 3.10: Measured RV data of the two systems HD39007 (left) and HD 55730 (right). The dashed lines show the best-fit linear trends.

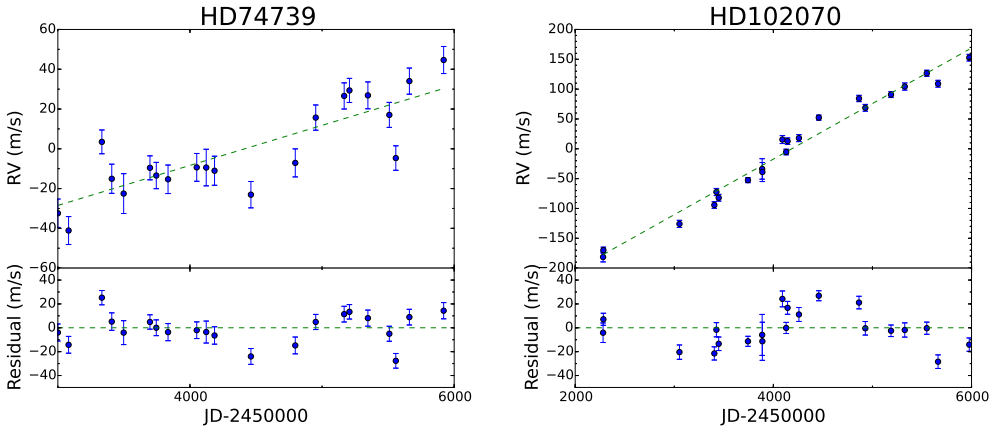

Figure 3.11: Measured RV data of the two systems HD74739 (left) and HD 102070 (right). The dashed lines show the best-fit linear trends.

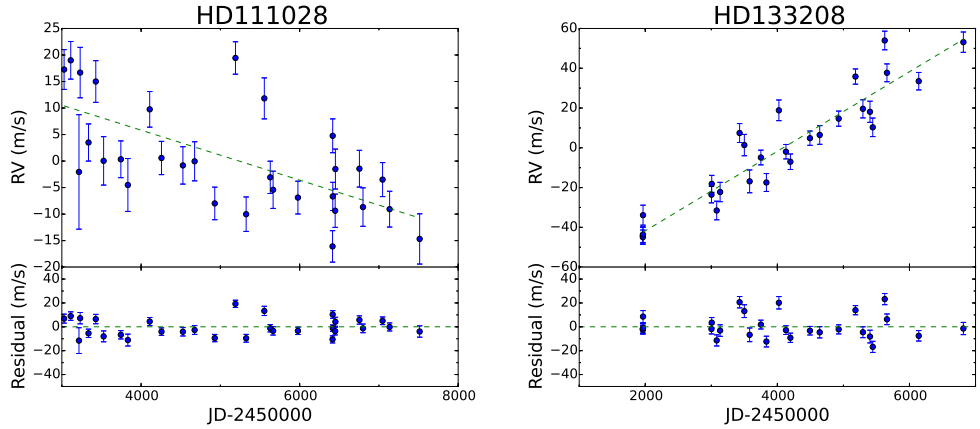

Figure 3.12: Measured RV data of the two systems HD 111028 (left) and HD 133208 (right). The dashed lines show the best-fit linear trends.

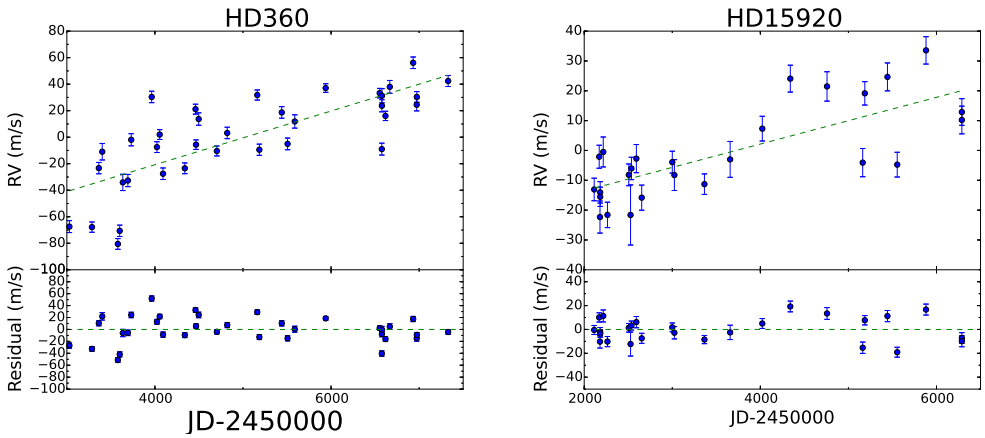

Figure 3.13: Measured RV data of the two systems HD 360 (left) and HD 15920 (right). The dashed lines show the best-fit linear trends.

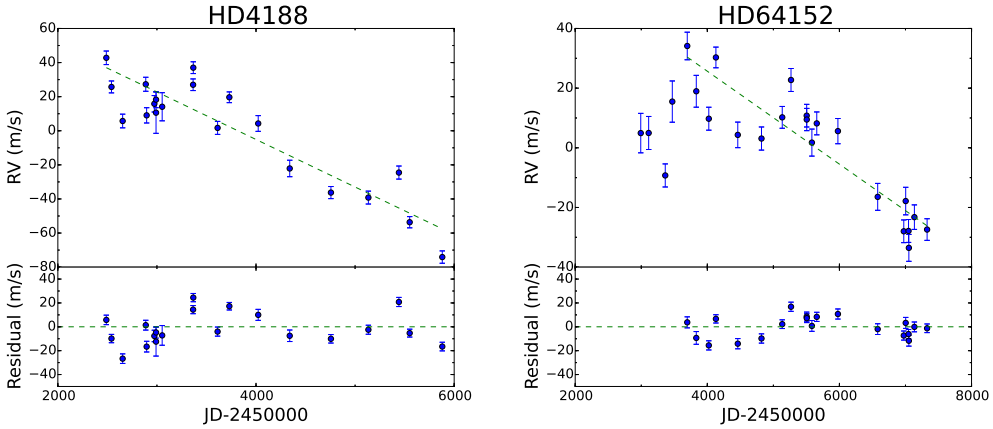

Figure 3.14: Measured RV data of the two systems HD 4188 (left) and HD 64152 (right). The dashed lines show the best-fit linear trends.

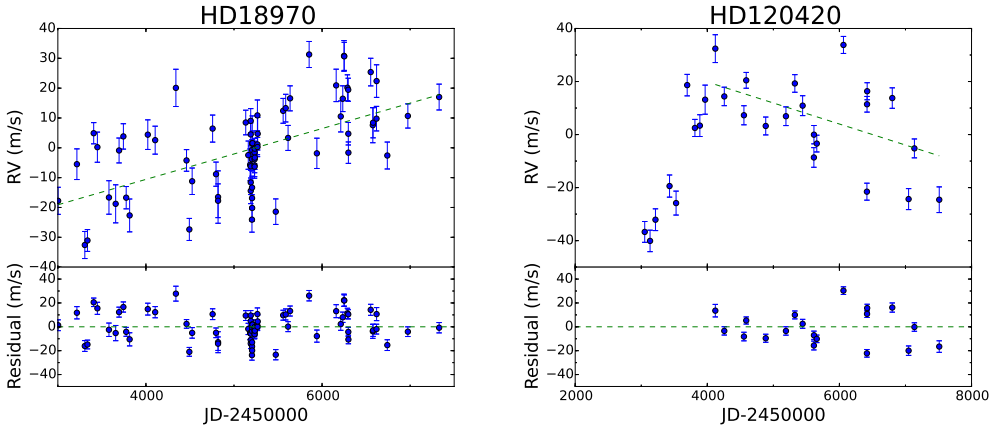

Figure 3.15: Measured RV data of the two systems HD 18970 (left) and HD 120420 (right). The dashed lines show the best-fit linear trends.

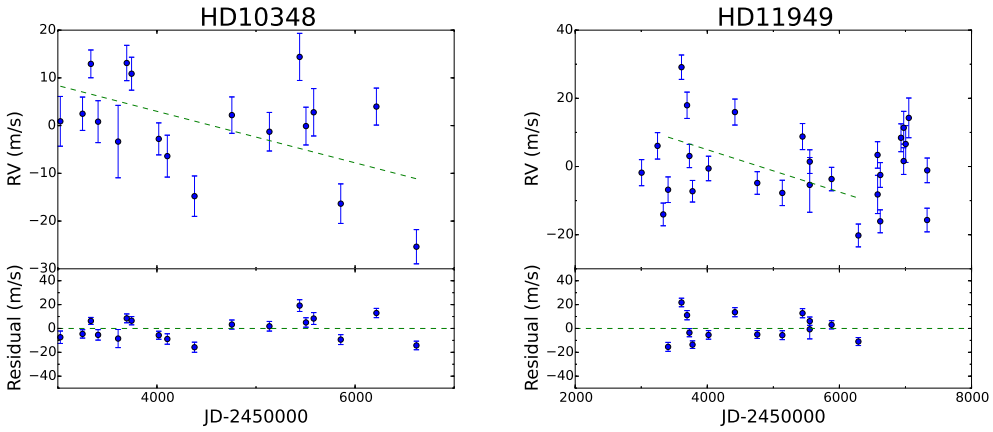

Figure 3.16: Measured RV data of the two systems HD 10348 (left) and HD 11949 (right). The dashed lines show the best-fit linear trends.

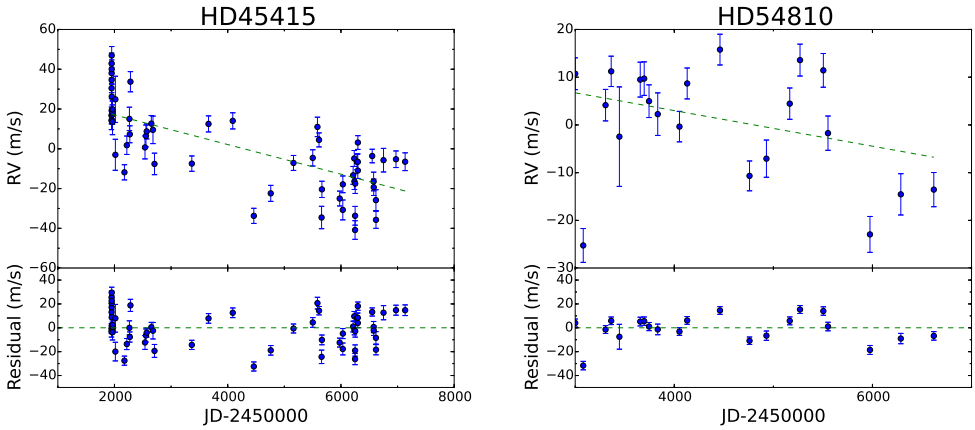

Figure 3.17: Measured RV data of the two systems HD 45415 (left) and HD 54810 (right). The dashed lines show the best-fit linear trends.

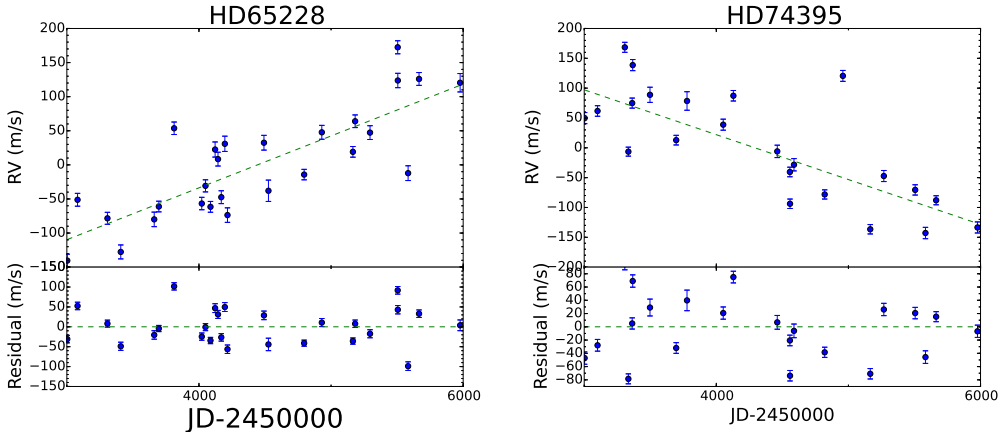

Figure 3.18: Measured RV data of the two systems HD 65228 (left) and HD 74395 (right). The dashed lines show the best-fit linear trends.

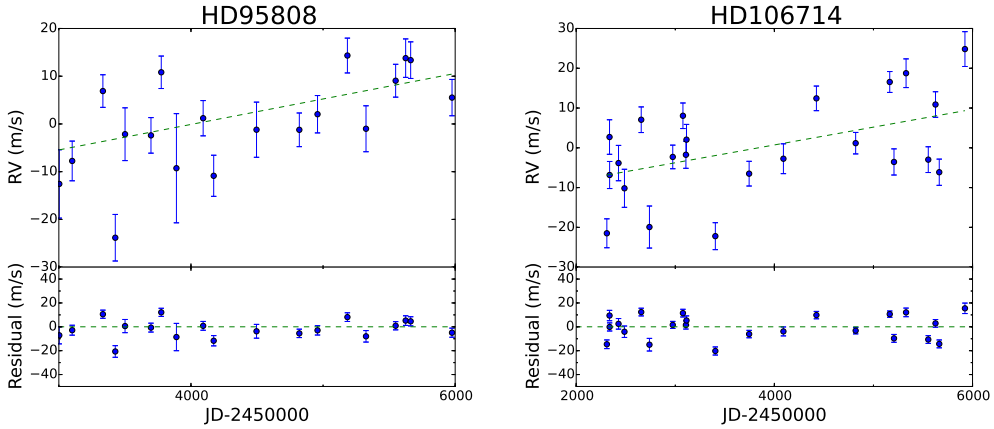

Figure 3.19: Measured RV data of the two systems HD 95808 (left) and HD 106714 (right). The dashed lines show the best-fit linear trends.

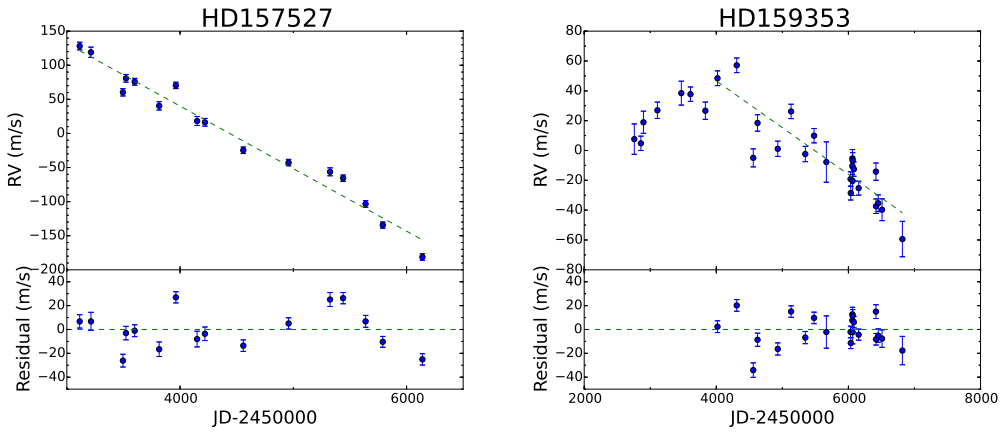

Figure 3.20: Measured RV data of the two systems HD 157527 (left) and HD 159353 (right). The dashed lines show the best-fit linear trends.

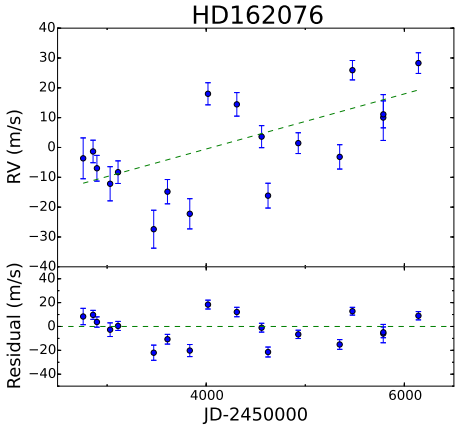

Figure 3.21: Measured RV data of the two systems HD 162076. The dashed lines show the best-fit linear trends.

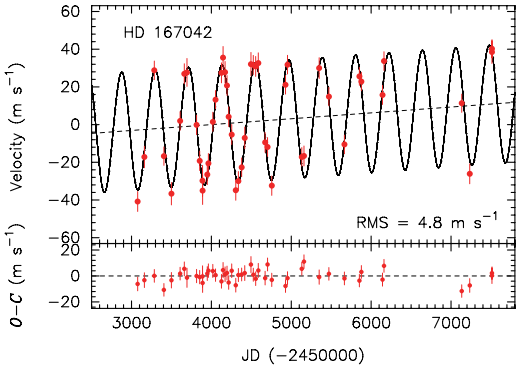

Figure 3.22: RVs of HD167042 observed at OAO. The nearly circular Keplerian orbit with a linear velocity trend ($\dot{v} = \mathbf{1.1\ m\ s^{-1}}$ yr^{-1}) is shown by the solid line.

Table 3.10: RV trends of our targets

Name	$\dot{\gamma}$(m s^{-1} yr^{-1})	
γ Hya	4.1 ± 0.2	This work
ι Dra	−13.65 ± 0.75	Kane et al. (2010)
18 Del	−2.8 ± 0.7	This work
HD 5608	−5.51 ± 0.45	Sato et al. (2012)
HD 14067	−22.4 ± 2.2	Wang et al. (2014)
HD 109272	2.4 ± 0.2	This work

Table 3.11: RV trends of our targets observed in December 2015 and WIYN/NESSI

Name	$\dot{\gamma}(\mathrm{m\,s^{-1}\,yr^{-1}})$
HD 27971	-14.43 ± 0.19
HD 39007	3.60 ± 0.37
HD 55730	3.22 ± 0.14
HD 74739	7.35 ± 0.59
HD 102070	34.00 ± 0.45
HD 111028	-1.72 ± 0.17
HD 133208	7.30 ± 0.23
HD 360	7.39 ± 0.30
HD 15920	2.86 ± 0.21
HD 4188	-10.18 ± 0.29
HD 18970	3.11 ± 0.19
HD 10348	-1.97 ± 0.30
HD 45415	-2.72 ± 0.11
HD 54810	-1.36 ± 0.27
HD 65228	27.78 ± 0.83
HD 74395	-27.47 ± 0.74
HD 95808	1.94 ± 0.37
HD 106714	1.63 ± 0.21
HD 157527	-33.48 ± 0.49
HD 162076	3.37 ± 0.33
HD 9408	61.8±1.9
HD 64152	-5.68±0.28
HD 120420	-2.89±0.32
HD 11949	-2.26±0.37
HD 159353	-11.45±0.56

3.5 Direct Imaging Observations

The observation log is summarized in Table 3.12 and Table 3.13. In 2015 winter observations, if a companion candidate was seen in quick look image, we obtained J, H, Ks, three colors of the images. Data reduction was conducted as noted above by me.

Observations at WIYN telescope were done in December 2016 to April 2017 in queue mode observation. Each observation exposure time is 40 ms exposures in 832nm central wavelength, 40nm wide filter. The background 5 σ sensitivity is measured in the reconstructed speckle image using a series of concentric annuli around the target star. If a companion candidate was detected, its relative photometry & astrometry is measured based on model fits to the power spectrum from the autocorrelation functions for each frame in the image set. Reconstructed images, 5 σ sensitivity, and detected companion candidate photometry are provided from NESSI team.

Table 3.12: Summary of observation log in SEEDS

Target	Obs. date (UT)	Band	Total ET (s)	Rotation angle	Mask (″)	Notes
γ Hya	2012 May 13	H	585	10.3	0.6	
	2014 Apr. 25	J	150	3.0		cloudy
	2014 Apr. 25	H	148.5	2.8		cloudy
	2014 Apr. 25	Ks	75	2.4		cloudy
ι Dra	2012 May 14	H	675	12.0	0.6	cloudy
18 Del	2011 Aug. 2	H	585	27.7	0.4	
	2012 Jul. 8	H	480	20.7	0.4	
	2014 Jun. 10	H	575	31.7		
HD 5608	2011 Dec. 31	H	570	30.8	0.4	
	2012 Sep. 12	H	966	28.1	0.6	
	2014 Oct. 7	H	600	31.5		cloudy
HD 14067	2012 Nov. 5	H	1600	89.3	0.4	
HD 109272	2012 Apr. 11	H	450	10.8	0.4	
	2014 Apr. 23	J	195	4.8		
	2014 Apr. 23	H	147	3.6		
	2014 Apr. 23	Ks	165	1.0		

Table 3.13: Summary of observation log in December 2015

Target	Obs. date (UT)	Band	Total ET (s)	Rotation angle	Mask (″)	Notes
HD 9408	2015 Dec. 30	H	418.5	7.9		
HD 27971	2015 Dec. 29	J	15	0.2		
	2015 Dec. 29	H	15	0.3		
	2015 Dec. 29	Ks	15	0.3		
HD 39007	2015 Dec. 29	J	15	0.3		
	2015 Dec. 29	H	15	0.5		
	2015 Dec. 29	Ks	15	0.5		
HD 55730	2015 Dec. 30	J	180	0.3		
	2015 Dec. 30	H	180	0.1		
	2015 Dec. 30	Ks	180	0.1		
ι Cnc A	2015 Dec. 29	J	15	0.1		
	2015 Dec. 29	H	15	0.1		
	2015 Dec. 29	Ks	15	0.1		
ζ Crt	2015 Dec. 30	J	150	3.6		
	2015 Dec. 30	H	150	3.6		
	2015 Dec. 30	Ks	150	3.6		
HD 111028	2015 Dec. 30	J	120	7.9		
	2015 Dec. 30	H	150	7.7		
	2015 Dec. 30	Ks	150	12.2		
β Boo	2016 Jan. 4	J	300	3.8		
	2016 Jan. 4	H	300	3.1		
	2016 Jan. 4	Ks	375	4.4		
HD 360	2015 Dec. 29	H	420	5.5		
HD 15920	2015 Dec. 29	H	405	8.2		
HD 4188	2015 Dec. 30	180	H	2.1		
HD 64152	2015 Dec. 30	H	510	11.0		
HD 18970	2015 Dec. 30	H	570	10.7		
HD 120420	2016 Jan. 4	H	600	6.0		

Chapter 4

Results

We detected five companion candidates in the four systems γ Hya, 18 Del, HD 5608, and HD 109272. Follow-up observations confirmed that three of the companion candidates in three systems, γ Hya, HD 5608, and HD 109272, have a common proper motion. We converted the observed flux of the companion to its mass using the NextGen model (Hauschildt et al., 1999a,b) or the Dusty model (Chabrier et al., 2000). The model that was most consistent with regard to the derived mass for all three bands (J-, H-, Ks-band) was adopted. The targets' ages, excepting ι Dra, were estimated in Takeda et al. (2008) by comparing the luminosities and effective temperatures with the theoretical stellar evolution model (Lejeune and Schaerer, 2001). We roughly estimated the age of ι Dra by comparing its luminosity and effective temperature with a theoretical model (Bressan et al., 2012; Chen et al., 2015)

4.1 Confirmed Stellar Companions

4.1.1 γ Hya

We discovered a companion candidate with an H-band contrast of ΔH = 7.24 located 1.6″ from γ Hya, as shown in Figure 4.1. Two years after the first observation, a follow-up observation enabled us to confirm that the companion candidate, γ Hya B, shares a common proper motion with the central star (Figure 4.2). Our astrometric and photometric results are shown in Table 4.1. Considering γ Hya's age (0.37 Gyr, Takeda et al. 2008) and consistency of the mass derived from J-, H-, and Ks-band photometry, we adopted the 400-Myr NextGen model to convert the measured photometry into mass. Mass of γ Hya B is $0.61^{+0.12}_{-0.14}$ $M_{\odot}$ by averaging mass estimates from four independent obsrvation results.

4.1.2 HD 109272

We discovered one companion candidate (ΔH = 7.18) at a separation of 1.2″ from HD 109272 (Figure 4.1). Follow-up observations allowed a common proper motion test for the candidate (Figure 4.2), which suggested that the companion candidate HD 109272 B is gravitationally bound to the central star. Table 4.2 shows the astrometric and photometric results for HD 109272 B. Its mass was calculated using the 1-Gyr Dusty model based on an age of HD 109272 B of 1.4 Gyr (Takeda et al., 2008). By averaging two mass estimates derived from two observations, we find that HD 109272 B has a mass of $0.28 \pm 0.06 M_{\odot}$.

4.1.3 HD 5608

We found two companion candidates around HD 5608. The first candidate has ΔH = 9.40 with a separation of 0.6″ and the second has ΔH = 13.1 with a separation of

Table 4.1: Astrometric and photometric results for γ Hya B

Name	Date (UT)	Filter	Sep. (″)	P.A. (deg)	Δmag	Mass ($M_{\odot}$)
γ Hya B	2012 May 13	H	1.623 ± 0.011	194.4 ± 0.2	7.24 ± 0.08	0.63 ± 0.06
	2014 Apr. 25	J	1.611 ± 0.004	195.2 ± 0.2	7.97 ± 0.24	0.53 ± 0.14
	2014 Apr. 25	H	1.611 ± 0.004	195.2 ± 0.2	7.39 ± 0.20	0.61 ± 0.12
	2014 Apr. 25	Ks	1.626 ± 0.006	195.3 ± 0.1	7.07 ± 0.30	0.65 ± 0.21

Table 4.2: Astrometric and photometric results for HD 109272 B

Name	Date (UT)	Filter	Sep. (″)	P.A. (deg)	Δmag	Mass ($M_\odot$)
HD 109272 B	2012 Apr. 11	H	1.187 ± 0.005	53.0 ± 0.2	7.18 ± 0.14	0.30 ± 0.04
	2014 Apr. 23	J	1.168 ± 0.004	52.0 ± 0.1	7.36 ± 0.33	0.28 ± 0.06
	2014 Apr. 23	H	1.166 ± 0.004	52.2 ± 0.1	7.22 ± 0.28	0.30 ± 0.09
	2014 Apr. 23	Ks	1.170 ± 0.006	52.0 ± 0.1	7.40 ± 0.16	0.24 ± 0.04

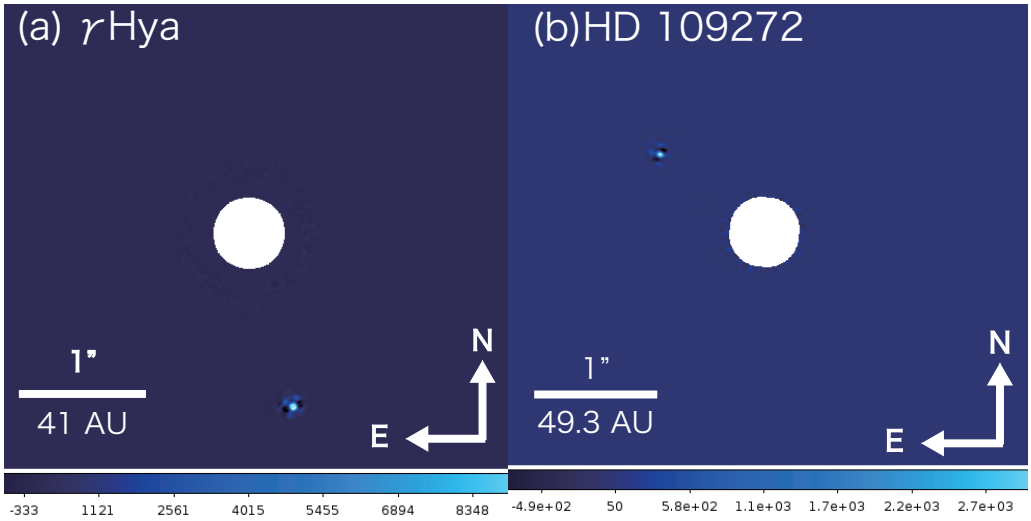

Figure 4.1: Detected bright companions from HiCIAO observations. (a) Final image of γ Hya in the H-band taken on 2012 May 13. North is up and east is left. The companion was detected at 1.6″ from γ Hya. (b) Final image of HD 109272 in the H-band taken on 2012 April 11. The companion candidate at 1.2″ can be seen in the figure.

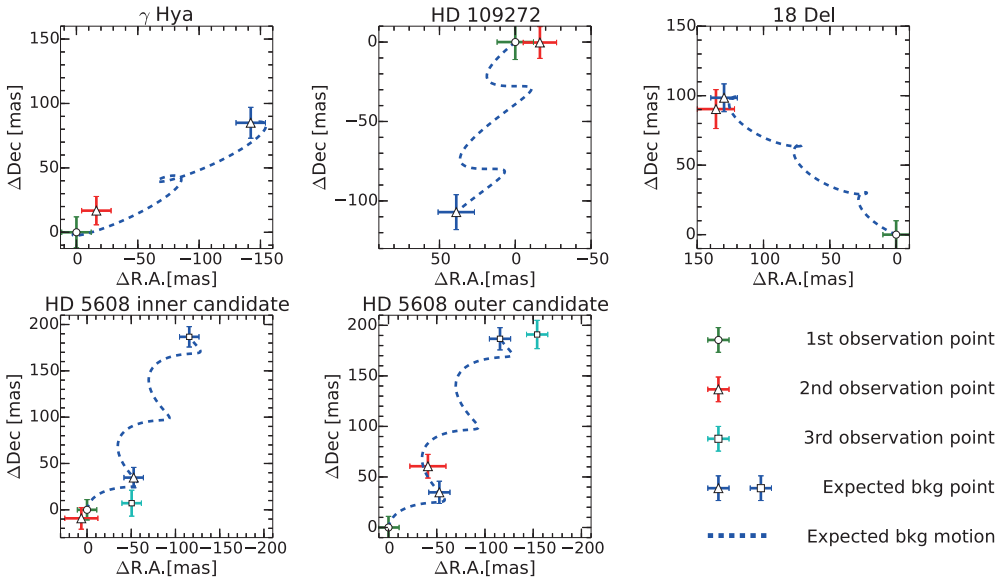

Figure 4.2: Results of the common proper motion test for the companion candidates. The horizontal and vertical axes are relative distances from the first observation point. In each plot the circle with a green cross is the first observed position with error, the triangle with a red cross represents the second observed position, and the square with a cyan cross represents the third observed position. The blue dotted line represents the track of background star motion driven by the stellar parallax and the proper motion of each star. The blue crosses shows the positions of the observational data if the companion candidate is a background star.

Table 4.3: Astrometric and photometric results for HD 5608 B

Name	Date (UT)	Filter	Sep. (″)	P.A. (deg)	Δmag	Mass ($M_\odot$)
HD 5608 B	2011 Dec. 31	H	0.627 ± 0.009	58.9 ± 0.4	9.40 ± 0.11	0.11 ± 0.02
	2012 Sep. 12	H	0.627 ± 0.022	59.9 ± 1.0	9.70 ± 0.10	0.10 ± 0.02
	2014 Oct. 7	H	0.588 ± 0.012	55.7 ± 0.6	9.55 ± 0.20	0.11 ± 0.02

7.4″, as shown in Figure 4.3. The time intervals of our three observations are long enough to allow for common proper motion tests (Figure 4.2). We conclude that the close companion candidate HD 5608 B is co-moving and the other companion candidate at 7.4″ is a background star. Our astrometric and photometric results for HD 5608 B are shown in Table 4.3. Considering that HD 5608 B has an age of 2.5 Gyr (Takeda et al., 2008) , we used the interpolation between the 2-Gyr and 3-Gyr Dusty models to estimate the mass of HD 5608 B. The mass derived from Dusty is $0.106 \pm 0.002 M_\odot$ from the weighted mean of three observational results, and that derived from NextGen model is $0.13 \pm 0.01 \sim M_\odot$. These indicate that HD 5608 B is a low mass star, and the Dusty model is a model to reproduce the luminosity of the low-mass stars . Thus, we adopted the interpolation between the 2-Gyr and 3-Gyr Dusty models, and took the mass of HD 5608 B to be $0.10 \pm 0.01 M_\odot$.

4.2 Confirmed Background Star

4.2.1 18 Del

We found a faint companion candidate of ΔH = 16.9 with S/N ∼ 5 at 7.5″ from 18 Del A (Figure 4.3). In the July 2012 observation, we were not able to detect the candidate because the exposure time was not enough to detect the candidate. We detected it again on 2014 June 10th and we carried out a common proper motion test. The result indicates that the companion candidate traces the track expected for a background star (Figure 4.2). The achieved contrast ratio is shown in Figure 4.4. The detectable mass limits derived from the COND 0.8-Gyr model (Baraffe et al., 2003) for an age of 18 Del of 0.79 Gyr (Takeda et al., 2008) is displayed in the right panel of Figure 4.4. We exclude a $\sim 0.13\ M_\odot$ object at 0.5″, a $\sim 0.05\ M_\odot$ object at 1.0″, and a $\sim 0.03\ M_\odot \approx 31\ M_{\rm Jup}$ object beyond 2.0″ from the central star.

4.3 Case of the non-detection of the companion candidates from HiCIAO observations

4.3.1 ι Dra

We were not able to detect any objects on 2012 May 14 in the H-band for ι Dra beyond 0.6″. Figure 3.6 plots the PARSEC isochrone (Bressan et al., 2012) model within the range of the uncertainty of ι Dra's mass derived by Baines et al. (2011). The position of ι Dra in the figure agrees with an age of 2 Gyr. Hence we use the 2-Gyr COND model (Baraffe et al., 1998) to evaluate the detectable mass limits. Although the age estimation for iot Dra may not be accurate, we note that there is not a big difference in the results even if the difference in the adopted age is ± 1 Gyr. The excluded object mass range is

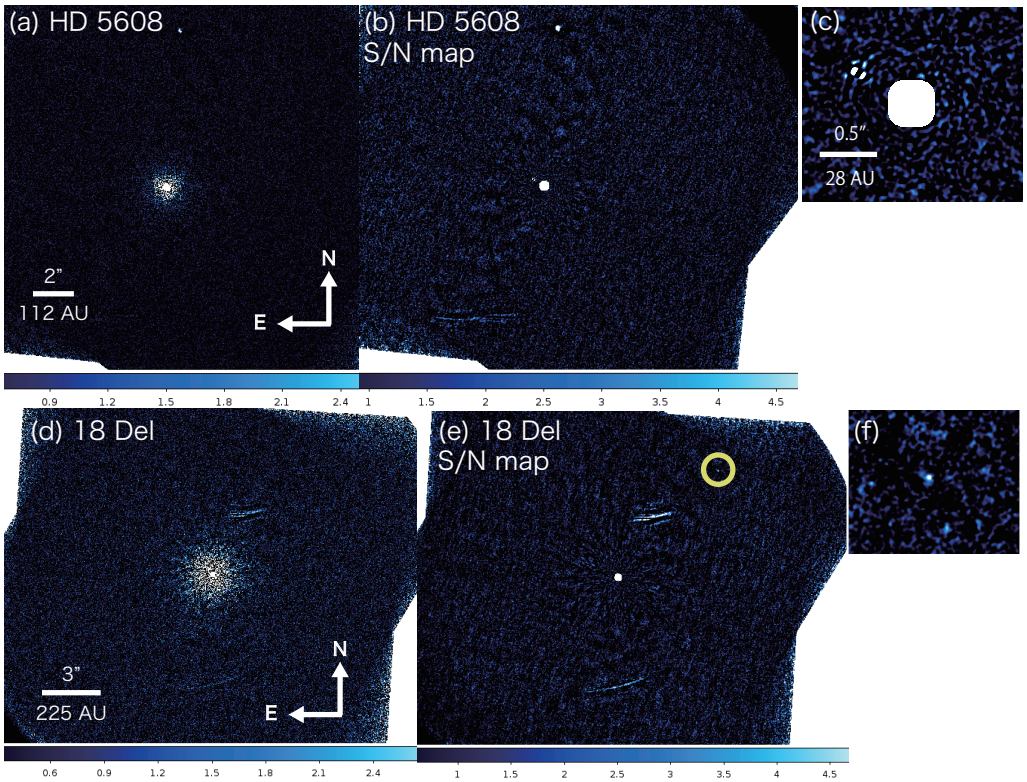

Figure 4.3: Images of faint companion and background stars detected by HiCIAO observations for HD 5608 and 18 Del. S/N map for each target is also shown to help to see a faint companion candidate, which is difficult to see on the panel (a) or (d). (a) Final image of HD 5608 in the H-band taken on 2011 December 31. (b) S/N map of HD 5608 at H-band showing faint companion candidates. Two companion candidates can be distinguished from the noise. A close faint companion candidate can be seen 0.6 from the central star. A distant companion candidate is detected 7.4 from the central star. (c) Closed-up S/N map showing the inner candidate of HD 5608. (d) Final image of 18 Del in the H-band taken on 2011 August 2. (e) S/N map of 18 Del at H-band showing a faint companion candidate.

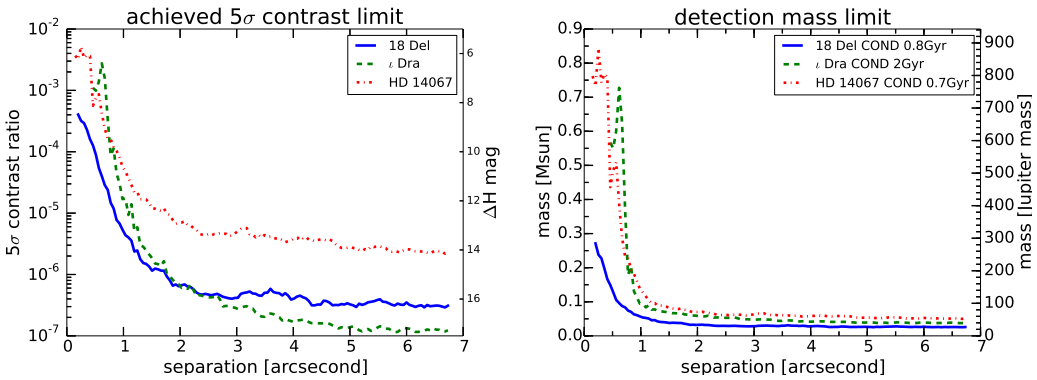

Figure 4.4: Left: Achieved 5σ contrast ratio on 2011 Aug. 2 for 18 Del in the H-band, 2012 May 14 for ι Dra in the H-band, and 1012 Nov. 5 for HD 14067 in the H-band. Right: Detectable mass limits for 18 Del, ι Dra, and HD 14067.

shown in Figure 4.4. We exclude a $\sim 0.09\ M_{\odot}$ object at $1.0''$ and a $\sim 0.05\ M_{\odot} \approx 52\ M_{\rm Jup}$ object over $2''$.

4.3.2 HD 14067

We were not able to find any companion candidates around HD 14067. Figure 4.4 shows the 5σ detectable mass limit, converted using the COND 0.7-Gyr model for the age of HD 14067 (Wang et al., 2014). No objects with $\sim 0.12\ M_{\odot}$ at $1.0''$ and $\sim 0.06\ M_{\odot}$ beyond $2.0''$ are apparent in the observation.

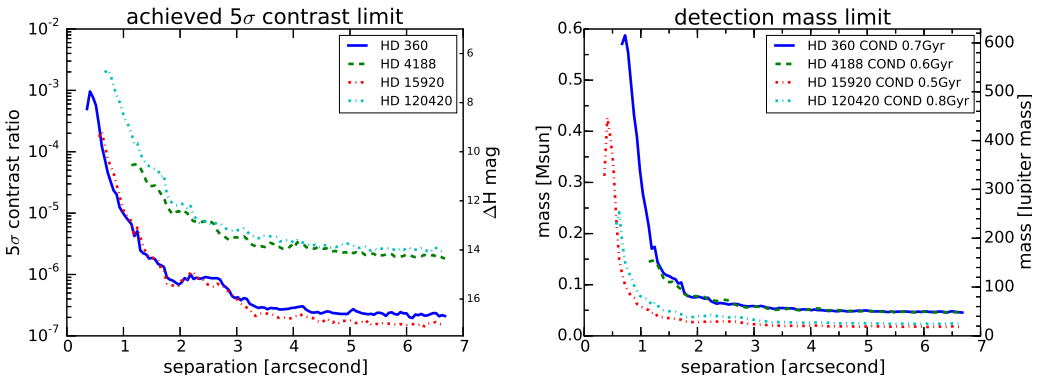

Figure 4.5: Left: Achieved 5σ contrast ratio for HD 360 in the H-band, for HD 4188 in the H-band, for HD 15920 in the H-band, and for HD 120420 in the H-band. Right: Detectable mass limits for HD 360, HD 4188, HD 15920, and HD 120420

4.3.3 HD 360

We were not able to find any companion candidates around HD 360. Figure 4.5 shows achieved 5 σ contrast limit and detectable mass limit converted by COND model of 0.7Gyr model. Detectable mass is 0.58 $M_\odot$ at 0.7 $''$, 0.27 $M_\odot$ at 1.0$''$, and 0.07 $M_\odot$ beyond 2.0 $''$ from HD 360.

4.3.4 HD 4188

We were not able to detect any companion candidates around HD 4188. We calculated 5 σ contrast and detectable mass as shown in Figure 4.5, using COND 0.6 Gyr model. A $\sim$ 0.14 $M_\odot$ object at 1.1$''$ and a $\sim$ 0.07 $M_\odot$ object beyond 2.0$''$ from the HD 4188 were excluded by the HiCIAO observation.

4.3.5 HD 15920

The observation result is no detection around HD 15920. Achieved 5 σ contrast and detectable mass calculated using COND 0.5 Gyr are shown in figure 4.5. We excluded $\sim$ 0.33 $M_\odot$ at 0.5$''$, $\sim$ 0.05 $M_\odot$ at 1.0$''$, and $\sim$ 0.02 $M_\odot$ beyond 2.0$''$ from HD 15920.

4.3.6 HD 120420

No companion candidates around HD 120420 was detected in the observation. Figure 4.5 shows achieved 5 σ contrast limit and detectable mass calculated using COND 0.8 Gyr model in the observation. We excluded $\sim$ 0.24 $M_\odot$ at 0.6$''$, and $\sim$ 0.07 $M_\odot$ at 1.0$''$, and $\sim$ 0.03 $M_\odot$ beyond 2.0$''$ from HD 120420.

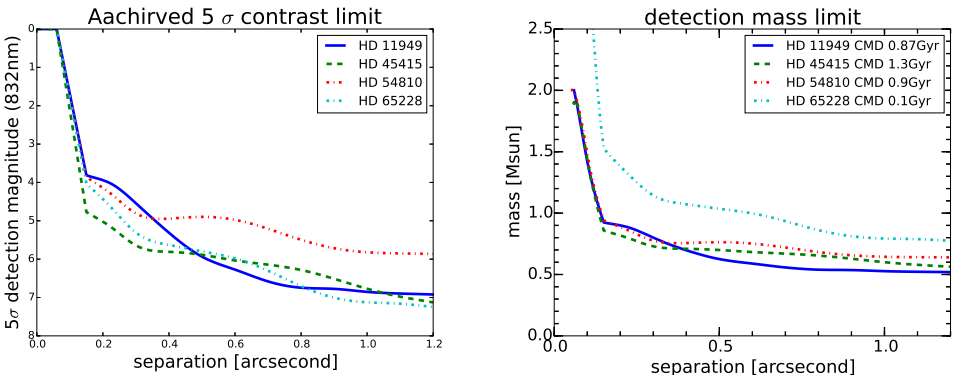

Figure 4.6: Left: Achieved 5σ detection Δ magnitude of HD 11949, HD 45415, HD 54810,and HD 65228 observed by NESSI/WIYN in 832nm. Right: Detectable mass limit for HD 11949, HD 45415, HD 54810,and HD 65228

4.4 Case of the non-detection of the companion candidates from NESSI observations

4.4.1 HD 11949

We were not able to find any companion candidates around HD 11949. Figure 4.6 shows 5 σ detection limit in magnitude. Using PARSEC isochrone model of HD 11949 ages, we converted detection limits to detectable mass. We excluded a $\sim 0.62\ M_{\odot}$ object at $0.5''$, and $\sim 0.52\ M_{\odot}$ object at $1.0''$ from the central star.

4.4.2 HD 45415

No companion candidates around HD 45415 was detected in the observation. Figure 4.6 shows 5 σ detection limit in magnitude and detectable mass. A $\sim 0.70\ M_{\odot}$ object at $0.5''$ and a $\sim 0.60\ M_{\odot}$ at $1.0''$ from HD 45415 are detection limit calculated using PARSEC isochrone of HD 45415 ages.

4.4.3 HD 54810

We could not detect any companion candidates around HD 54810. Figure 4.6 shows 5 σ detection limit in magnitude and detectable mass. We excluded $\sim 0.76\ M_{\odot}$ at $0.5''$, and $\sim 0.64\ M_{\odot}$ at $1.0\ ''$ from HD 54810 using PARSEC isochrone model of HD 54810 age.

4.4.4 HD 65228

We were not able to discover any companion candidates around HD 65228. Figure 4.6 shows 5 σ detection limit in magnitude. Detection limit mass calculated using PARSEC isochrone of HD 65228 ages is $\sim 1.03\ M_{\odot}$ at $0.5''$, and $\sim 0.79\ M_{\odot}$ at $1.0''$ from HD 65228.

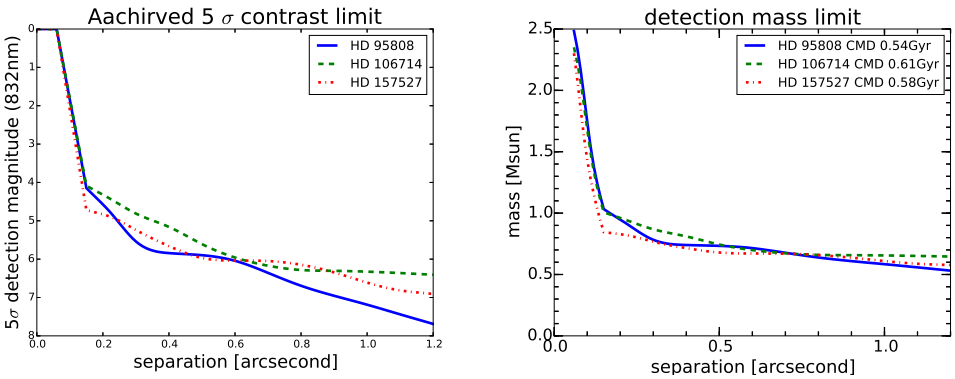

Figure 4.7: Left: Achieved 5σ detection Δ magnitude of HD 95808, HD 106715 and HD 157527 observed by NESSI/WIYN. Right: detectable mass limits derived from detection limit.

4.4.5 HD 95808

We were not able to find any companion candidates around HD 95808. Figure 4.7 shows 5 σ detection limit in magnitude. Detectable mass calculated using PARSEC isochrone of HD 95808 ages is $\sim 0.73\ M_{\odot}$ at $0.5''$, and $\sim 0.58\ M_{\odot}$ at $1.0''$ from the central star.

4.4.6 HD 106714

No companion candidates around HD 106714 was detected. Figure 4.7 shows 5 σ detection limit in magnitude. We derived detection mass limit using PARSEC isochrone of HD 106714 ages. A object with $\sim 0.74\ M_{\odot}$ at $0.5''$ and a object with $\sim 0.65\ M_{\odot}$ at $1.0''$

4.4.7 HD 157527

We could not detect any companion candidates around HD 157527. Figure 4.7 shows 5 σ detection limit in magnitude and detection limit mass derived from PARSEC isochrone of HD 157527 ages. We exclude $\sim 0.67\ M_{\odot}$ at $0.5''$ and $\sim 0.60\ M_{\odot}$ at $1.0''$ from the central star.

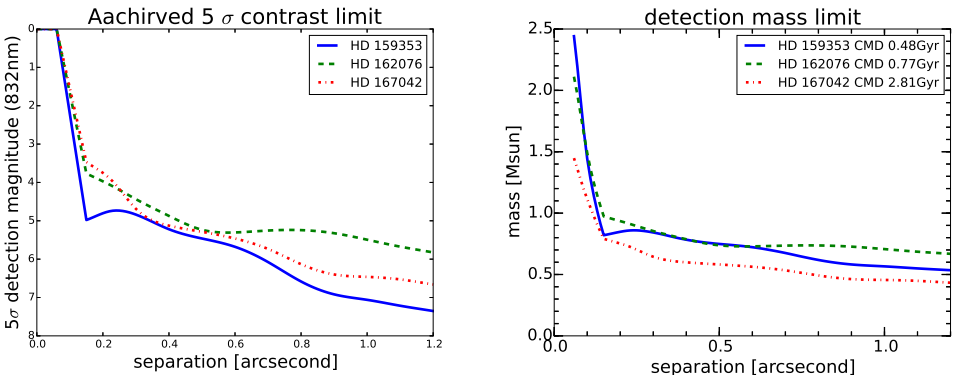

Figure 4.8: Left: Achieved 5σ detection Δ magnitude of HD 159353, HD 162076, and HD 167042 observed by NESSI/WIYN. Right: Detectable mass limit of NESSI observations.

4.4.8 HD 159353

We were not able to find any companion candidates around HD 159353. Figure 4.8 shows 5 σ detection limit in magnitude. Using PARSEC isochrone, we exclude $\sim 0.74\ M_{\odot}$ at $0.5''$ and $\sim 0.56\ M_{\odot}$ at $1.0''$ from the central star.

4.4.9 HD 162076

No companion candidates around HD 162076 was detected. Figure 4.8 shows 5 σ detection limit in magnitude and detection limit mass derived using PARSEC isochrone. A $\sim 0.73\ M_{\odot}$ object at $0.5''$ and a $\sim 0.70\ M_{\odot}$ at $1.0''$ from HD 162076 are detection limits.

4.4.10 HD 167042

Any companion candidates around HD 167042 was not detected. Figure 4.8 shows 5 σ detection limit in magnitude and detection limit mass. We exclude $\sim 0.58\ M_{\odot}$ at $0.5''$ and $\sim 0.45\ M_{\odot}$ at $1.0''$ from HD 167042.

Table 4.4: Astrometric and photometric results of companion candidates detected by HiCIAO

Name	Date	Filter	Sep. ($''$)	P.A. (deg)	Δmag	Absolute mag.	Mass ($M_\odot$)
HD 9408 B	2015 Dec. 30	H	5.699±0.005	14.35±0.04	9.87±0.12	8.33±0.31	0.18±0.02
HD 9408 C		H	7.441±0.009	200.86±0.07	14.35±0.12	12.81±0.31	0.059±0.001
HD 9408 D		H	9.186±0.009	200.96±0.06	15.05±0.12	13.51±0.31	0.055±0.001
HD 18970 B	2015 Dec. 30	H	1.498±0.007	154.47±0.29	14.15±0.34	12.66±0.39	0.050±0.002
HD 18970 C		H	5.998±0.008	190.62±0.07	14.76±0.34	13.27±0.39	0.047±0.002
HD 18970 D		H	9.101±0.008	127.26±0.04	11.49±0.34	10.00±0.39	0.095±0.010
HD 27971 B	2015 Dec. 30	J	0.654±0.004	274.83±0.28	6.62±0.06	5.96±0.30	0.61±0.04
		H	0.667±0.005	274.54±0.50	6.25±0.05	5.17±0.26	0.63±0.04
		Ks	0.676±0.007	274.08±0.87	6.53±0.03	5.28±0.36	0.59±0.06
HD 39007 B	2015 Dec. 29	J	1.117±0.001	264.04±0.19	3.42±0.13	2.50±0.21	$1.43^{+0.09}_{-0.07}$
		H	1.122±0.001	264.41±0.03	3.55±0.03	2.21±0.16	1.49±0.08
		Ks	1.128±0.001	264.41±0.05	3.57±0.01	2.11±0.16	1.54±0.09
HD 55730 B	2015 Dec. 30	H	1.315±0.012	331.77±0.40	8.75±0.20	7.53±0.30	0.27±0.05
		Ks	1.314±0.013	332.64±0.64	8.94±0.12	7.63±0.24	0.22±0.03
HD 55730 C		H	7.702±0.012	324.38±0.07	11.49±0.20	10.26±0.33	0.08±0.01
		Ks	7.749±0.014	324.19±0.11	11.77±0.07	10.46±0.24	0.07±0.01
HD 64152 B	2015 Dec. 30	H	0.96±0.01	256.9±0.9	14.49±0.76	13.22±0.76	0.050±0.004
HD 64152 C		H	9.97±0.01	9.97±0.08	14.88±0.76	13.61±0.76	0.048±0.004
HD 74739 B	2015 Dec. 29	J	0.764±0.002	337.28±0.15	6.67±0.05	4.01±0.21	0.97±0.06
		H	0.777±0.003	338.06±0.55	6.59±0.08	3.50±0.24	1.00±0.07
		Ks	0.745±0.005	337.48±0.20	6.97±0.04	3.77±0.27	0.91±0.07
HD 102070 B	2015 Dec. 30	H	0.329±0.008	94.3±1.7	4.94±0.21	2.42±0.33	$1.46^{+0.19}_{-0.13}$
		Ks	0.323±0.014	98.2±2.5	4.61±0.15	2.00±0.33	$1.68^{+0.18}_{-0.25}$
HD 111028 B	2015 Dec. 30	J	2.233±0.002	236.43±0.19	7.40±0.40	8.30±0.49	0.24±0.06
		H	2.248±0.004	238.16±0.20	7.18±0.12	7.39±0.26	0.28±0.04
		Ks	2.264±0.010	236.26±0.19	7.57±0.19	7.74±0.32	0.21±0.03
HD 133208 B	2016 Jan. 4	J	0.894±0.008	232.78±0.51	8.84±0.32	6.54±0.32	0.52±0.05
		H	0.902±0.022	233.0±1.6	8.31±0.15	5.54±0.15	0.58±0.02
		Ks	0.892±0.003	233.51±0.23	7.97±0.04	5.11±0.04	0.61±0.01

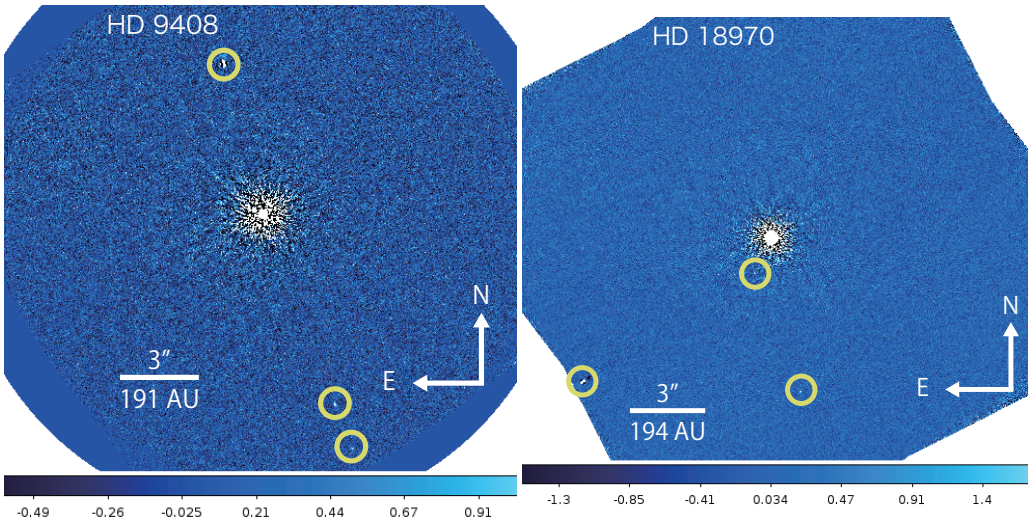

Figure 4.9: Detected companion candidates from HiCIAO observations. (Left) Image of HD 9408 in the H-band taken on 2015 December 30. North is up and east is left. The faint companions were detected at 5.7″, 7.4″, and 9.2″ from HD 9408 as shown in yellow circles. (Right) Final image of HD 18970 in the H-band taken on 2015 December 30. Three faint companion candidates are in yellow circles.

4.5 Stars with Companion Candidates

4.5.1 HD 9408

We discovered three faint companion candidates, HD 9408 B, HD 9408 C, HD 9408 D (ΔH = 9.87, 14.35, 15.05, respectively) located at $\sim$ 5.7″, 7.4″, and 9.2″ from HD 9408 as shown in Figure 4.9. Remembering HD 5608 that suggested a low mass star is suit for Dusty model, we adopted Dusty 1Gyr model to convert flux to mass of the companion candidate. The derived mass is 0.18 $\pm$ 0.02, 0.059 $\pm$ 0.001, and 0.055 $\pm$ 0.001, respectively.

We calculated expected background stars using a Galactic model, the TRILEGAL model (Girardi et al., 2012). The model estimates that the number of expected background star with in the FoV of HiCIAO is nine with a limiting magnitude of H $\sim$ 19.5 that is detection limit of the observation. This suggest that detected companion candidates are likely to be background stars.

4.5.2 HD 18970

We detected three faint companions, HD 18971 B (Δ H = 14.15), HD 18971 C (Δ H = 14.76), and HD 18971 D (Δ H = 11.49) as shown in Figure 4.9. We adopt Dusty 0.6Gyr model to derive mass of companion candidates and estimate that mass of companion candidates, HD 18971 B, HD 18971 C, and HD 18971 D are 0.050 $\pm$ 0.002, 0.047 $\pm$ 0.002, and 0.095 $\pm$ 0.010, respectively.

The number of expected background star calculated by the TRILEGAL model is six with a limiting magnitude of H $\sim$ 19.2. The detected companions may be background stars.

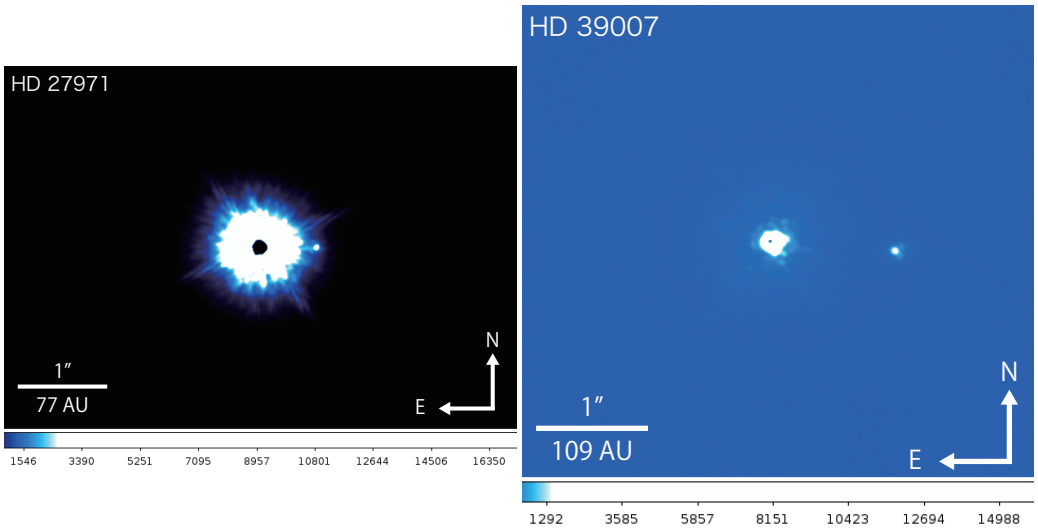

Figure 4.10: Detected companion candidates from HiCIAO observations. (Left) Image of HD 27971 in the H-band taken on 2015 December 29. The companion candidate at 0.6″ can be seen in the figure. (Right) Image of HD 39007 taken in the H-band on 2015 December 29. The bright companion candidate is seen at 1.1″ from HD 39007.

4.5.3 HD 27971

A bright companion candidate (ΔH =6.62)was detected at 0.6″ from HD 27971 as shown in Figure 4.10. Using NEXTGen model, we derived mass of the companion candidate, 0.61 $\pm$ 0.04 $M_{\odot}$ (J-band), 0.63 $\pm$ 0.04 $M_{\odot}$ (H-band), and 0.59 $\pm$ 0.06 $M_{\odot}$ (Ks-band). Also, we confirm that mass of the companion candidate adopted PARSEC isochrone model is same as derived from NEXTGen model. Considering mass derived from J-, H-, and Ks-band, we find that HD 27971 B has mass of 0.61 $\pm$ 0.02 $M_{\odot}$.

We calculated expected background stars using a Galactic model, the TRILEGAL model. The model estimates that the number of expected background star with in the FoV of HiCIAO is zero with a limiting magnitude of H $\sim$ 18.5. HD 27971 B is likely to be a companion.

4.5.4 HD 39007

A bright companion candidate, HD 39007 B, with Δ H =3.55 was detected at $\sim$ 1.1″ from HD 39007 A (Figure 4.10). Since NextGen model does not cover absolute magnitude of HD 39007 B, we adopt PARSEC isochrone model (Bressan et al., 2012) to convert flux to mass. Mass of HD 39007 B is 1.48 $\pm$ 0.05 $M_{\odot}$ by averaging three independent mass estimates.

The TRILEGAL model calculates the number of background stars within the FoV of HiCIAO to be three. Note that the magnitudes of excpected background stars are above 14 magnitudes in H-band. Therefore HD 39009 B may be the companion star.

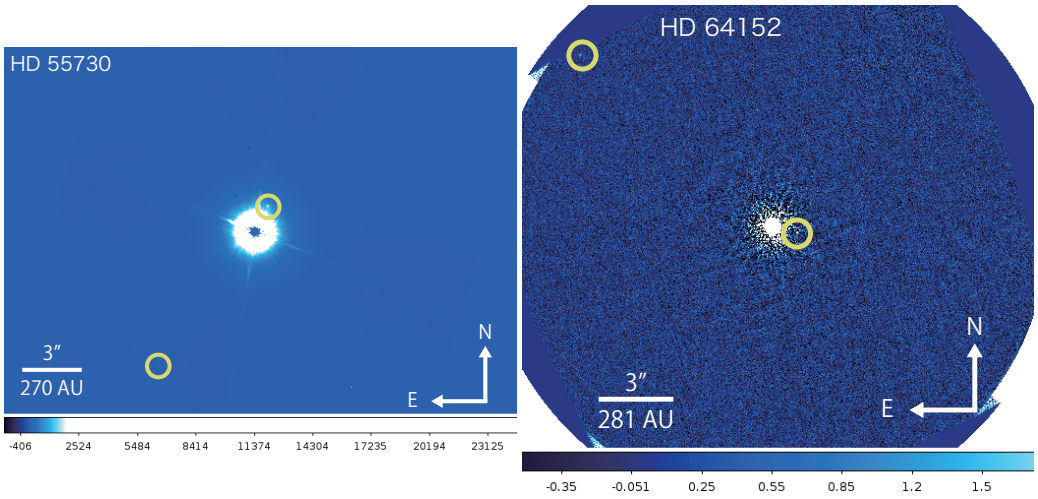

Figure 4.11: Detected companion candidates from HiCIAO observations. (Left) Image of HD 55730 in the H-band taken on 2015 December 30. Two companion candidates, at 1.4″ and 7.7 ″ can be seen in the figure. (Right) Image of HD 64152 in the H-band taken on 2015 December 30. North is up and east is left. The faint companion candidate was detected at 1.1″ from HD 64152.

4.5.5 HD 55730

Two companion candidates were detected. HD 55730 B is Δ H = 8.75 with a separation of 1.3″, and HD 55730 C is Δ H = 11.49 with a separation of 7.7″ (Figure 4.11). The Dusty 700Myr model was adopted to convert flux to mass. HD 55730 B's mass is 0.23 $\pm$ 0.02 $M_{\odot}$ and HD 55730 C's mass is 0.075 $\pm$ 0.007 $M_{\odot}$, which are suitable for Dusty model.

We calculated expected background stars using a Galactic model, the TRILEGAL model. The number of expected background stars is three. This indicates that detected companion candidates could be background star.

4.5.6 HD 64152

Faint companion candidates were detected in the observation (Figure 4.11). A close companion candidate, HD 64152 B, is Δ H = 14.4 at 0.96″. Another distant companion candidate, HD 64152 C, is Δ H = 14.88 at 9.97″. Using Dusty 700Myr model, we derive mass of companion candidates, HD 64152 B (0.050 $\pm$ 0.004 $M_{\odot}$) and HD 64152 C (0.048 $\pm$ 0.004 $M_{\odot}$). The TRILEGAL model expected that the number of background star is eleven with limiting magnitude of 20.5, suggesting companion candidates are background stars.

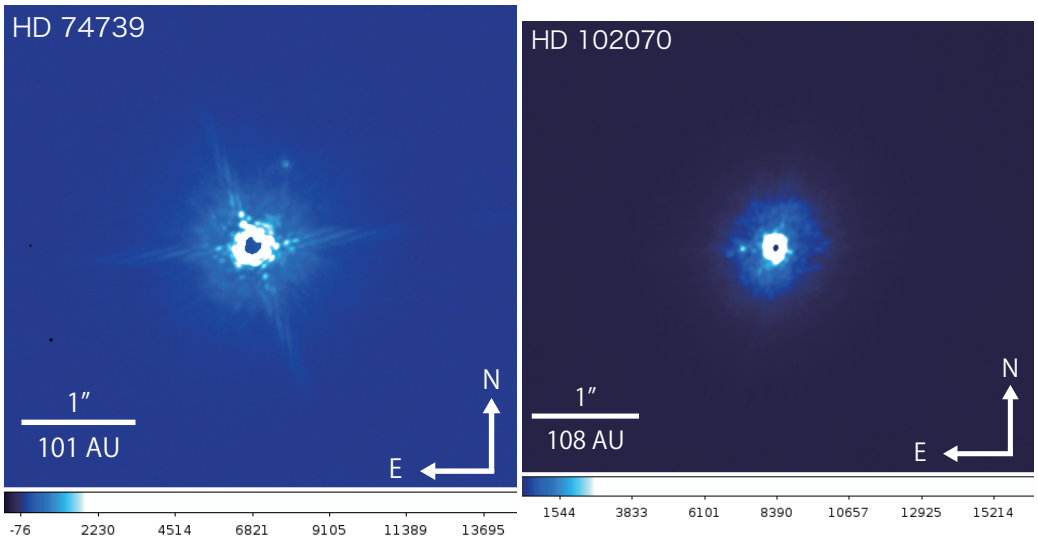

Figure 4.12: Detected companion candidates from HiCIAO observations. (Left) Image of ι Cnc A (HD 74739) in the H-band taken on 2015 December 29. The companion candidate at 0.7″ can be seen in the figure.
(Right) Image of HD 102070 in the H-band taken on 2015 December 30. The companion candidate was detected at 0.3″ from HD 102070.

4.5.7 ι Cnc A (HD 74739)

We detected a bright companion candidate shown in Figure 4.12. ι Cnc AB is Δ H = 3.5 located at 0.7″ from ι Cnc A. We convert flux to mass using NextGen model and obtain 0.96 $\pm$ 0.03 $M_{\odot}$ averaging 3 independent measurements. We also confirm that mass is 0.97 $\pm$ 0.04 $M_{\odot}$ using PARSEC isochrone model. We obtain that the number of expected background stars is zero using the Galactic model, TRILEGAL model with limiting magnitude of 20.9. This suggests the detected companion candidate is likely to be a real companion.

4.5.8 ζ Crt (HD 102070)

A bright companion candidate, HD 102070B, was detected as shown in Figure 4.12. HD 102070 B is Δ H =4.9 located at 0.3″ from HD 102070. We use PARSEC isochrone model to derive its mass from absolute magnitude of HD 102070 B because NextGen model does not cover its magnitude. HD 102070 B's mass averaging 2 independent measurements is 1.54 $\pm$ 0.15 $M_{\odot}$. The TRILEGAL model expects that none of stars is in the FoV of HiCIAO, suggesting HD 102070 B is possible to be a companion.

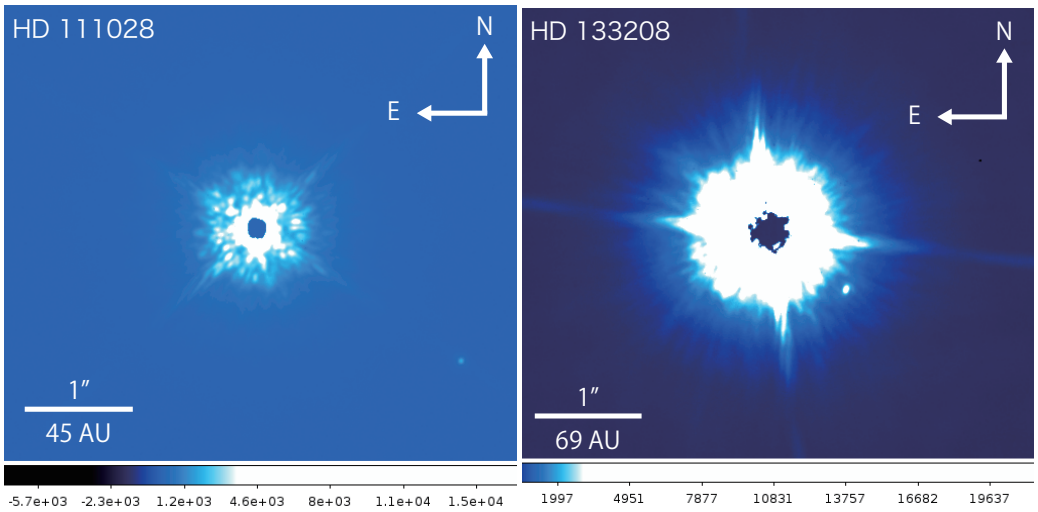

Figure 4.13: Detected companion candidates from HiCIAO observations. (Left) Image of HD 111028 in the H-band taken on 2015 December 30. The companion candidate at 2.2″ can be seen in the figure. (Right) Image of β Boo (HD 133208) in the H-band taken on 2015 December 30. North is up and east is left. The companion candidate was detected at 0.9″ from β Boo.

4.5.9 HD 111028

We detected a companion candidates (Δ H = 7.18), HD 111028, located at 2.2″ from HD 111028 (Figure 4.13). Using Dusty 3Gyr model, we derive 0.23 $\pm$ 0.02 $M_{\odot}$ as mass of HD 111028 B. We also check that mass derived from NextGen model is same. The TRILEGAL model expects background star is one with H=18.6. Considering expected background star's magnitude, we may count as HD 111028 B is a companion.

4.5.10 β Boo (HD 133208)

A bright companion candidate, β Boo B was detected (Figure 4.13). β Boo B is Δ H = 5.54 and its separation is 0.9″. β Boo B's mass derived from NextGen 0.3Gyr model is 0.58 $\pm$ 0.01 $M_{\odot}$. We confirm that mass derived from Dusty model is consistent. The number of expected background star from the Galactic model, TRILEGAL model, is zero, implying a gravitationally bounded companion.

Table 4.5: Astrometric and photometric results of companion candidates detected by NESSI

Name	Filter	Sep. (″)	P.A. (deg)	Δmag	Absolute mag.	Mass ($M_\odot$)
HD 10348 B	r	0.861	155.43	6.96	6.94	0.70
HD 74395 B	r	0.207	284.98	4.04	1.82	2.19

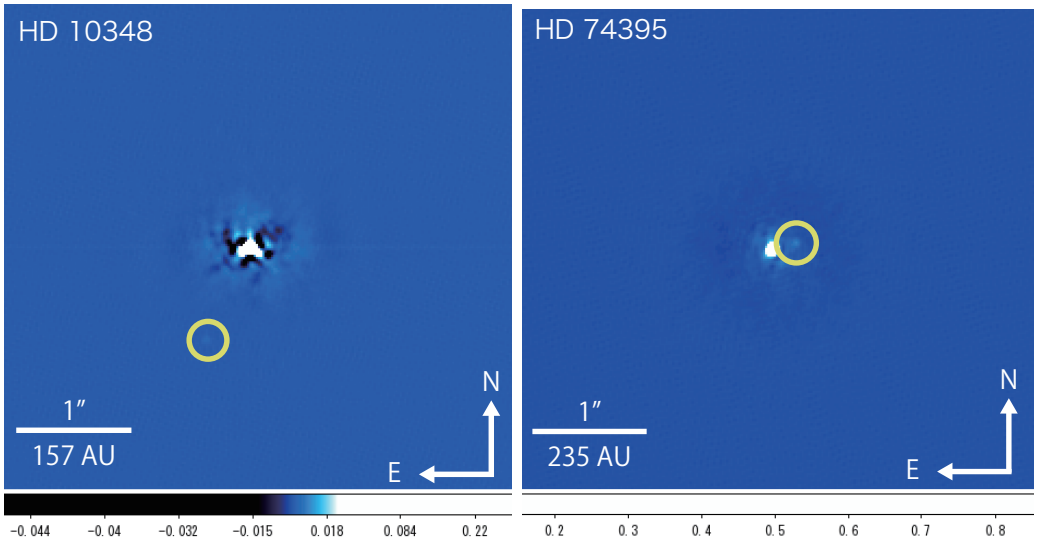

Figure 4.14: Detected companion candidates from NESSI observations. (a) Image of HD 10348 in r-band. North is up and east is left. The companion candidate was detected at 0.8″ from HD 10348. (b) Image of HD 74395 in r-band. The companion candidate at 0.2″ can be seen in the figure.

4.5.11 HD 10348

The companion candidate, HD 10348 B, with Δ r =6.96 was detected by NESSI/WIYN telescope (Figure 4.14). We use NextGen 0.3Gyr model to convert its flux to mass. We obtain its mass is 0.70 $M_\odot$. We assume that SDSS i-band is approximately the same magnitude of NESSI 832nm. Using PARSEC isochrone, we also confirm its mass is 0.67 $M_\odot$. We also confirm that mass derived from NextGen model is 0.70 $M_\odot$. The TRILEGAL model expects zero as the number of expected background stars. The companion candidate, HD 10348 B is supposed to be a companion.

4.5.12 HD 74395

The companion candidate, HD 74395 B, located at 0.2″ from HD 74395 was detected by NESSI/WIYN telescope (Figure 4.14). Since Next Gen model does not cover absolute magnitude of the detected companion, we use PARSEC isochrones model to derive its mass. HD 74395 B's mass is 2.19 $M_\odot$. Using the TRILEGAL model, we estimate that the number of background star is zero in the FoV of NESSI. This suggests that detected companion candidate is likely to be a companion.

Chapter 5

Discussion

In this chapter, we will discuss the origin of the observed RV trends using our observational results shown in previous chapters. Considering that detected companions and companion candidates can be responsible for the observed RV trends, we clarify the nature of these RV trends. In the case of no detection, we will constrain the semi-major axis and mass of RVTGs combining direct-imaging observation results and RV trends. In addition, we will discuss an influence of the RVTGs to inner planets. An outer companion gravitationally disturbs an inner planet to oscillate its eccentricity and inclination. This could be the origin of an eccentric planet.

5.1 RV Trend Generators

Combining the RV trend for the primary star with the projected separation of the detected companions, we can calculate the minimum dynamical mass that would be required to produce the RV trend with the following equation (Torres, 1999; Liu et al., 2002):

$$M_{\rm dyn} = 5.34 \times 10^{-6}\, M_{\odot} \left(\frac{d}{\rm pc} \frac{\rho}{\rm arcsec} \right)^2 \times \left| \frac{\dot{v}}{\rm m/s/yr} \right| F\left(i, e, \omega, \phi\right) \tag{5.1.1}$$

where d is the distance to the target, ρ is the observed angular separation of the companion (see also Knutson et al., 2014), and F is a function that depends on the orbital parameters (inclination i, eccentricity e, longitude of periastron ω, and orbital phase ϕ) of the companion. Torres (1999) determined that the minimum value of $F\left(i, e, \omega, \phi\right)$ is $3\sqrt{3}/2$. We use this equation to calculate the minimum mass limited by the RV trend. If the mass estimated from photometry exceeds the dynamical minimum mass derived from the RV trend, then we can conclude that a detected companion is responsible for the observed RV trend, and if not, the companion is not responsible for the observed RV trend.

Additionally, we calculate a physical (unprojected) separation of the detected companion from the central star, consulting Howard et al. (2010) who derived a true separation of a stellar companion around HD 126614 by combining the companion's estimated mass with the central star's RV trend. There are two solutions for each of the three companions. As a simplification, we do not consider projection effects on the orbit, but assume that the projected separation is equal to the semi-major axis when comparing imaging and RV limits. As shown in e.g. Brandeker et al. (2006), the statistical mean conversion factor between the semi-major axis and the projected separation is close to 1 for eccentricity distributions representative of wide binaries, which supports this approximation.

In the cases where no companion could be found, upper and lower limits for the companion as function of semi-major axis were calculated (see Figure 5.1). The lower mass limit from the RV trend is calculated from Equation 5.1.1, and the upper mass limit is set by the detectable mass limit of the direct-imaging observation. The object that could cause the RV trend is then constrained between these two limits.

Furthermore, the lack of curvature in a linear trend can be used to exclude the existence of inner companions. We assume that the time span of the observations must correspond to at most half an orbital period, or significant curvature would necessarily be seen. This sets a lower limit on the period, and thus an inner limit on the semi-major axis of the companion. In the following subsections, we will derive the parameters of each object from our observations, categorizing them in three cases.

5.1.1 Confirmed companion cases

γ Hya – With an angular separation of 1.623″ (2012 May 13), the dynamical minimum mass of γ Hya B is 0.25 $M_{\odot}$. The mass estimated from photometry, $0.61^{+0.12}_{-0.14}$ $M_{\odot}$, exceeds the dynamical minimum mass. Therefore, we conclude that γ Hya B is responsible for the observed RV trend. The physical separation is 67.5 ± 0.6 AU or 159 ± 7 AU.

HD 5608 – The dynamical minimum mass of HD 5608 B is 0.095 $M_{\odot}$ (2011 Dec. 31). Our photometric estimated mass is 0.10 ±0.01 $M_{\odot}$, which is consistent with the dynamical minimum mass derived from the RV trend. We confirm that the companion is the RV trend generator. The calculated physical separation is 40 ± 1 AU or 47 ± 3 AU.

HD 109272 – In the HD 109272 system, the dynamical minimum mass limit calculated with the angular separation on 2012 Apr. 11 is 0.12 $M_{\odot}$. The estimated mass from the photometry of HD 109272 B is 0.28±0.06 $M_{\odot}$. Therefore, we conclude that HD 109272 B is the RV trend generator for the observed RV trend in HD 109272 A. The true physical separation of HD 109272 B is 59.3 ± 0.9 AU or 140 ± 6 AU.

5.1.2 No companions cases

18 Del – Mugrauer et al. (2014) reported that 18 Del A has a distant companion 18 Del B outside the field of view of HiCIAO. The projected separation of 18 Del B is 2199 AU and its mass is 0.19 $M_{\odot}$. The dynamical minimum mass at 2199 AU is 181 $M_{\odot}$. Therefore, 18 Del B cannot be the source of the observed RV trend. The upper and lower limits for the RVTG are shown in Figure 5.1. In addition, the long-term linear RV trend would excludes the existence of inner objects. The semi-major axis range of the RVTG is $a \sim$ 10–50 AU. A stellar companion at wide separation is ruled out, though a low-mass stellar companion at the inner region is possible. The minimum mass at $a = 10$ AU is $m_p \approx 4$ $M_{\rm Jup}$, so the RVTG is either a high-mass planet, a brown dwarf, or a low-mass stellar companion. Planetary RVTG (4-13$M_{\rm Jup}$) range is 10-18 AU and planetary and brown dwarf RVTG (4-65 $M_{\rm Jup}$) is 10-45 AU.

ι Dra – The absence of the detection of any companions around ι Dra is consistent with the result observed by Kane et al. (2014) at 692 nm and 880 nm. An analysis combining the RV trend and the HiCIAO result is shown in Figure 5.1. Considering the linear RV trend observed over a decade (Kane et al., 2010), the possible innermost object is $m_p \approx 16$ $M_{\rm Jup}$ at$a = 9$ AU. On figure 5.1, the intersection of the observation detectable line with the dynamical minimum line derived from the RV trend is $a \approx 31$ AU. Hence, the semi-major axis range of the RVTG is $a \sim$ 9–31 AU. The mass range implies the RVTG is a brown dwarf or a stellar companion at small separation.

HD 14067 – From the observation result, we can determine limits for identifying the RVTG for HD 14067 (Figure 5.1). The linear RV trend over five years excludes objects in the inner region. The possible objects' orbital period is 10 years at least, which means that the innermost possible RVTG is at $a = 10$ AU in the HD 14067 system. The minimum dynamical mass at $a = 10$ AU in the system is $m_p \approx 32$ $M_{\rm Jup}$. On figure 5.1, the outermost possible RVTG is at $a \approx 49$ AU, where the detectable limit line crosses the dynamical minimum line. The dynamical minimum mass at $a \approx 49$ AU is $M_p \approx$ 0.74 $M_{\odot}$. We can rule out a wide-orbit stellar companion, though a stellar companion at $a \sim$ 10–49 AU is still possible. The RVTG for HD 14067 is a brown dwarf or a stellar companion at $a \sim$ 10–49 AU.

HD 360 – No detection of any companion candidate around HD 360 enables us to limit the nature of the RVTG for HD 360. The linear RV trend over 11 years point out that the absence of inner objects around HD 360. The possible innermost object of the

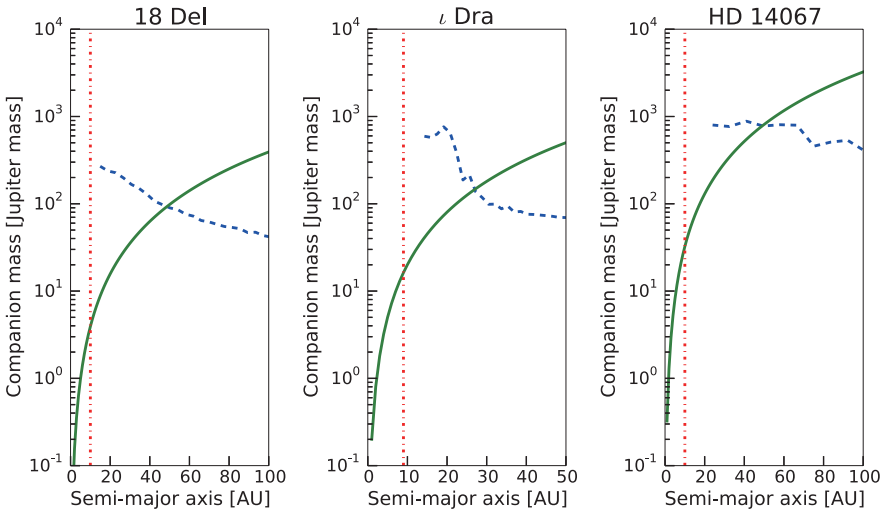

Figure 5.1: Combined analysis from the RV trend and direct imaging data for 18 Del, ι Dra, and HD 14067. The green line is the dynamical minimum mass derived from the observed RV trend, the blue dash line is the detectable mass limit from HiCIAO observation, and the red dot-and-dash line is the limit from the observational period of the RV observations.

RVTG is $a = 11$ AU. This corresponds $m_p \approx 12\ M_{\rm Jup}$. On figure 5.8, the intersection of the observation detectable line with the dynamical minimum line derived from the RV trend is $a \approx 75$ AU and m_p is 0.75 $M_\odot$. Therefore the semi-major axis range of the RVTG is $a \sim$ 11-75 AU. The mass range implies the RVTG is not a high mass companion.

HD 4188 – Considering no companion candidates around HD 4188, we limit the nature of the RVTG for HD 4188. The linear RV trend over 9 years indicates the absence of inner object $a < 10$ AU. The minimum dynamical mass at 9AU is 10 $M_{\rm Jup}$. Outer existing range is limited from combination with dynamical minimum mass and detection limit of HiCIAO observation, and is 40 AU, 0.20 $M_\odot$. Thus the RVTG for HD 4188 is a planet, or a brown dwarf, or a low-mass star located at 10-40 AU. Planetary RVTG range is 9-10 AU and sub-stellar RVTG range is 9-23 AU.

HD 15920 – The absence of companion candidates around HD 15920 offers us to limit the range of the RVTG for HD 15920. RV observations over 11 years and the linear RV trend exclude a object with $a < 10$ AU. The possible innermost object of the RVTG is $a = 10$ AU and $\approx 4\ M_{\rm Jup}$. The dynamical minimum mass line crosses the detectable mass limit of HiCIAO observation at ≈ 50 AU that corresponds to 0.12 $M_\odot$. Hence the RVTG is a planet or a brown dwarf or a low mass star at 10-50 AU. Planetary RVTG range is 10-18 AU, and sub-stellar RVTG range is 10-43 AU.

HD 120420 – No detection of any companion candidate around HD 120420 enables us to limit the range of semi-major axis and mass of the RVTG. Considering the linear RV trend over 10 years, we can exclude the object $a <$10 AU. The dynamical minimum mass at 10 AU from HD 120420 is $\approx 2\ M_{\rm Jup}$. Crossover point of dynamical minimum mass and detectable mass of the HiCIAO observation is 70 AU and $\approx 0.11\ M_\odot$. The RVTG for HD 120420 is a planet, a brown dwarf, or a low mass star located at 10-70 AU. Planetary RVTG range is 10-21 AU, and sub-stellar RVTG range is 10-52 AU.

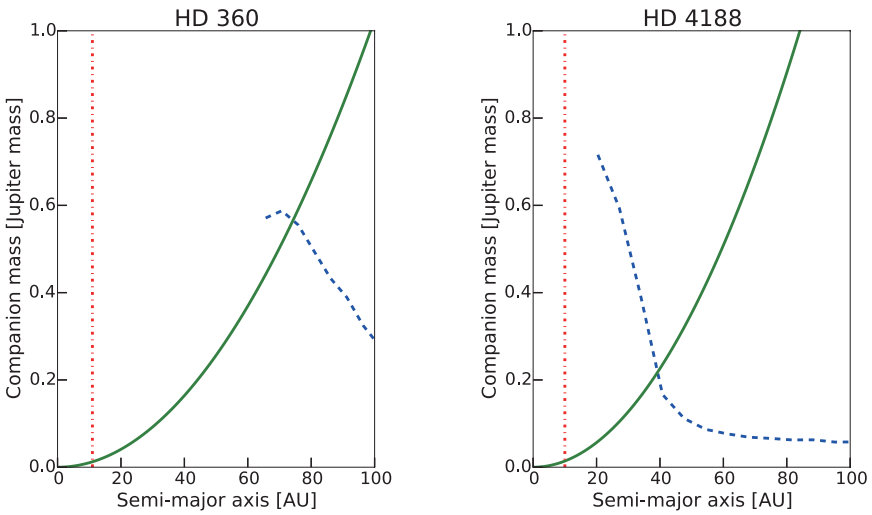

Figure 5.2: Combined analysis from the RV trend and direct imaging data for HD 360, and HD 4188. The green line is the dynamical minimum mass derived from the observed RV trend, the blue dash line is the detectable mass limit from HiCIAO observation, and the red dot-and-dash line is the limit from the observational period of the RV observations.

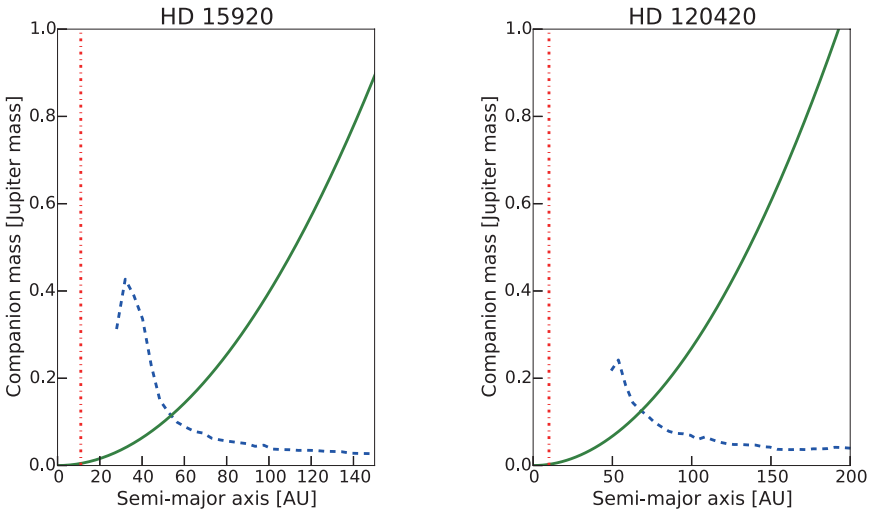

Figure 5.3: Combined analysis from the RV trend and direct imaging data for HD 15920, and HD 120420. The green line is the dynamical minimum mass derived from the observed RV trend, the blue dash line is the detectable mass limit from HiCIAO observation, and the red dot-and-dash line is the limit from the observational period of the RV observations.

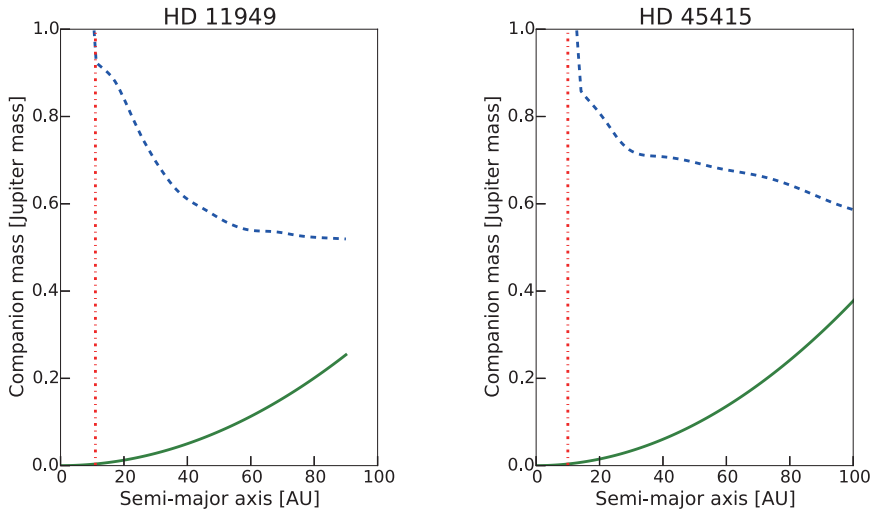

Figure 5.4: Combined analysis from the RV trend and direct imaging data for HD 15920, and HD 120420. The green line is the dynamical minimum mass derived from the observed RV trend, the blue dash line is the detectable mass limit from HiCIAO observation, and the red dot-and-dash line is the limit from the observational period of the RV observations.

HD 11949 – With no detection of any companion candidates around HD 11949, we limit the range of semi-major axis and mass of the RVTG. Long-term RV observations over 11 years exclude the existence of a object with $a < 11$ AU. The minimum dynamical mass at 11 AU is 4 $M_{\rm Jup}$. Due to the NESSI observation, we partially limit the range of mass and semi-major axis of the RVTG. The RVTG for HD 11949 is a planet, or a brown dwarf, or a low mass star with $11 < a$. Planetary RVTG range is 11-20 AU, and sub-stellar companion range is 11-48 AU.

HD 45415 – No detection of any companion candidates around HD 45415 offers us to limit the range of semi-major axis and mass of the RVTG. Considering the RV observation period, we can exclude the object $a < 11$ AU. The dynamical minimum mass at 11 AU is 4 $M_{\rm Jup}$. The dynamical minimum mass does not cross detectable mass from NESSI observation. Therefore we partially limit the existence range of the RVTG for HD 45415. The RVTG is a planet, or a brown dwarf, or a low mass star located at 11 AU $< a$. Planetary RVTG range is 11-18 AU, and sub-stellar RVTG range is 11-44 AU.

HD 54810 – From the NESSI observation result, we can exclude the existence of companion candidates around HD 54810. The linear RV trend over a decade indicates no companion candidates $a < 10$ AU. Innermost and lower limit of mass of the RVTG of HD 54810 is ≈ 2 $M_{\rm Jup}$. The dynamical minimum mass derived from the observed RV trend does not cross the detection limit mass of the NESSI observation. Hence we can only limit that the nature of the RVTG for HD 54810 is not a star like the Sun and a intermediate mass star. A planet is still possible for the RVTG. Planetary RVTG range is 10-26 AU, and sub-stellar RVTG range is 10-62 AU.

HD 65228 – No companion candidate around HD 65228 enables us to limit the nature of the RVTG for HD 65228. Since the RV observation have been conducted over a decade, innermost object is ≈ 0.05 $M_{\odot}$ at 12AU. The dynamical minimum mass crosses detection limit mass of NESSI is 1.1 $M_{\odot}$ at $\sim$ 54 AU. Thus we conclude that the RVTG for HD

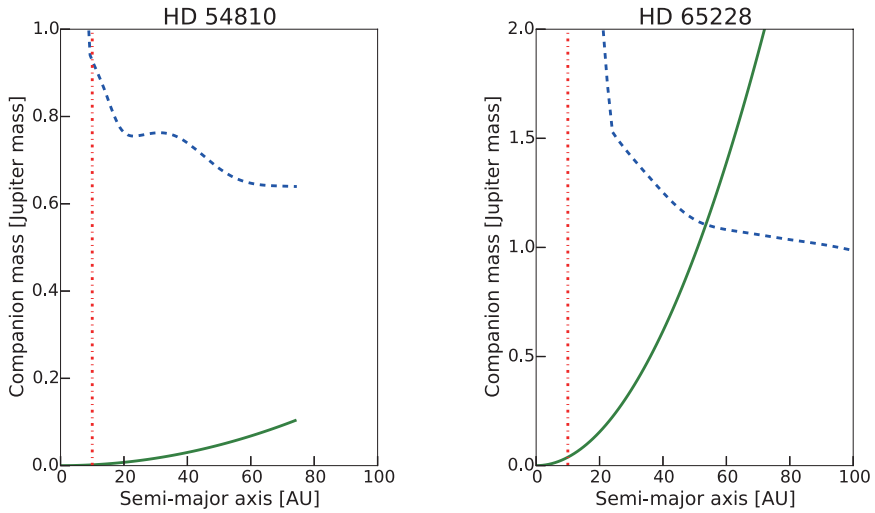

Figure 5.5: Combined analysis from the RV trend and direct imaging data for HD 54810, and HD 65228. The green line is the dynamical minimum mass derived from the observed RV trend, the blue dash line is the detectable mass limit from HiCIAO observation, and the red dot-and-dash line is the limit from the observational period of the RV observations.

65228 is not a planet, but a star located at 12-54 AU.

HD 95808 – The absence of companion candidate around HD 95808 offers us to limit the range of the RVTG for HD 95808. Over 8years observations, we can exclude any objects within $a \approx 9$ AU. The dynamical minimum mass at 9AU is $\sim 2\ M_{\rm Jup}$. Due to the FoV of NESSI, the dynamical minimum mass does not cross the detection limit of the NESSI observation result. We can exclude a solar type star for the cause of the RV trend. The RVTG for HD 95808 is a planet, a brown dwarf, and a low mass star. Planetary RVTG range is 9-21 AU, and sub-stellar RVTG range is 9-52 AU.

HD 106714 – Since no companion candidates around HD 106714, we can limit the nature of the RVTG for HD 106714. The linear trend over a decade corresponds to the absence of objects $a < 10$ AU. The dynamical minimum mass at 10 AU is $\sim 2M_{\rm Jup}$. Combining with the dynamical minimum mass and detection limit mass of NESSSI, we conclude that the RVTG for HD 106714 is a planet, or a brown dwarf, or a low mass star. Planetary RVTG range is 10-23 AU, and sub-stellar RVTG range is 10-56 AU.

HD 157527 – From no detection result of NESSI observation, we limit the range of semi major axis and mass of the RVTG. The linear RV trend over 8 years exclude the object with $a < 9$ AU. The minimum mass is 0.03 $M_{\odot}$ at 9AU. The cross-section of the dynamical minimum mass and detection mass limit of NESSI limits is 40 AU and ≈ 0.69 $M_{\odot}$. The RVTG for HD 157527 is possible for a brown dwarf, a low mass star located at $a =$ 9-40 AU.

HD 159353 – The lack of companion candidates around HD 159353 offers us to limit the nature of the RVTG. Long term RV observations over 11 years exclude the existence of objects with $a < 11$ AU. The dynamical minimum mass at 11 AU is 0.01 $M_{\odot}$. Out limit is 65 AU where the dynamical minimum mass crosses detection mass limit, 0.67 $M_{\odot}$. The RVTG for HD 159353 is a brown dwarf or a low mass star.

HD 162076 – From no detection of any companion candidates of observation result,

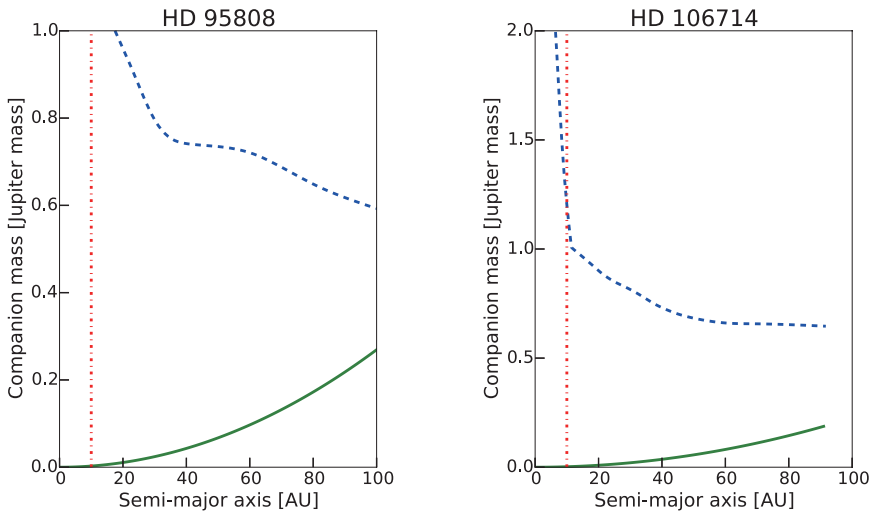

Figure 5.6: Combined analysis from the RV trend and direct imaging data for HD 54810, and HD 65228. The green line is the dynamical minimum mass derived from the observed RV trend, the blue dash line is the detectable mass limit from HiCIAO observation, and the red dot-and-dash line is the limit from the observational period of the RV observations.

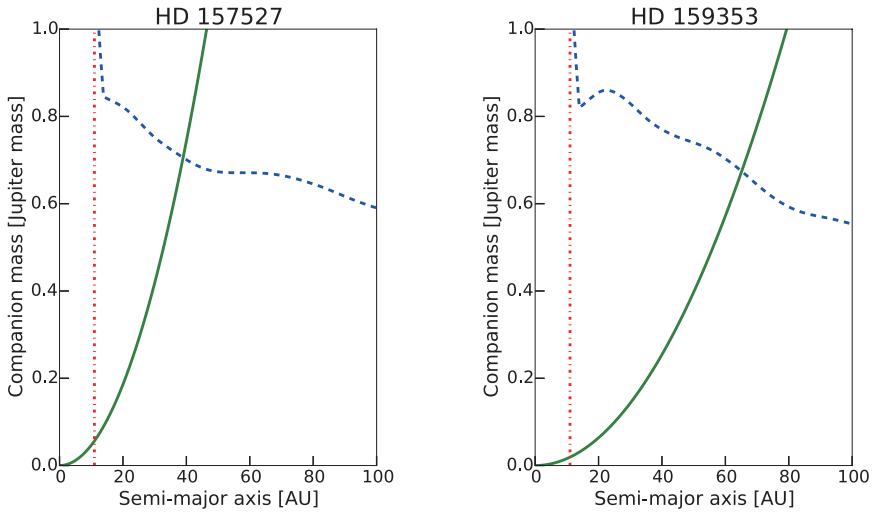

Figure 5.7: Combined analysis from the RV trend and direct imaging data for HD 157527, and HD 159353. The green line is the dynamical minimum mass derived from the observed RV trend, the blue dash line is the detectable mass limit from HiCIAO observation, and the red dot-and-dash line is the limit from the observational period of the RV observations.

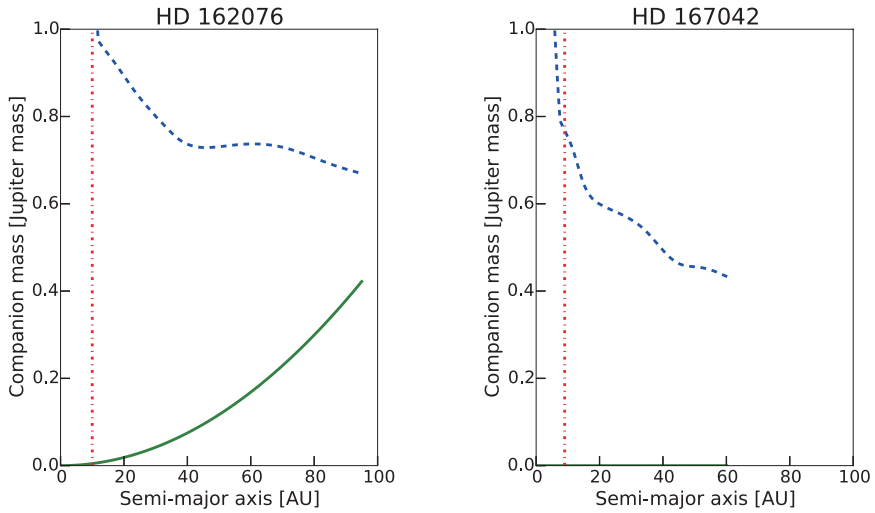

Figure 5.8: Combined analysis from the RV trend and direct imaging data for HD 167042. The green line is the dynamical minimum mass derived from the observed RV trend, the blue dash line is the detectable mass limit from HiCIAO observation, and the red dot-and-dash line is the limit from the observational period of the RV observations.

we partially limit the properties of the RVTG. Since the linear RV trend continues over 9 years, inner object $a < 10$ AU is excluded. The minimum mass at 10 AU is $\approx 5\ M_{\rm Jup}$. NESSI observation excludes the existence of a star $\gtrsim 1.0\ M_{\odot}$. Therefore the RVTG for HD 162076 is a brown dwarf or a low mass star with $a > 9$ AU.

HD 167042 – Since we cannot detect any companion candidate around HD 167042, we partly limit the nature of the RVTG. The linear RV trend continues over a decade excludes the object with $a < 9$AU. NESSI observation partly excludes the existence of stars. Since the RV trend is shelving, the dynamical minimum mass at 60 AU is 0.05 $M_{\rm Jup}$. Therefore the nature of the RVTG for HD167042 is a planet, a brown dwarf, or a low mass star. Planetary RVTG range is 9-900AU.

5.1.3 Companion candidate cases

In the case of companion candidate cases, we tried to examine that a companion candidate can be responsible for the observed RV trend, calculating minimum dynamical mass at the separation of the companion candidate. If the companion candidate cannot explain the observed RV trend, we limit the range of the RVTG in the same way as the no companion case.

HD 9408 – Since the RV of HD 9408 has curvature feature, we fit RV data and measure the slope of the RV trend. The minimum dynamical mass at the separation of HD 9408 B, HD 9408 C, and HD 9408 D are 113 $M_{\odot}$ at 5.7″, 191 $M_{\odot}$ at 7.4″, and 289 $M_{\odot}$ at 9.1″ to explain the observed RV trend. This indicates that detected companion candidates cannot be responsible for the observed RV trend.

We limit the range of RVTG for HD 9408 as shown in Figure. Inner limit from observation period is 0.08 $M_{\odot}$ at 10 AU. And outer limit is 50 AU and 0.55 $M_{\odot}$. The RVTG for HD 9408 is a low-mass star located at 10-50 AU.

HD 18970 – Using equation 5.1.1, we derive dynamical minimum mass at the separation of the detected companion candidate. The minimum dynamical mass at the separation of HD 18970 B, HD 18970 C, and HD 18970 D are 0.40 $M_{\odot}$, 6.5 $M_{\odot}$, and 14.9 $M_{\odot}$, respectively. This indicates that even if the detected companion candidate is gravitationally bounded as a real companion, it does not responsible for the observed RV trend. We calculated achieved contrast ratio and detectable mass limit in the observation (Figure 5.9).

Combining the dynamical minimum mass from the RV trend and the detectable mass from the HiCIAO observation, we limit the range of semi major axis and mass of the RVTG for HD 18970. Inner limit from observation period is 11 AU and 5 $M_{\rm Jup}$. Outer limit where dynamical minimum mass crosses detectable mass is 40 AU and 0.06 $M_{\odot}$. The RVTG for HD 18970 is a planet or a brown dwarf or a low mass stellar companion. Planetary RVTG range is 11-16 AU, and sub-stellar RVTG range is 11-42 AU.

HD 27971 – We evaluate whether the detected companion candidate, HD 27971 B, exceed the dynamical minimum mass derived from the observed RV trend. The dynamical minimum mass at the separation of HD 27971 B is 0.43 $M_{\odot}$ that is less than mass of HD 27971 B, 0.61 $\pm$ 0.02 $M_{\odot}$. Since the Galactic model estimates that the probability of background stars is low, the RVTG for HD 27971 is probably the detected companion, HD 27971 B.

HD 39007 – Using 5.1.1, we derive dynamical minimum mass at the separation of the detected companion candidate. The minimum dynamical mass at the separation of HD 39007 B, 1.1″, is 0.72 $M_{\odot}$. Mass of HD 39007 B derived from photometry is 1.48 $\pm$ 0.05 $M_{\odot}$ that exceeds the dynamical minimum mass. Considering the brightness expected from the Galactic model, the probability that HD 39007 B is a background star is low. Therefore we conclude that the RVTG for HD 39007 is likely to be HD 39007 B.

HD 55730 – We detected two companion candidates, HD 55730 B, and HD 55730 C. The dynamical minimum mass is 0.61 $M_{\odot}$ for HD 55730 B (1.3″), and 21 $M_{\odot}$ for HD 55730 C (7.7″). This means that two companion candidates are not responsible for the observed RV trend. We calculated achieved 5 σ contrast and detectable mass limit of the HiCIAO observation.

We limit the range of the RVTG. RV observations conducted over 12 years exclude the existence of inner objects. Dynamical minimum mass at inner limit 11 AU is 5 $M_{\rm Jup}$. Outer limit of semi major axis of the RVTG for HD 55730 is 40 AU. Thus the nature of the RVTG for HD 55730 is a planet or a brown dwarf with the semi major axis within 11-40 AU. Planetary RVTG range is 11-20 AU, and sub-stellar RVTG range is 11-40 AU.

HD 64152 – Detected companion candidates, HD 64152 B and HD 64152 C. Using 5.1.1, we derive dynamical minimum mass at the separation of the detected companion candidate. The minimum dynamical mass at the separation of HD 64152 B and HD 64152 C are 0.63 $M_{\odot}$, and 67 $M_{\odot}$, respectively. This represents that detected companion candidates cannot be the RVTGs.

Using RV data and detection limit of HiCIAO observation, we limit the range of semi major axis and mass of the RVTG for HD 64152. The object within 11 AU is excluded by the observation period, and dynamical minimum mass at 11 AU is 10 $M_{\rm Jup}$. Also object beyond 50 AU is excluded by the combination with dynamical minimum mass and detectable mass. Therefore the RVTG for HD 64152 is a planet, or a brown dwarf, or a low mass stellar companion. Planetary RVTG range is 11-12 AU, and sub-stellar RVTG range is 11-30 AU.

ι Cnc A (HD 74739) – We examine that ι Cnc AB mass exceeds the dynamical minimum mass. The dynamical minimum mass of ι Cnc AB is 0.51 $M_{\odot}$. The mass estimated from photometry, 0.96 $\pm$ 0.04 $M_{\odot}$, exceeds the dynamical minimum mass. ι

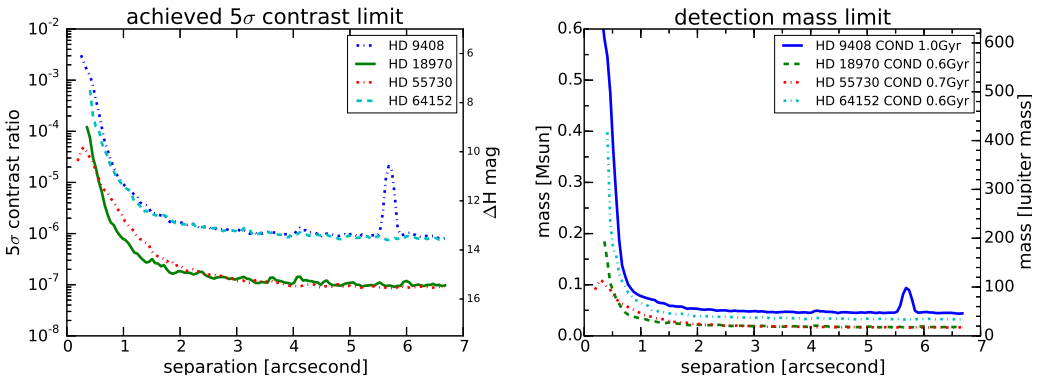

Figure 5.9: Left: Achieved 5σ contrast ratio for HD 9408 in the H-band, for HD 18970 in the H-band, for HD 55730 in the H-band, and for HD 64152 in the H-band. Right: Detectable mass limits for HD 9408, HD 18970, HD 55730, and HD 64152.

Cnc AB is probably responsible for the observed RV trend because the possibility of background stars is low.

ζ Crt (HD 102070) – The dynamical mass derived from the observed RV trend is 0.49 $M_\odot$ at the separation of HD ζ Crt B. The mass of ζ Crt derived from HiCIAO observation is 1.54 ± 0.15 $M_\odot$ that exceeds the dynamical minimum mass. Since expected number of background star is zero, we conclude that the RVTG for ζ Crt is likely to be ζ Crt B.

HD 111028 – With the separation of HD 111028 B, the dynamical minimum mass is 0.23 $M_\odot$. The mass derived from photometry is 0.23 ± 0.02 $M_\odot$, which is consistent with the dynamical minimum mass. As written in result section, HD 111028 B may be a companion. We consider HD 111028 B as the RVTG for HD 111028.

β Boo (HD 133208) – The dynamical mass at the separation of β Boo, $0.9''$, is 0.39 $M_\odot$. The mass β Boo B derived from HiCIAO observation, 0.58 ± 0.01 $M_\odot$ exceeds it. We conclude that β Boo B is responsible for the observed RV trend because of the low probability of background stars.

HD 10348– We evaluate that the detected companion candidate, HD 10348 B, can be responsible for the observed RV trend. The dynamical minimum mass at the separation of HD 10348 B, $0.86''$, is 0.50 $M_\odot$. The mass of HD 10348 B derived from photometry exceeds it. Therefore HD 10348 B is supposed to be the RVTG for HD 10348.

HD 74395–At the separation of HD 74395 B, $0.2''$, the dynamical minimum mass is 0.84 $M_\odot$. The mass derived from NESSI observation is 2.19 $M_\odot$ that exceeds the dynamical minimum mass. The Galactic model suggests there are no background stars. From the above, we conclude that HD 74395 B is responsible for the observed RV trend.

5.1.4 Summary of RVTG

We limit the mass range of the RVTGs, combining RV data and direct imaging observation results. Thirteen targets have possibilities of planetary RVTGs. From HiCIAO observations, it is seven targets 18 Del, HD 4188, HD 15920, HD 120420, HD 18970, HD 55730, and HD 64152. And it is six targets from NESSI observations, HD 11949, HD 45415, HD 54810, HD 95808, HD 106714, and HD 167042. The possible planetary RVTG range is 9-26AU, and sub-stellar RVTG is 9-62 AU.

Not only we limit the nature of RVTGs, but also detect companions. Detected com-

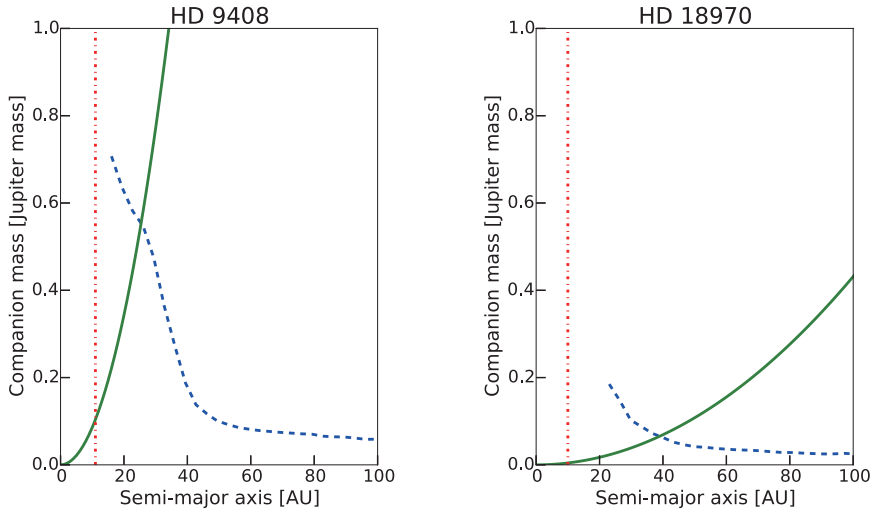

Figure 5.10: Combined analysis from the RV trend and direct imaging data for HD 9408, and HD 18970. The green line is the dynamical minimum mass derived from the observed RV trend, the blue dash line is the detectable mass limit from HiCIAO observation, and the red dot-and-dash line is the limit from the observational period of the RV observations.

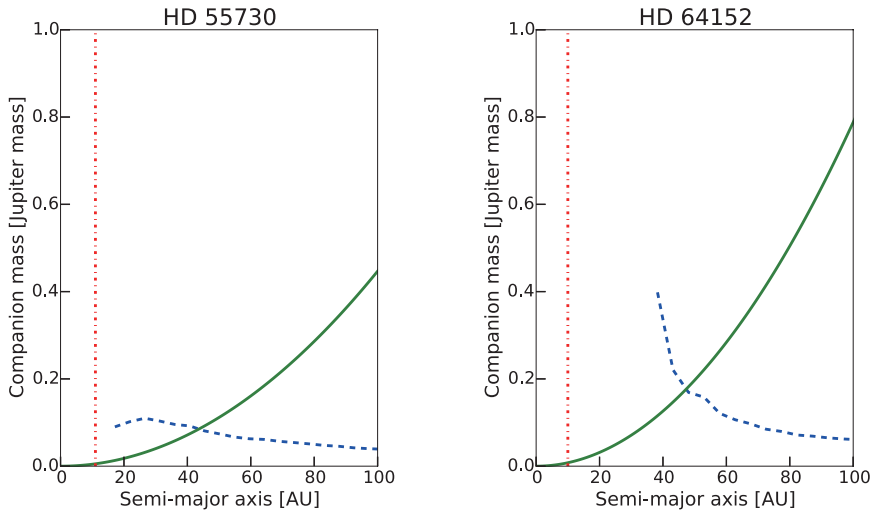

Figure 5.11: Combined analysis from the RV trend and direct imaging data for HD 55730, and HD 64152. The green line is the dynamical minimum mass derived from the observed RV trend, the blue dash line is the detectable mass limit from HiCIAO observation, and the red dot-and-dash line is the limit from the observational period of the RV observations.

panion cases are three, γ Hya, HD 109272, HD 5608. Likely companion cases are eight, HD 27971, HD 39007, ι Cnc A, ζ Crt, HD 111028, β Boo, HD 10348, HD 74395.

5.2 Distant planet rate and implication for its formation model

With our results shown above, we will discuss planetary occurrence rates and binary rates (or frequencies). For planetary frequency, we compare our planetary frequency with that of previous works of direct imaging surveys for main-sequence stars (Galicher et al., 2016; Vigan et al., 2017). For binary rates, we compare our binary rate of RV trend targets with those of binaries listed in Duchéne & Kraus (2013).

5.2.1 Planet occurrence rate

The sample number of the OAO RV survey is 322 stars and that of potential distant planet host stars is thirteen. Since we have not discovered distant planets via direct imaging among the thirteen candidates, we are able to derive a rough estimate of the occurrence rate (upper limit) of distant planets around intermediate mass giants. To derive occurrence rate strictly, we should consider the probabilities that a planet is not detected in an RV trend (false negative) and an RV trend is not generated by a planet (false positive).

To estimate how many planets are missed in RV trends sample, we need to determine an RV trend detection efficiency. The RV trend detection efficiency is determined by an "injection test". Artificial companions are injected in RV data and it is determined that the injected companion can be detected or not. However, we do not know the distant planet distribution around intermediate mass giants. Therefore, we will extrapolate distant planet distribution from previous inner planet distribution around solar type stars, which may be different from that of intermediate mass giants.

To estimate a detection efficiency of an RV trends, we regard RV residuals of our samples as RV trend non-detection RVs. The artificial RVs generated by long-term planets were injected into these residuals to conduct trend detection tests. The criteria for detection is that the RV variation exceeds three times root mean square of the residual. The grid of companion masses and semi-major axis are 20 $\times$ 10 in the range of $1 \leq M_p/M_{\rm Jup} \leq 100$ and $10 \leq a/AU \leq 100$ in logarithmic space. We test 500 planets at each point, and orbital inclination i, argument of periapsis ω are randomly assigned. The eccentricity is randomly drawn from beta distribution with $\alpha = 0.867$ and $\beta = 3.01$ determined by Kipping (2013).

We conduct the RV detection test using RV residuals of HD 360 with 22.0 m/s rms in the case of maximum rms without outlier, while RV residuals of HD 39007 with 13.1 m/s as typical rms in our Okayama RV survey samples (Figure 5.12). Web have checked that the distribution of our RV trend samples is the same as that of the whole Okayama RV survey samples. Therefore HD 360 and HD 39007 can be representative to estimate RV trend detection efficiencies for the Okayama RV survey samples. The results are shown in Figure 5.13. Median RV trend in possible planet RVTGs is 2.8 m s^{-1} yr^{-1}. For HiCIAO possible planet RVTGs, median RV trend is 3.0 m s^{-1} yr^{-1}. Minimum dynamical mass (Torres, 1999) at 10 AU for 3 m s^{-1} yr^{-1} is $\sim$ 4 $M_{\rm Jup}$. The typical detection fraction of 4 $M_{\rm Jup}$ at 10 AU of HD 360 is $\sim$ 0.20. Therefore we adopt 0.20 as detection efficiency to correct missing RV trends.

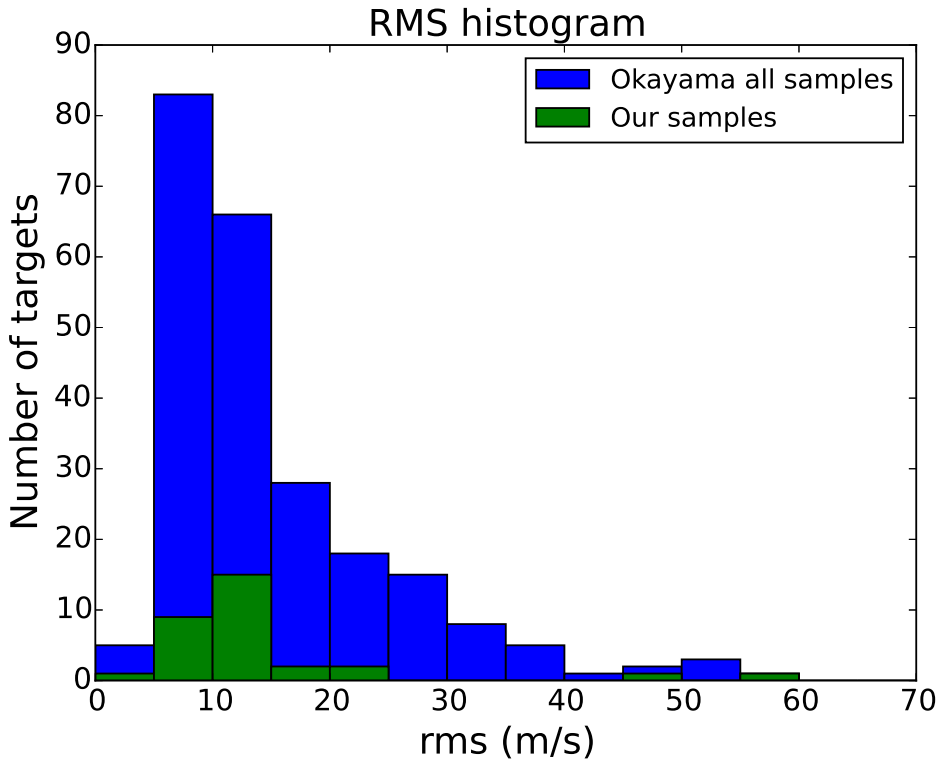

Figure 5.12: A histogram of root mean square (rms) of RV trend fitted residual of OAO samples and our RV trend samples. Obvious binary (rms $>$ 500 m/s), planet, and trend systems were excluded from OAO samples in this plot. The typical rms of our samples is $\sim$ 10 m/s.

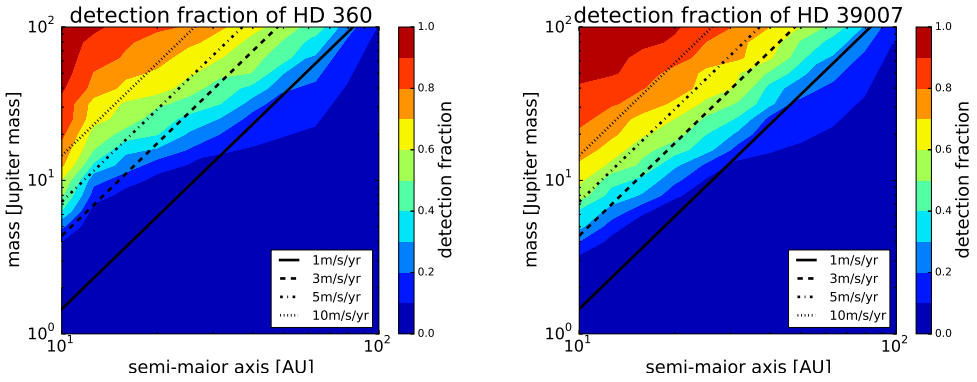

Figure 5.13: The result of trend detection efficiency. The grid of each figure is 20 $\times$ 10 for mass and semi-major axis. Color contous show that the detection fraction of 500 artificial injected objects at each grid point. Each line represents the minimum dynamical mass derived from Torres (1999) of each RV trend value.

Besides distant planets there are other factors that can induce RV trends. A white dwarf companion is a factor that can generate an RV trend. Holberg et al. (2013) estimate frequency of main sequence-white dwarf system, "Sirius-like system" is 1/80-1/175 for nearby A to K main sequence stars. We adopt that the white dwarf contamination probability is 1/80. We then discuss that whether HiCIAO could detect white dwarfs as faint companion candidates. Converting absolute magnitude of Sirius B in H-band ($12.06^{+0.23}_{-0.16}$ Bonnet-Bidaud & Pantin, 2008) to apparent magnitude at 100 pc which is a typical value of our sample, we obtain 17 magnitude; this is above the detection limit of 18 Del ($\sim$ 19.5) but below that of HD 4188 ($\sim$ 16.5). We thus conclude that HiCIAO observations could detect white dwarfs but the probability of missing white dwarfs is not negligible. Therefore we consider white dwarf fraction, 1/80.

Another factor that can generate the RV trend is missing stellar companions such as face-on stars. This is because we did not include such stellar companions of $> 100 M_{\rm Jup}$ masses in our simulation above. If a stellar companion exists very near the target, such a close binary is detected as a spectroscopic binary. To support this, Duchéne & Kraus (2013) report that the companion orbital distribution around intermediate mass stars has two peaks, $P \approx 10$ days and $a \approx 350$ AU. Short period stellar companions can be detected in RV observations, while long period stellar compainons can be detected in direct-imaging observations. We consider that missing stellar companions are limited range as discussed in section 5.1. We also note that the probability of planets, not face-on stellar companions, can be estimated by the method of Ho & Turner (2011).

Following above discussion, we derive that a rough estimate of an upper limit of distant planet occurrence rates around intermediate mass giants is 13/322 /0.2 $\times$ (1-1/80)$\approx$20 %. Our result is for 9-26 AU for planetary RVTG ($4 M_{\rm Jup} \leq M \leq 13 M_{\rm Jup}$), and 9-62 AU for sub-stellar RVTG ($4 M_{\rm Jup} \leq M \leq 70 M_{\rm Jup}$. This occurrence rate is an upper limit.

Cumming et al. (2008) analyze the Keck Planet Search RV data and determine that a mass-period distribution of close-in (P <2000days) gas giants ($> 0.3 M_{\rm Jup}$) around F-M type stars is $dN = C M^{\alpha} P^{\beta} d\ln M d\ln P$ with $\alpha = -0.31 \pm 0.20$ and $\beta = 0.26 \pm 0.10$. Increasing period makes increasing gas giant planets. Fischer & Valenti (2005) report that high metalicity stars tend to host gas giants from Keck, Lick, and Anglo-Australian Telescope RV planet search programs. Johnson et al. (2010) show that the gas giant planet occurrence increases with stellar masses from the California Planet Survey targets.

Galicher et al. (2016) determined that the occurrence rate of giant planets 0.5-14 $M_{\rm Jup}$ and 20-300 AU is $1.05^{+2.80}_{-0.70}$% via direct imaging survey using NIRC2/Keck II, NIRI/Gemini North, NICI/Gemini South, and NACO/VLT. Vigan et al. (2017) also determined that the sub-stellar companion (0.5-75 $M_{\rm Jup}$) frequency was within 0.75–5.70 % at 68 % confidence level.

How can these occurrence rates be compared with the planet formation models? Core-accretion planet formation model explains these inner RV planet distribution features well. Mordasini et al. (2012) show that the massive planet frequency is peaked at a few AU. Kennedy & Kenyon (2008) show that the probability of gas giant host stars increases with stellar masses from 0.4 to 3 $M_{\odot}$ due to the disk mass. Ida et al. (2013) including protoplanet scattering and migration suggest that the fraction of distant ($a \geq 30$ AU) massive gas giants ($M_p \geq 10 M_{\rm Jup}$) is $\sim$ 3.7 % with low eccentricity.

Since gravitational instability occurs at large separations, it is difficult to explain these inner planet distribution. Furthermore, Janson et al. (2012) find that the mass and semi-major axis range allowed for gravitational instability formation is limited, and conclude that core accretion is likely dominant for the total planet population. Recent population synthesis model (e.g. Forgan et al., 2015; Müller et al., 2018) show that planets can be

Table 5.1: Comparison to other direct imaging survey results

stellar type	occurrence rate(%)	separation(AU)	Planet mass ($M_{\rm Jup}$)	reference
GK giants	<20	9-62	2-75	this work
GK giants (HiCIAO group)	<10	9-62	2-75	this work
FGKM main sequence	$1.05^{+2.80}_{-0.70}$	20-300	0.5-14	Galicher et al. (2016)
FGK main sequence	0.75-5.70	20-300	0.5-75	Vigan et al. (2017)

detected at several tens AU if gravitational instability is dominant to form distant planets (Figure 5.14). However, the above low detection rates of the distant planets via direct-imaging observation result do not support this scenario, suggesting that gravitational instability is rare to form distant planets (Vigan et al., 2017).

Our derived upper limit is 20 % and a first clue to understand distant planet occurrence rates around intermediate mass giants. Our upper limit is higher than previous direct imaging results (Table 5.1). Also our result is an upper limit, and we could not distinguish between core accretion model and gravitational instability model for distant planet formation.

In addition, considering that speckle imaging could lack companions, we note that our upper limit could be down to 10%. We consider contrast difference between HiCIAO instrument and NESSI instrument. To check that the speckle instrument can lack companions, we then briefly discuss binary rates of intermediate stars based on our imaging results. We used binomial tests, which is based on the binomial distribution defined as

$$P[X = k] = \binom{n}{k} p^k (1-p)^{n-k} \tag{5.2.1}$$

where x is the probability variable, n and k are trials and successes, and p is probability of the trial. Including likely companion cases, we derive the binary rate as 34% (11/32). For HiCIAO observation group, binary rate is 45% (9/20). For NESSI observation group, binary rate is 16% (2/12). One should note that the high companion rate in the HiCIAO group is most likely due to the HiCIAO's higher contrast than the NESSI's contrast.

For binary rate, Duchéne & Kraus (2013) concluded that companion fraction rate around field intermediate mass stars is $\geq$ 50 %. Our result of 34% was statistically identical with a probability of 0.055. Dividing into HiCIAO group and NESSI group, we also evaluate the probability of these rates, 9/20 and 2/12 using binomial tests. The probabilities for HiCIAO group and NESSI group calculated by binomial test are 0.41 and 0.02, respectively. Thus we find no difference between field stars and HiCIAO group. Contrary to HiCIAO group, the probability of NESSI group calculated by binomial test indicates that speckle observations are not deep to identify the RVTGs because the RV trend samples observed by HiCIAO do not have significant difference from field binary rate. Lacking stellar companions in speckle observations suggests that our potential planetary RVTG host stars observed by NESSI could be false positive.

Therefore our upper limit of distant planet occurrence rate around intermediate mass giants can be 7/322 /0.2 $\times$ (1-1/80)$\approx$10 % when we consider that NESSI observations could overlook companions. This is still higher than previous direct-imaging results, but suggests that distant planets via gravitational instability model is not dominant in outer region as same as the previous studies.

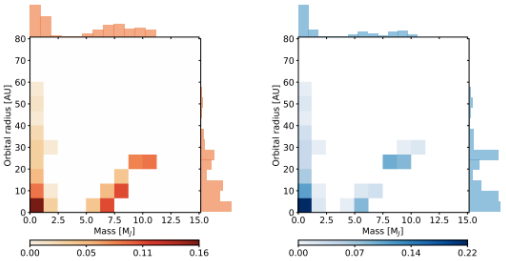

(c) 1.4 $M_\odot$ (d) 2.4 $M_\odot$

Figure 5.14: Gravitational instability simulation result from Müller et al. (2018). Each color shows ratio of surviving clumps. The simulation includes gap opening and migration.

5.3 Mechanism Influencing the Orbit of Inner Eccentric Planets

Several studies have revealed that the formation mechanism of eccentric planets cannot be explained by core accretion theory and Type I/II migration. The Kozai mechanism, which is a perturbation mechanism from a distant stellar companion (e.g. Wu & Murray, 2003), planet–planet scattering (e.g. Nagasawa et al., 2008), and secular chaotic excursions (e.g. Wu & Lithwick, 2010) are promising approaches to describe eccentric planets.

Among our sample, four targets have already known inner planets (Table 3.9). We discuss the Kozai mechanism to explain the eccentric planets, namely a perturbation due to an outer stellar companion periodically oscillates the eccentricity and inclination of an inner planet. The oscillation timescale of the Kozai mechanism is calculated by

$$P_{\rm Kozai} \sim \frac{M_A}{m_B} \frac{P_B^2}{P_{b,0}} \left(1 - e_B^2\right)^{3/2} \tag{5.3.1}$$

where M_A is the primary star's mass, m_B is the stellar companion's mass, P_B is the period of the companion, $P_{b,0}$ is the initial period of the planet, and e_B is the eccentricity of the companion (Holman et al., 1997).

We calculated the timescale of the Kozai mechanism for the significantly high eccentricity planets ι Dra b, HD 5608 b, and HD 14067 b. For ι Dra b, we assume that its companion has a mass of 0.18 $M_\odot$ and in a circular orbit at 31 AU, which is the maximum mass and separation. We then assume that the initial period of the planet is equal to that of a circular orbit of the observed semi-major axis. The timescale is $P_{\rm Kozai} \sim$ 107 kyr, which is much less than the Gyr order of ι Dra's age. The timescale for HD 5608 b, assuming the circular orbit of HD 5608 B, is $P_{\rm Kozai} \sim$ 450 kyr or 277 kyr. The timescale for HD 14067 b is $P_{\rm Kozai} \sim$ 30 kyr with the 0.74 $M_\odot$ object at 49 AU. These timescales are also sufficiently shorter than the system's ages. It follows from equation (5.3.1) that if the planets have migrated inward from an initially wider separation, then the initial Kozai timescales would be even shorter. Therefore, we conclude that the Kozai mechanism could be a plausible explanation for the eccentricity of the planets ι Dra b, HD 5608 b, and HD 14067 b. We note that an alternative mechanism for producing high eccentricities is planet-planet scattering. This possibility can be tested by continuing RV and direct imaging observations, in order to search for additional planets in the systems, as well as providing improved constraints for the orbits of the imaged companions.

Chapter 6

Summary

We present direct-imaging results of intermediate-mass stars with long-term radial velocity (RV) trends that suggest the existence of an outer object. We used HiCIAO on the 8.2m Subaru telescope and NESSI on the 3.5m WIYN telescope to identify the objects responsible for the observed RV trends. Our observations revealed that the three evolved intermediate-mass stars γ Hya, HD 5608, and HD 109272 possess the stellar companions γ Hya B, HD 5608 B, and HD 109272 B, respectively. We also ruled out the presence of stellar companions and brown dwarfs for separations from $1''$ to $7''$ for ι Dra, 18 Del, HD 14067, HD 360, HD 4188, HD 15920, HD 120420 using HiCIAO, while NESSI observations ruled out the presence of stellar companions around HD 11949, HD 45415, HD 54810, HD 65228, HD 95808, HD 106714, HD 157527, HD 159353, HD 162076, and HD 167042. We also detected companion candidates around twelve targets, HD 9408, HD 18970, HD 27971, HD 39007, HD 55730, HD 64152, HD 74739, HD 102070, HD 111028, and HD 133208 using HiCIAO, HD 10348, and HD 74395 using NESSI.

We have constrained the nature of the RV trend generators (RVTGs) around each of the thirty one targets. The detected companions γ Hya B, HD 5608 B, and HD 109272 B exceed the minimum dynamical mass derived from the combination of RV and direct imaging observations. We confirm that these companions are responsible for the observed RV trends. We also calculated the upper and lower limits of the mass and the semi-major axis for the RVTGs of ι Dra, 18 Del, HD 14067, HD 360, HD 4188, HD 15920, HD 120420, HD 11949, HD 45415, HD 54810, HD 65228, HD 95808, HD 106714, HD 157527, HD 159353, HD 162076, and HD 167042. For companion candidate stars, we evaluate that detected companion candidates can be the RVTG by calculating dynamical minimum mass to make observed RV trends. Eight detected companion candidates that are likely to be gravitationaly bound, HD 27971 B, HD 39007 B, ι Cnc AB, ζ Crt B, HD 111028 B, β Boo B, HD 10348 B, and HD 74395 B are supposed to be the RVTGs. We found that companion candidates of four targets, HD 9408, HD 18970, HD 55730, and HD 64152 could not be responsible for the observed RV trends.

Thirteen targets are potential distant planet host stars. Evaluating a detection efficiency of RV trends and white dwarf contamination, we estimate that an upper distant planet occurrence rate around intermediate mass giants is $< 20\%$. This is a first suggestion for the distant planet occurrence rate around intermediate mass giants. The targets observed by HiCIAO do not have a significant difference rate from the field binary one. The binary rate of targets observed by NESSI indicates that speckle observations could lack stellar companions. Considering that NESSI observations could overlook companions, we can obtain that an upper limit of the distant planet occurrence rate around intermediate mass giants is 10%.

For the three eccentric planet systems, ι Dra b, HD 5608 b, and HD 14067 b, the Kozai oscillation timescales are significantly shorter than their age, and thus the Kozai mechanism is a plausible explanation for the eccentricity of the planets.

Our study have shown the effectiveness of combining direct-imaging and RV data for intermediate mass giants to reveal the distribution of planets, which is a clue to understand planetary formation. Combining direct-imaging and RV data has a power to limit the distant planet occurrence rate. However, our direct imaging observations have a limited contrast and a limited inner working angle. An extreme AO technique such as SCExAO on the Subaru telescope offers us a higher contrast and thus enables to more precisely distinguish the cause of an RV trend between a planet and a low mass star or a brown dwarf.

Since the sample number of our observations is not large enough, further observations will improve the distant planet occurrence rate around intermediate mass giants. Understanding planets around intermediate mass giants is important for planet formation

theory to check the impact of different main star ' s mass. Our future study using extreme AO of large number of samples will contribute the nature of distant planet around intermediate mass giants to more precisely limit the planet formation theory.

References

Baines, E. K., McAlister, H. A., ten Brummelaar, T. A., et al. 2011, "Fundamental Parameters of the Exoplanet Host K Giant Star ι Draconis from the CHARA Array", ApJ, 743, 130B

Baraffe, I., Chabrier, G., Allard, F., & Hauschildt, P. H. 1998, A&A 337, 403

Baraffe, I., Chabrier, G., Barman, T. S., et al. 2003, "Evolutionary models for cool brown dwarfs and extrasolar giant planets. The case of HD 209458", A&A, 402, 701B

Batalha, N. M. 2014, Proceedings of the National Academy of Science, 111, 12647

Beaulieu, J.-P., Bennett, D. P., Fouqué, P., et al. 2006, Nature, 439, 437

Bonnet-Bidaud, J. M., & Pantin, E. 2008, A&A, 489, 651

Boss, A. P. 1997, "Giant planet formation by gravitational instability", Science, 276, 1836B

Bouchy, F., Pepe, F., & Queloz, D. 2001, A&A, 374, 733

Bowler, B. P., Johnson, J. A., Marcy, G. W., et al. 2010, "Retired A Stars and Their Companions. III. Comparing the Mass-Period Distributions of Planets Around A-Type Stars and Sun-Like Stars", ApJ, 709, 396B

Brandeker, A., Jayawardhana, R., Khavari, P., Haisch, K. E., Jr., & Mardones, D. 2006, ApJ, 652, 1572

Brandt, T. D., McElwain, M. W., Turner, E. L., 2013, "New Techniques for High-contrast Imaging with ADI: The ACORNS-ADI SEEDS Data Reduction Pipeline", ApJ, 764, 183B

Bressan, A., Marigo, P., Girardi, L., et al. 2012, MNRAS, 427, 127

Butler, R. P., Marcy, G. W., Williams, E., McCarthy, C., Dosanjh, P., & Vogt, S. S. 1996, PASP, 108, 500

Cassan, A., Kubas, D., Beaulieu, J.-P., et al. 2012, Nature, 481, 167

Bressan, A., Marigo, P., Girardi, L., 2012, "PARSEC: stellar tracks and isochrones with the PAdova and TRieste Stellar Evolution Code", MNRAS, 427, 127B

Charbonneau, D., Brown, T. M., Latham, D. W., Mayor, M. 2000, "Detection of Planetary Transits Across a Sun-like Star", ApJ, 529L, 45C

Charbonneau, D., Brown, T. M., Noyes, R, W., Gilliland, R. L. 2002, "Detection of an Extrasolar Planet Atmosphere", ApJ, 568, 377C

Chen, Y., Bressan, A., Girardi, L., et al. 2015, MNRAS, 452, 1068

Chabrier, G., Baraffe, I., Allard, F., & Hauschildt, P.: 2000, ApJ, 542, 464

Crepp, J. R., Johnson, J. A., Howard, A. W., et al. 2012, "The TRENDS High-contrast Imaging Survey. I. Three Benchmark M Dwarfs Orbiting Solar-type Stars", ApJ, 761, 39C

Crepp, J. R., Johnson, J. A., Howard, A. W., et al. 2013a, "The TRENDS High-contrast Imaging Survey. II. Direct Detection of the HD 8375 Tertiary", ApJ, 771, 46C

Crepp, J. R., Johnson, J. A., Howard, A. W., et al. 2013b, "The TRENDS High-contrast Imaging Survey. III. A Faint White Dwarf Companion Orbiting HD 114174", ApJ, 774, 1C

Crepp, J. R., Johnson, J. A., Howard, A. W., et al. 2014, "The TRENDS High-contrast Imaging Survey. V. Discovery of an Old and Cold Benchmark T-dwarf Orbiting the Nearby G-star HD 19467", ApJ, 781, 29C

Cumming, A., Butler, R. P., Marcy, G. W., et al. 2008, PASP, 120, 531

Cutri, R. M., Skrutskie, M. F., van Dyk, S., et al. 2003, VizieR Online Data Catalog, 2246, 0

da Silva, R., Milone, A. C., Reddy, B. E. 2011, "omogeneous photospheric parameters and C abundances in G and K nearby stars with and without planets", A&A, 526A, 71D

Dressing, C. D., & Charbonneau, D. 2015, ApJ, 807, 45

Duchéne, G., & Kraus, A. 2013, "Stellar Multiplicity", ARA&A, 51, 269D

Egner, S., Ikeda, Y., Watanabe, M., et al. 2010, "Atmospheric dispersion correction for the Subaru AO system", SPIE, 7736E, 4VE

Forgan, D., Parker, R. J., & Rice, K. 2015, MNRAS, 447, 836

Frink, S., Mitchell, D. S., Quirrenbach, A., et al. 2002, "Discovery of a Substellar Companion to the K2 III Giant ι Draconis", ApJ, 576, 478F

Gaia Collaboration, Brown, A. G. A., Vallenari, A., et al. 2016, A&A, 595, A2

Galicher, R., Marois, C., Macintosh, B., et al. 2016, A&A, 594, A63

Girardi, L., Barbieri, M., Groenewegen, M. A. T., et al. 2012, Astrophysics and Space Science Proceedings, 26, 165

Haisch, K. E., Jr., Lada, E. A., & Lada, C. J. 2001, ApJL, 553, L153

Hatzes, A. P., & Cochran, W. D. 1992, European Southern Observatory Conference and Workshop Proceedings, 40, 275

Hauschildt, P. H., Allard, F., Baron, E. 1999, "The NextGen Model Atmosphere Grid for 3000 <= Teff <= 10,000 K", ApJ, 512, 377H

Hauschildt, P. H., Allard, F., Ferguson, J., Baron, E., & Alexander, D. R.: 1999b, ApJ, 525, 871

Hayano, Y., Takami, H., Guyon, O., et al. 2008, "Current status of the laser guide star adaptive optics system for Subaru Telescope", SPIE, 7015E, 10H

Hayashi, C. 1981, "Structure of the Solar Nebula, Growth and Decay of Magnetic Fields and Effects of Magnetic and Turbulent Viscosities on the Nebula", PThPS, 70, 35H

Hayashi, C., Nakazawa, K., & Nakagawa, Y. 1985, Protostars and Planets II, 1100

Ho, S., & Turner, E. L. 2011, ApJ, 739, 26

Holberg, J. B., Oswalt, T. D., Sion, E. M., Barstow, M. A., & Burleigh, M. R. 2013, MNRAS, 435, 2077

Holman, M., Touma, J., & Tremaine, S. 1997, Nature 386, 254

Howard, A. W., Johnson, J. A., Marcy, G. W., et al. 2010, ApJ, 721, 1467H

Howard, A. W., Marcy, G. W., Johnson, J. A., et al. 2010, Science, 330, 653

Howell, S. B., Everett, M. E., Sherry, W., Horch, E., & Ciardi, D. R. 2011, AJ, 142, 19

Ida, S., & Lin, D. N. C. 2004, "Toward a Deterministic Model of Planetary Formation. I. A Desert in the Mass and Semimajor Axis Distributions of Extrasolar Planets", ApJ, 604, 388I

Ida, S., Lin, D. N. C., & Nagasawa, M. 2013, ApJ, 775, 42

Izumiura, H. 1999, in Proc. 4th East Asian Meeting on Astronomy, ed. P. S. Chen (Kunming: Yunnan Observatory), 77

Janson, M., Bonavita, M., Klahr, H., & Lafrenière, D. 2012, ApJ, 745, 4

Johnson, J. A., Butler, R. P., Marcy, G. W., et al. 2007, "A New Planet around an M Dwarf: Revealing a Correlation between Exoplanets and Stellar Mass", ApJ, 670, 833J

Johnson, J. A., Marcy, G. W., Fischer, D. A., et al. 2008, ApJ, 675, 784-789

Johnson, J. A., Aller, K. M., Howard, A. W., & Crepp, J. R. 2010b, PASP, 122, 905

Kambe, E., Sato, B., Takeda, Y., et al. 2002, PASJ, 54, 865

Kane, S. R., Reffert, S., Henry, G. W., et al. 2010, "On the Transit Potential of the Planet Orbiting Iota Draconis", ApJ, 720, 1644K

Kane, S. R., Howell, S. B., Horch, E. P., 2014, "Limits on Stellar Companions to Exoplanet Host Stars with Eccentric Planets", ApJ, 785, 93K

Kennedy, G. M., & Kenyon, S. J. 2008, ApJ, 673, 502-512

Kipping, D. M. 2013, MNRAS, 435, 2152

Knutson, H. A., Fulton, B. J., Montet, B. T., et al. 2014, ApJ, 785, 126

Kozai, Y. 1962, "Secular perturbations of asteroids with high inclination and eccentricity", AJ, 67, 591K

Kuzuhara, M., Tamura, M., Kudo, T., et al. 2013, ApJ, 774, 11

Lafrenière, D., Marois, C., Doyon, R., 2007, "A New Algorithm for Point-Spread Function Subtraction in High-Contrast Imaging: A Demonstration with Angular Differential Imaging", ApJ, 660, 770L

Laney, C. D., Joner, M. D., & Pietrzyński, G. 2012, MNRAS, 419, 1637

Lejeune, T., & Schaerer, D. 2001, A&A, 366, 538

Lin, D. N. C., Bodenheimer, P., Richardson, D. C. 1997, "Orbital migration of the planetary companion of 51 Pegasi to its present location", Nature, 380, 606L

Liu, M. C., Fischer, D. A., Graham, J. R., et al. 2002, ApJ, 571, 519

Marcy, G. W., & Butler, R. P. 1992 "Precision radial velocities with an iodine absorption cell", PASP, 104, 270M

Marcy, G. W., & Butler, R. P. 1996, ApJL, 464, L147

Fischer, D. A., & Valenti, J. 2005, ApJ, 622, 1102

Marois, C., Lafrenière, D., Doyon, R., et al. 2006, "Angular Differential Imaging: A Powerful High-Contrast Imaging Technique", ApJ, 641, 556M

Marois, C., Macintosh, B., Barman, T. et al. 2008, "Direct Imaging of Multiple Planets Orbiting the Star HR 8799", Science, 322, 1348M

Mayor, M., & Queloz, D. 1995, "A Jupiter-Mass Companion to a Solar-Type Star", Nature, 378, 355

Marzari, F., Weidenschilling, S. J., 2002, "Eccentric Extrasolar Planets: The Jumping Jupiter Model", Icarus, 156, 570M

Mede, K., & Brandt, T. D. 2017, AJ, 153, 135

Mizuno, H. 1980, Progress of Theoretical Physics, 64, 544

Montet, B. T., Crepp, J. R., Johnson, J. A., et al. 2014, "The TRENDS High-contrast Imaging Survey. IV. The Occurrence Rate of Giant Planets around M Dwarfs", ApJ, 781, 28M

Mordasini, C., Alibert, Y., Benz, W., & Naef, D. 2009, A&A, 501, 1161

Mordasini, C., Alibert, Y., Benz, W., et al. 2012, "Extrasolar planet population synthesis . IV. Correlations with disk metallicity, mass, and lifetime", A&A, 541A, 97M

Mugrauer, M., Ginski, C., Seeliger, M. 2014, "New wide stellar companions of exoplanet host stars", MNRAS, 439, 1063M

Müller, S., Helled, R., & Mayer, L. 2018, ApJ, 854, 112

Nagasawa, M., Ida, S., & Bessho, T. 2008, ApJ, 678, 498

Narita, N., Kudo, T., Bergfors, C., et al. 2010, PASJ, 62, 779N

Narita, N., Takahashi, Y. H., Kuzuhara, M., et al. 2012, PASJ, 64L, 7N

Quintana, E. V., Barclay, T., Raymond, S. N., et al. 2014, Science, 344, 277

Raghavan, D., McAlister, H. A., Henry, T. J., et al. 2010, "A Survey of Stellar Families: Multiplicity of Solar-type Stars", ApJS, 190, 1R

Reffert, S., Bergmann, C., Quirrenbach, A., Trifonov, T., & Künstler, A. 2015, A&A, 574, A116

Rodigas, T. J., Arriagada, P., Faherty, J., et al. 2016, ApJ, 818, 106

Sato, B., Kambe, E., Takeda, Y., Izumiura, H., & Ando, H. 2002, PASJ, 54, 873

Sato, B., Ando, H, Kambe, E., et al. 2003, "A Planetary Companion to the G-Type Giant Star HD 104985", ApJ, 597L, 157S

Sato, B., Izumiura, H., Toyota, E., et al. 2008, "Planetary Companions around Three Intermediate-Mass G and K Giants: 18 Delphini, ξ Aquilae, and HD 81688"

Sato, B., Omiya, M., Harakawa, H., et al. 2012, "Substellar Companions to Seven Evolved Intermediate-Mass Stars", PASJ, 64, 135S

Sato, B., Omiya, M., Wittenmyer, R. A., et al. 2013, ApJ, 762, 9

Sato, B., Omiya, M., Harakawa, H., et al. 2013, "Planetary Companions to Three Evolved Intermediate-Mass Stars: HD 2952, HD 120084, and ω Serpentis", PASJ, 65, 85S

Scott, N. et al PASP, in prep

Spiegel, D., Burrows, A. 2012, "Spectral and Photometric Diagnostics of Giant Planet Formation Scenarios", ApJ, 745, 174S

Suzuki, R., Kudo, T., Hashimoto, J., et al. 2010, "Performance characterization of the HiCIAO instrument for the Subaru Telescope", SPIE, 7735E, 30S

Takahashi, Y. H., Narita, N., Hirano, T., et al. 2013 arXiv: 1309.2559T

Takeda, Y., Sato, B., Murata, D. 2008, "Stellar Parameters and Elemental Abundances of Late-G Giants", PASJ, 60, 781T

Tamura, M., Hodapp, K., Takami, H., et al. 2006, "Concept and science of HiCIAO: high contrast instrument for the Subaru next generation adaptive optics", SPIE, 6269E, 0VT

Tamura, M. 2009, "Subaru Strategic Exploration of Exoplanets and Disks with HiCIAO/AO188 (SEEDS)", AIPC, 1158, 11T

Tamuz, O., Ségransan, D., Udry, S., et al. 2008, "The CORALIE survey for southern extra-solar planets. XV. Discovery of two eccentric planets orbiting HD 4113 and HD 156846", A&A, 480L, 33T

Torres, G. 1999, PASP, 111, 169

Toomre, A. 1964, ApJ, 139, 1217

van Leeuwen, F. 2007, A&A, 474, 653

Valenti, J. A., Butler, R. P. & Marcy, G. W. 1995, PASP, 107, 966.

Vigan, A., Bonavita, M., Biller, B., et al. 2017, A&A, 603, A3

Wang, L. Sato, B., Omiya, M., 2014, "A long-period eccentric substellar companion to the evolved intermediate-mass star HD 14067", PASJ, tmp, 119W

Wertz, O., Absil, O., Gómez González, C. A., et al. 2017, A&A., 598, A83

Wu, Y. & Murray, N. 2003, ApJ, 589, 605

Wu, Y., & Lithwick, Y. 2010, ApJ, 735, 109

Zechmeister, M., Reffert, S., Hatzes, A. P., et al. 2008, "The discovery of stellar oscillations in the K giant ι Draconis", A&A, 491, 531Z